# THEORETICAL AND MOLECULAR DYNAMICS SIMULATION STUDIES ON THE MECHANICS OF CARBON NANOMATERIALS–BASED NANO/BIO-SYSTEMS

BY

XINGHUA SHI

B.E., PEKING UNIVERSITY, 2001

M.S., CHINESE ACADEMY OF SCIENCES, 2004

A DISSERTATION SUBMITTED IN PARTIAL FULFILLMENT OF THE REQUIREMENTS FOR THE DEGREE OF DOCTOR OF PHILOSOPHY IN THE SCHOOL OF ENGINEERING AT BROWN UNIVERSITY

PROVIDENCE, RHODE ISLAND

MAY 2011

This dissertation by Xinghua Shi is accepted in its present form

by the School of Engineering as satisfying the

dissertation requirement for the degree of Doctor of Philosophy.

Date_____ _____

Huajian Gao, Advisor

Recommended to the Graduate Council

Date_____ _____

Kyung-Suk Kim, Reader

Date_____ _____

Robert Hurt, Reader

Approved by the Graduate Council

Date_____ _____

Peter Weber, Dean of the Graduate School

# *Vita*

Xinghua Shi was born in Jiangsu province of China on February 9, 1978. He received his B.E. degree from Peking University in 2001, and his M.S. degree from Institute of Mechanics, Chinese Academy of Sciences in 2004. He entered the solid mechanics group at Brown University for pursuing the Ph.D. degree in August 2006.

# *Acknowledgements*

First and foremost, I would like to thank my advisor, Prof. Huajian Gao, for accepting me as his doctoral student and offering me the opportunity to work on some of the most interesting problems in nanomechanics. He has had the greatest professional influence on my development as a scientist. His courage to tackle new and difficult problems and his patience to withstand the many failures that accompany such risks is admirable. All of the work in this thesis has come out of very pleasant collaborations with him. I thank him for the support, guidance and patience throughout my Ph.D. study, which helped to make this learning experience the one I will always remember.

I am grateful to the members of the thesis committee, Prof. Kim and Prof. Hurt, for their insightful comments and valuable suggestions making significant improvements to my thesis. I would like to thank Prof. Nicola Pugno from Politecnico di Torino of Italy for stimulating discussions and collaboration during the course of my PhD study. I have benefited a lot from useful conversations and enjoyable collaborations with many post-docs and students during my stay at Brown. Also, I would like to thank the faculty of Brown Solid Mechanics for providing many high-quality courses that contributed to my education.

I want to express my deepest appreciation to my family, particularly to my wife Liang. This thesis could not have been completed without their constant encouragement and support.

# *Contents*

# *List of Tables*

# *List of Figures*

# *Chapter 1*

# *Introduction*

## 1.1 Overview of carbon nanotubes-cell interaction

The question of whether and how nanomaterials enter human and animal cells is of importance for the development of efficient gene and drug delivery systems as well as for assessing the potential hazards of nanotechnology on ecology and human health. Due to their unique physical, chemical, electrical and optical properties, carbon nanotubes (CNT) and other nanomaterials have shown enormous potential and promise to be adapted and integrated into biomedical devices, such as site-specific drug delivery systems [1-3], non-viral gene carriers [4] as well as biosensor and screening systems [5-7]. Along with these promising applications, there is also increasing concern about the effects of nanomaterials on human health. For example, in assessing the responses of animal/human cells to CNTs, it was found that some cells tend to wrap CNTs into nodular structures and isolate CNT-attached parts from the main cell population [8]. It has also been convincingly shown that CNTs can cross the cell membrane into cytoplasm, even entering the cell nucleus [9-16]. On the other hand, the mechanisms and pathways CNTs entering cells are not fully resolved. So far, two different uptake

pathways have been suggested based on experimental observations: one is endocytosis [9-13] and the other is direct insertion and diffusion through the lipid bilayer of cell membrane [14-16]. The discrepancy from the experimental observations is calling for further theoretical modeling and simulations on this subject.

The entry angle of CNT into the cell is another important issue. Recently it has been found that MWCNTs tend to enter the AML12 liver cell through a tip entry pathway in which one end of CNTs is engulfed while the other end remained outside the cell [17]. It is proposed that the tip entry induced incomplete uptake of MWCNTs could provoke frustrated endocytosis and even cell death. Why do the CNTs prefer tip entry? Can we explain this phenomenon? This issue will be studied in this thesis through theoretical model and coarse grained molecular dynamics (CGMD) simulations.

It has been shown experimentally that the size [18-20] and shape [20, 21] of nanoparticle play important roles in endocytosis. Theoretical studies have shown that particles with size at the nanometer scale can enter the cell most efficiently [22]. Another important issue is the role of stiffness of nanoparticles in cellular uptake. It has been found that the HIV virus regulates its mechanical properties at different stages of the life cycle: It becomes stiff during viral budding while remaining relatively soft before and afterward [23]. Why does the virus regulate its stiffness at different stages of its lifetime? Does the stiffness of a nanoparticle influence its interaction with the cell? Can we model the wrapping process taking the stiffness of the particle into account? To answer these questions, we will set up a simple molecular dynamics model in which the membrane wrapping around a cylindrical nanoparticle is modeled by a graphene sheet wrapping around a carbon nanotube. Of special interest is how the stiffness of CNT influences the

final state of wrapping. This work may provide some guidelines for the development of efficient gene and drug targeting and delivery systems in biomedical technology.

### 1.2 Overview of carbon nanoscrolls

Carbon nanoscralls (CNSs), also referred to as buckyrolls, have attracted significant interests in recent years [24-29]. Unlike the tubular structure of carbon nanotubes (CNT), a CNS is made of a continuous basal graphene sheet rolled up in a spiral form. Due to this topology, CNSs have shown unique structural [30-34], dynamical [31] and electronic [25, 30, 35, 36] properties. It has been found that a stable formation of CNS exists with energy lower than that of precursor graphene [31]. The core of CNS can be significantly changed upon charge injection, which makes it a natural choice for a new class of efficient nanoacutator [36]. The flexible core and large surface area also enable the CNS to be utilized for possible hydrogen storage [32-34]. Recent experiments on electrical-transport measurements [25] show that the resistance of CNS is weakly gate-dependent but strongly temperature-dependent. In addition, the CNS can sustain a high current density, indicating it a good candidate for microcircuit interconnects. All these properties of CNS indicate that CNSs may have numerous applications in nanotechnology.

Despite these experimental and molecular dynamics simulation studies on the CNS, there is still no theoretical investigation on its structural and dynamical properties. Is the CNS stable? Canits core size and dynamical motion be controlled? Part of this thesis is dedicated to setting up a theoretical framework to answer these questions.

So far most previous studies on carbon nanomaterials-based systems have been focused on CNT-based nano- or nano-bio-systems, such as molecular probes or sensors

[37], gene or drug delivery systems [38], nanoelectromechanical systems (NEMS) [39, 40]. Specifically, CNT-water [41-49], CNT-CNT [50], CNT-DNA oligonucleotides [51, 52] and CNT-peptide [53] systems have been studied for encapsulating different types of molecules inside the CNTs. One disadvantage of the CNT-based systems is that the core size of CNTs is uncontrollable due to their closed structure. For applications such as tunable water and ion channels, molecular sensors, as well as flexible gene and drug delivery systems, it will be desirable to develop nanostructures with tunable core sizes. In this thesis we demonstrate that the CNS might be an ideal candidate for such applications.

### 1.3 Organization of this thesis

The remainder of this thesis is organized as follows. In Chapter 2, we first investigate the size effect (radius) of CNTs entering the cell using CGMD. Two different theoretical models will be established to describe the wrapping and piercing of CNTs into the membrane, respectively. Then the tip entry of CNTs is studied through CGMD. The results are compared to predictions from theoretical models. At the end of this Chapter, the role of stiffness of nanoparticles in entering the cell is investigated. In Chapter 3, we derive an analytical equation describing the core size of CNS, followed by MD simulations to verify the theoretical model. The theoretical model for electric field induced dipole-dipole interaction is derived in Chapter 4. Then we demonstrate that the surface energy of CNS is reduced upon an applied electric field. In Chapter 5, a theoretical model is derived to describe the fundamental frequency of breathing oscillatory behavior of CNSs. MD simulations are conducted to verify the model as well

as to study the energy dissipation of oscillation. The problem of maximized core size of CNS under stimuli with resonant frequency is also studied in this Chapter. In Chapter 6, we derive a theoretical model describing the rolling/unrolling behavior of CNSs on substrate. MD simulations are performed to verify the model. The energy release rates of two modes of CNSs motion on substrate are compared. In Chapter 7, we conduct MD simulation to investigate CNS-based water channel with special attention on the enhanced flow rate and water diffusivity under DC and AC electric field. In Chapter 8 we study the electromechanical properties of CNS crystal through MD simulations. We investigate the giant electrostriction and hyperelastic behavior of CNS crystal. The response of CNSs under axial loading is also investigated. The most important results of this thesis are briefly summarized and an outlook at possible future research is provided in the Chapter 9.

# *Chapter 2*

# *Cellular uptake of carbon nanotubes*

## 2.1 Size effect of carbon nanotubes-cell interaction

In this Section, we conduct coarse grained molecular dynamics (CGMD) and theoretical studies to investigate how carbon nanotubes of different sizes interact and enter a patch of lipid bilayer [54]. By reducing the number of degrees of freedom together with the use of short range potentials, CGMD models can gain four to five orders of magnitude in speed compared with full-atom models, achieving length scales on the order of micrometers and time scales on the order of milliseconds. Encouraged by such computational efficiency, a number of CGMD models have been developed and used to study lipids and surfactants systems, including micelles [55, 56], bilayers [57, 58], micelle aggregation [59] and vesicle formation [60]. However, it should be noted that the computational efficiency of CGMD models is usually gained at the cost of loss in accuracy. An optimal balance between efficiency and accuracy is a key aspect to the development and implementation of CGMD models. Recently, Marrink et al [61] have developed a new CGMD model for lipid and surfactant systems, and it has been shown that this model gives quite accurate

results for structural, elastic, dynamic as well as thermodynamic properties for a number of lipid systems. We will therefore adopt this model in our study.

### 2.1.1 Coarse grained molecular dynamics models

In the CGMD model [61] adopted for the present study, non-bonded interactions between two particles are described by the Lennard-Jones (LJ) potential. The equilibrium distance between two particles is selected as 0.47 nm in all pair groups. The strength of the interaction, however, is set at five different levels, namely I ($\varepsilon$ =5.0 kJ mol$^{-1}$), II ($\varepsilon$ =4.2 kJ mol$^{-1}$), III ($\varepsilon$ =3.4 kJ mol$^{-1}$), IV ($\varepsilon$ =2.6 kJ mol$^{-1}$) and V ($\varepsilon$ =1.8 kJ mol$^{-1}$). A cutoff distance of 1.2 nm is selected for the LJ potential to smoothly shift to zero between the distance of 0.9 nm and 1.2 nm. Normal Coulombic potential is used for the electrostatic interaction. The bonded interaction is described by a harmonic potential with an equilibrium distance of 0.47 nm and a force constant of 1250 kJ mol$^{-1}$ nm$^{-2}$. In our simulations, we select a bilayer of Dipalmitoylphosphatidylcholine (DPPC) lipids, each lipid molecule consisting of 12 particles, two of which have attractive interaction (level I) with water molecules (hydrophilic head group), eight have repulsive interaction (level V) with water molecules (hydrophobic tail) and the other two have intermediate interaction (level III). Multi-walled nanotubes with radii from 1 nm to 5 nm and single-walled nanotubes with radii from 0.5 nm to 0.75 nm are constructed with the same length 6 nm. The multi-walled tubes are formed by assembling single-walled tubes with different radii and an inter-layer spacing of 0.68 nm (Fig. 2.1). The single-walled tube is constructed by folding a plane of rhombic cells, each cell consisting of four particles with nearest neighbour distance 0.42 nm and internal angle 60 °. In the multi-walled tubes, all nearest

and second nearest particles are connected through harmonic potential with a force constant equal to 300 kJ $mol^{-1}$ $nm^{-2}$, so that as a whole the tubes become almost rigid. Such multi-walled tubes can mimic hollow single wall tubes with closed ends and prevent unintended insertion of lipid molecules into the tubes. Since CNTs are commonly functionalized by binding with some proteins or other molecules to enhance their affinity with the cell, the interaction between tube particles and the head group of lipid molecules is set at level I. The interactions of tube particles with water and tails of lipid molecules are set at level III. All the parameters in the CGMD simulations are taken according to the above arrangement unless mentioned otherwise.

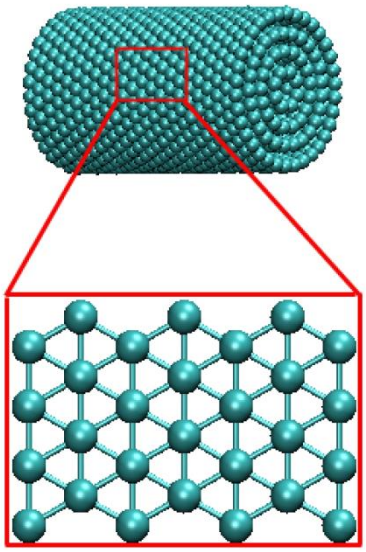

Figure 2.1: Schematic illustration of a coarse grained model of multi-walled carbon nanotubes formed from several single-walled nanotubes with an inter-layer spacing of 0.68 nm. The single-walled nanotube is constructed by rolling up a plane composed of rhombic cells, each cell consisting of four particles with nearest neighbour distance 0.42 nm and internal angle 60 °. [54]

An equilibrated bilayer containing 128 DPPC lipids from Reference [61] is copied 7 times in two lateral directions to generate a patch of membrane consisting of 6272 lipids with an in-plane lateral dimension of 42 × 42 $nm^2$. Initially, the nanotubes are

arranged in close proximity above the center of the bilayer (at a distance of 1 nm to the bilayer surface) with tube axis perpendicular to the plane of the bilayer. We assume the nanotubes would enter the lipid bilayer with their axis perpendicular to the layer--An assumption which will be further examined in some details in Section 2.2. In the present simulations, this is realized by constraining the lateral degrees of freedom. The bilayer and a selected nanotube are placed in a water box of volume $47 \times 47 \times 35$ nm$^3$ which contains 586,000 water particles (2,344,000 water molecules). Periodic boundary condition is applied in three orthogonal directions. All simulations reported in this paper are carried out in the NPT ensemble at temperature 323 K and pressure 1 atm. Through Berendsen's method [62], the temperature and pressure are scaled with time constants of 5 ps and 10 ps, respectively. In all systems, the time step is taken as 20 fs to keep the simulations stable. All simulations are performed with the molecular dynamics package GROMACS [63].

### 2.1.2 Wrapping of nanotubes into membrane

To explore the interaction of multi-walled carbon nanotubes with membrane, we perform a series of CGMD simulations of nanotubes interacting with the lipid bilayer patch described above. Figure 2.2a-f shows the time sequence of 6 snapshots of a selected nanotube with radius 2.3 nm being wrapped into the bilayer. For clarity, the water molecules are not shown here. The nanotube, initially arranged at a distance of 1 nm above the relaxed planar bilayer (Fig. 2.2a), is seen to approach and adhere to the bilayer, causing a small undulatory fluctuation as the lipid molecules spread onto the bottom surface of the nanotube (Fig. 2.2b). With more and more lipid molecules in the upper

monolayer of the bilayer adhering to the tube, the bilayer invaginates and wraps around the tube (Fig. 2.2c-e).

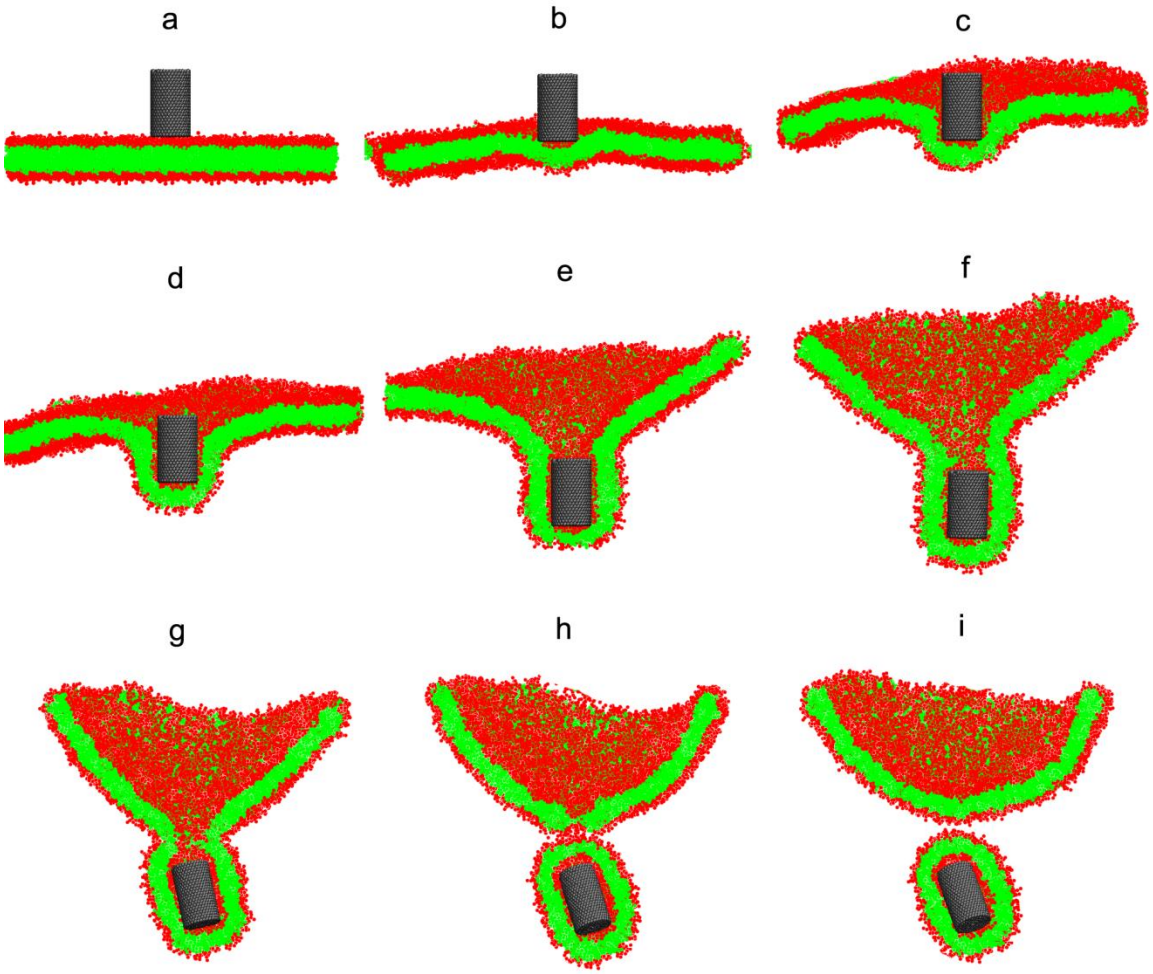


Figure 2.2: (a-f). Time sequence of six snapshots of a multi-walled nanotube entering a membrane via a wrapping process driven by the van der Waals force. The red particles indicate the head group of lipid molecules. (g, h). Fusion of the membrane neck. (i). Separation of the lipid covered tube from the membrane. [54]

At the later stage of this wrapping process, the membrane near the top end of the tube forms a neck (Fig. 2.2f). To complete the wrapping process so that the tube can cross over to the other side of the membrane, the bilayer around the neck must fuse so that the lipid covered tube can detach from the membrane. This wrapping-fusion process

is quite similar to budding/wrapping of viruses for which dynamin and other transmembrane proteins in the necked region are known to facilitate the detachment or fission process by reducing the binding affinity of membrane [64, 65]. In the CGMD simulations, we mimic this process by reducing the interactions between lipid molecules at the neck region. Figure 2.2g-h shows the fusion of bilayer and Figure 2.2i shows the final state of the fission process, where the outer monolayer fuses and the lipid covered tube is completely separated from the membrane.

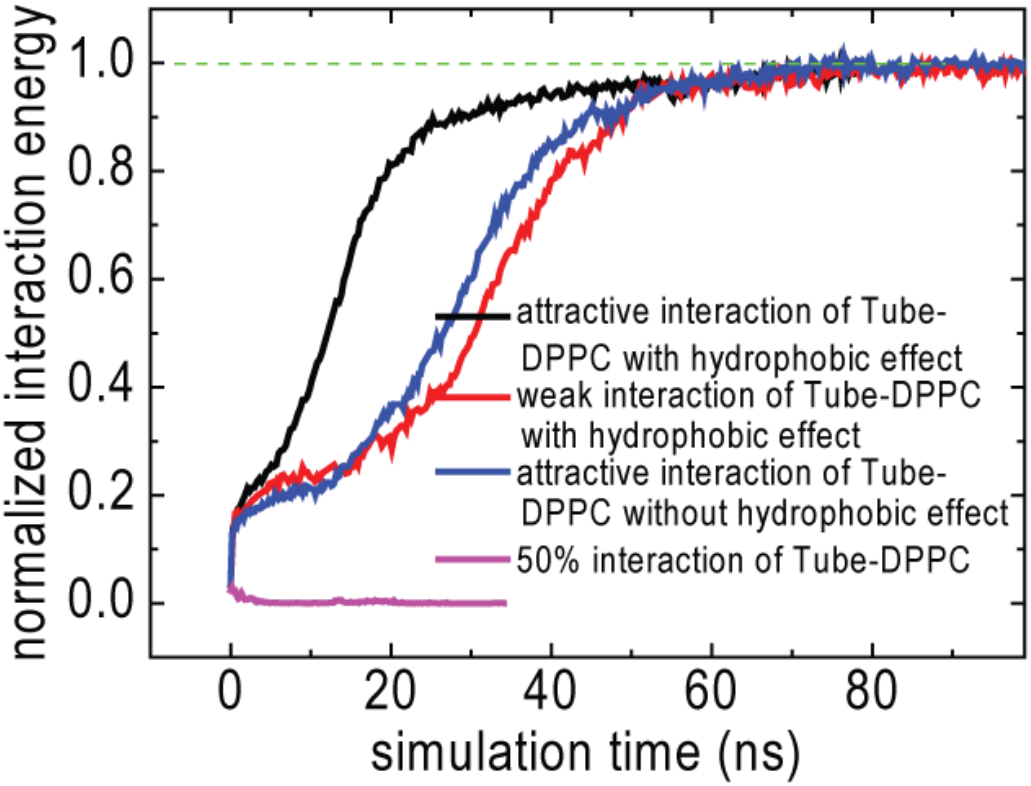


Figure 2.3: Interaction energy (normalized by the maximum interaction energy with corresponding interaction parameters) between the nanotube and membrane as a function of simulation time. The black line shows the case of strong interaction between the nanotube and DPPC in the presence of hydrophobic effect. The red line shows the case of weak interaction between the nanotube and DPPC in the presence of hydrophobic effect on. The blue line shows the case of strong interaction between the nanotube and DPPC in the absence of hydrophobic effect. The magenta line corresponds to the case when the interaction between the nanotube and DPPC is reduced by 50%. [54]

Figure 2.3 shows the variation of interaction energy between the tube and lipid molecules as a function of time. The steep slope of the energy profile in Figure 2.3 indicates rapid wrapping at the initial stage. As the wrapping proceeds, the flattening of slope shows a gradual decrease of the wrapping speed. At the later stage, the increasing curvature deformation near the top end of the tube significantly slows down the wrapping process.

What is the driving force for wrapping the tube into the bilayer? As the particle forming the tube carries no electric charge, the tube interacts with lipid and water molecules primarily via van der Waals forces. To check the importance of van der Waals force in the wrapping process, we reduce the interaction strength between lipid and tube particles and repeat the simulation. The magenta line in Figure 2.3 shows that, with 50% reduction in van der Waals interaction strength, the tube will adhere to the membrane but no wrapping occurs. Because the simulations are performed in a water box and carbon nanotubes are hydrophobic materials, hydrophobic interactions could play an important in this process. To clarify this issue, we change the interaction between water and tube molecules from level III to level IV and repeat the simulation. The blue line in Figure 2.3 shows that the tube is rapidly wrapped into the membrane with significant reduction in wrapping time, indicating that the hydrophobic effect has a significant effect on the wrapping process. We have also considered the case when the interaction between lipid and tube molecules is changed to level II. The red line in Figure 2.3 shows that the wrapping speed is initially slower but eventually catches up with the blue line. These studies indicate that both van der Waals attraction (between the tube and bilayer) and

hydrophobic interaction (between the tube and water) play important roles in the wrapping process.

To investigate the effect of tube radius on the wrapping process, we consider a smaller nanotube with radius 1.2 nm and repeat the simulation. Figure 2.4 shows the wrapping depth as a function of simulation time. The wrapping rate is about 0.7 nm/ns for the 2.3 nm tube and about 0.45 nm/ns for the 1.2 nm tube. This size effect can be understood from the fact that the thinner tube causes larger curvature energy of the membrane which tends to resist the wrapping process.

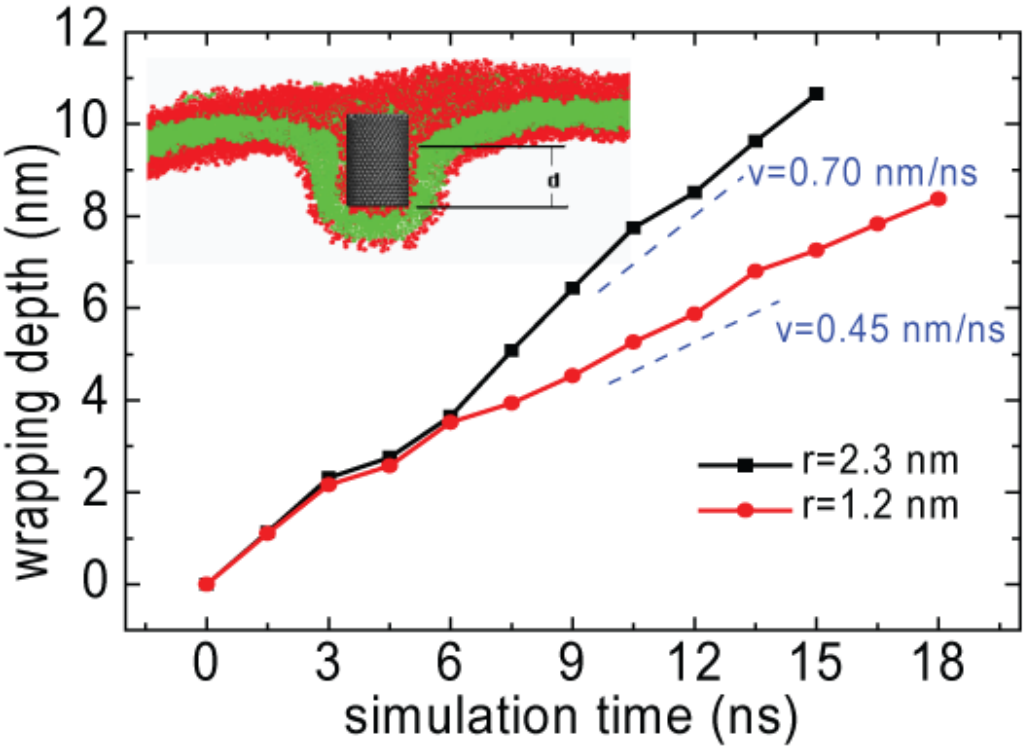


Figure 2.4: The depth of wrapping as a function of simulation time. The wrapping velocity is about 0.7 nm/ns for a nanotube with radius 2.3 nm (black line) and about 0.45 nm/ns (red line) for a smaller tube with radius 1.2 nm. [54]

### 2.1.3 Piercing of nanotube through membrane

As the radius of the nanotube is further decreased, we observe an interesting change of entry mechanism. For the wrapping process to be successful, the driving force due to van der Waals and hydrophobic interactions must exceed the resistance force due to the curvature energy of the membrane. For sufficiently small tubes, the driving force would become comparable to or smaller than the resistance force. To illustrate this, we repeat the simulation for a single-walled nanotube of 0.5 nm in radius while keeping all the other conditions identical to the previous simulations. Figure 2.5a-c show that, instead of crossing the membrane via wrapping, the tube simply pierces through the membrane. Our results also confirm the work by Lopez et al [66] that a small radius tube (~0.65 nm) with hydrophilic caps would insert into membrane and serve as a synthetic channel. Apparently, with decreasing radius, a nanotube would change its pathway of entry from wrapping to piercing. When the tube becomes a transmembrane tube as shown in Figure 2.5d, there is no more driving force for the tube to move further. On the other hand, living cells exist in a complicated chemical environment influenced greatly by the ion concentrations in solution. The osmotic gradients across the cell membrane are known to drive much of transmembrane transport. We modify the interaction between tube and water molecules on the lower side of the membrane to level II, thus artificially adding a potential gradient across the membrane. This potential is seen to drive the tube through the bilayer (Figs. 2.5e, f). Figure 2.6 shows the variation of the interaction energy between the tube and water molecules above and below the bilayer.

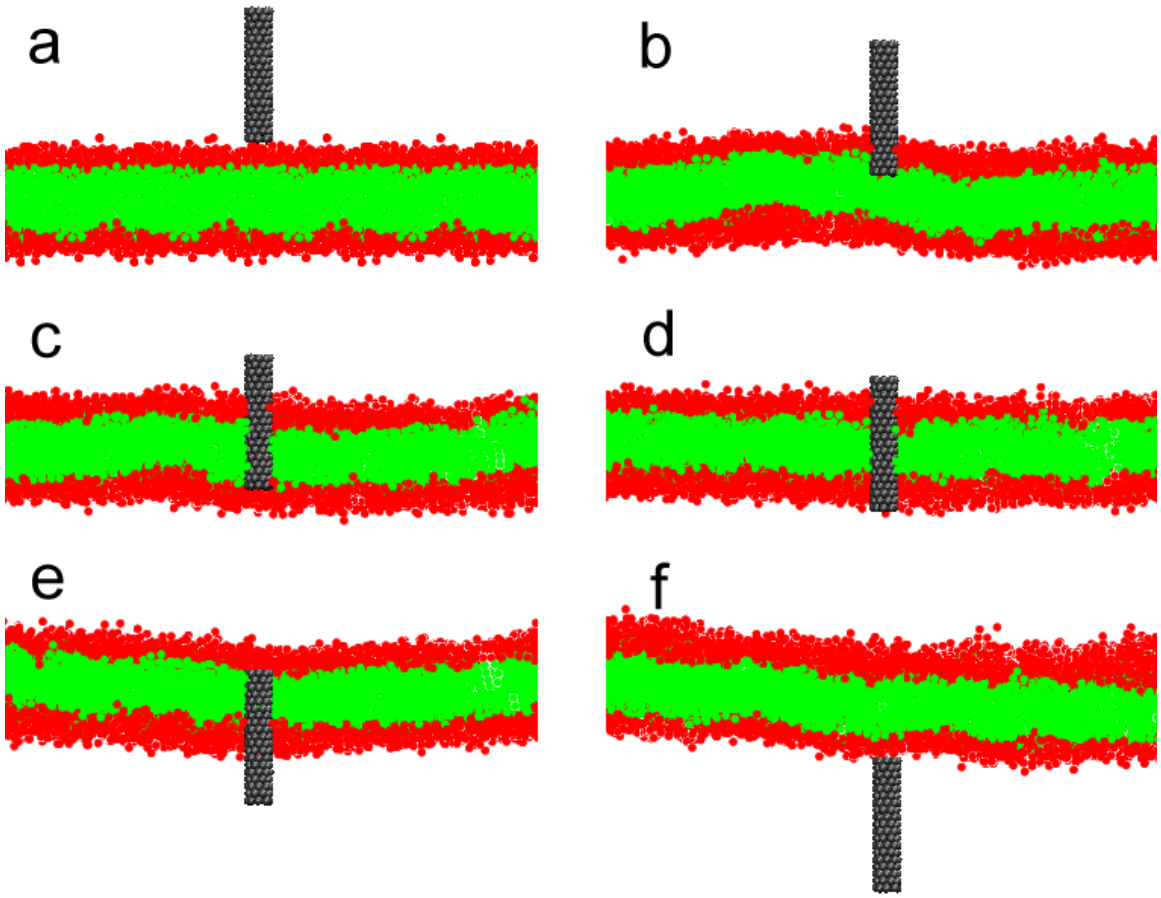


Figure 2.5: Time sequence of six snapshots of a (single-walled) nanotube piercing through a membrane driven by the van der Waal force. [54]

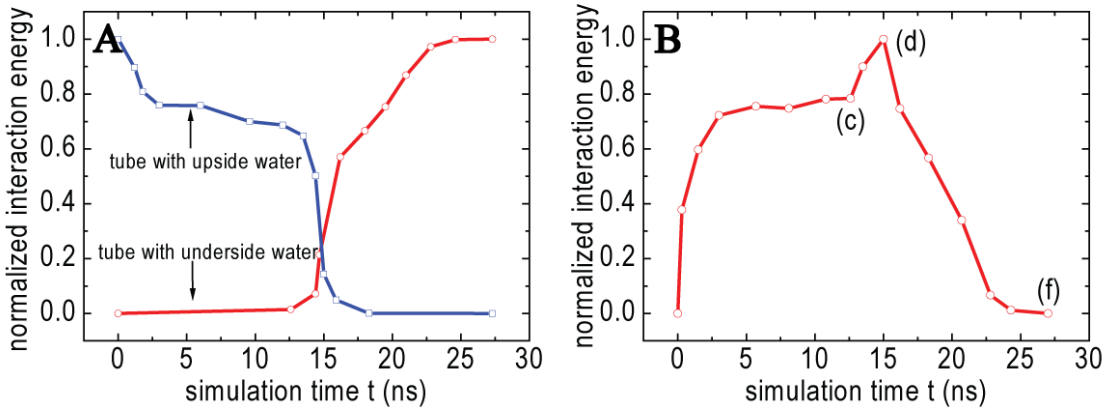


Figure 2.6: (**A**) Interaction energy (normalized by the maximum interaction energy with corresponding interaction parameters) between the (single-walled) nanotube and water as a function of time during piercing. The blue line corresponds to interaction between the nanotube and water above the bilayer, while the red line corresponds to interaction between the nanotube

and water below the bilayer. (**B**) Normalized interaction energy of the nanotube with lipid molecules as a function of time. The letter c, d, and f indicate the states shown in Figure 2.5. [54]

### 2.1.4 Theoretical models of wrapping and piercing mechanisms

To aid the understanding of the observed change in pathway of nanotubes entering cell, we propose two theoretical models to describe the wrapping and piercing mechanisms. It is well known that the lipid bilayer behaves like a two dimensional fluid in the plane of the membrane and a bending-resistant solid in the third dimension. In the wrapping process, the bilayer undergoes large deformation with rearrangement of lipid molecules to form a cylindrical shape. In the piercing process, the lipid molecules beneath the bottom end of the tube are squeezed outwards by the piercing tube. We propose two different theoretical models to describe these two entry mechanisms.

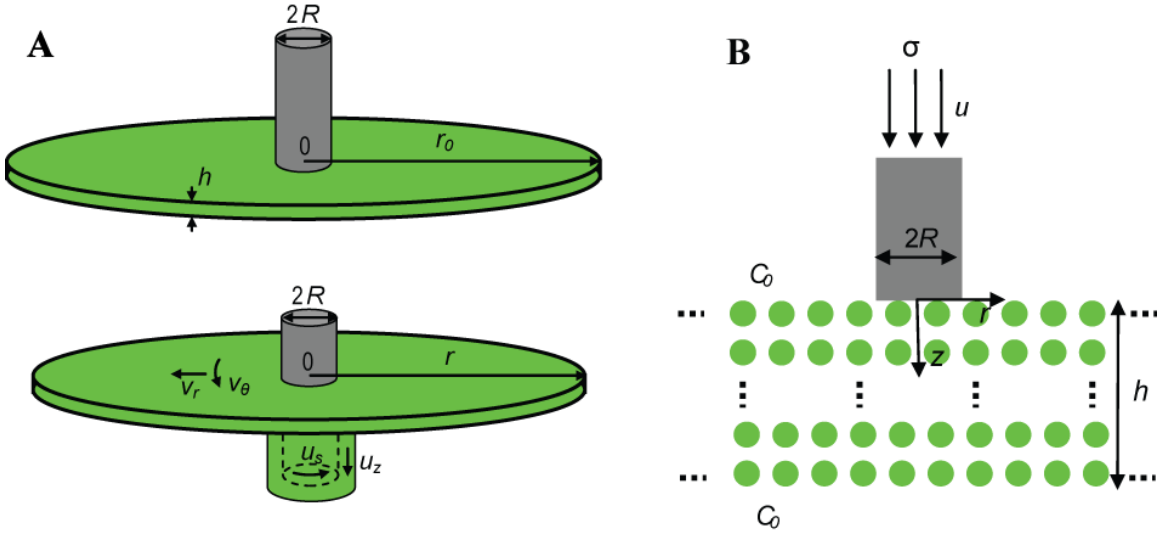


Figure 2.7: The theoretical models for wrapping and piercing of nanotubes into cell. (**A**) Schematic illustration of cell membrane wrapping around the tube. The membrane is considered as a two dimensional viscous fluid with fixed thickness $h$ in the third dimension. (**B**) Schematic illustration of a vacancy diffusion model for a cylindrical tube indenting a bilayer under stress $\sigma$. [54]

For the wrapping mechanism, we model the lipid bilayer as a two dimensional incompressible viscous fluid with fixed thickness *h* in the third dimension. Consider an infinite flat bilayer wrapping around a nanotube with radius $R$. In cylindrical coordinates (Fig. 2.7), the components of the rate of deformation tensor are expressed as

$$\begin{aligned} V_r &= \frac{\partial v_r}{\partial r}, \\ V_\theta &= \frac{1}{r}\frac{\partial v_\theta}{\partial \theta} + \frac{v_r}{r} = \frac{v_r}{r}, \end{aligned} \tag{2.1}$$

where $v_r$ and $v_\theta$ are the radial and circumferential velocities of the planar membrane, respectively (Fig. 2.7A). Because of the axisymmetry, $v_\theta$ should not change along the circumferential direction. On the other hand, in-plane incompressibility requires

$$V_r + V_\theta = \frac{\partial v_r}{\partial r} + \frac{v_r}{r} = 0, \tag{2.2}$$

and Eq. (2.1) is simplified as

$$\begin{aligned} V_r &= -\frac{v_r}{r}, \\ V_\theta &= \frac{v_r}{r}. \end{aligned} \tag{2.3}$$

with the radial velocity expressed by

$$r v_r = C_1, \tag{2.4}$$

where $C_1$ is a constant. For the part of membrane which is wrapped around the nanotube, the velocity components are denoted as $u_z$ and $u_s$ (Fig. 2.7A) which satisfy the continuity condition

$$\partial u_z / \partial z + \partial u_s / \partial s = 0. \tag{2.5}$$

Due to the axisymmetry, both $u_s$ and $u_z$ should not change along the circumference of the tube. Thus this part of the membrane has no shear deformation and simply flows at a constant rate, making no contribution to the viscous dissipation. If there is no slipping between the nanotube and the membrane in the wrapping process, the entry velocity of the nanotube is then given by $u_z$. Given the condition that there is no surface area change during the deformation of membrane, we obtain

$$\pi r_0^2 = \pi r_e^2 + 2\pi(R + h/2)L, \tag{2.6}$$

where $r_0$ and $r_e$ are the initial and deformed dimensions of membrane and $L$ is the wrapping depth of the nanotube. The time rate of change of Eq. (2.6) gives

$$r_e \dot{r}_e = r_e v_{re} = -(R + h/2)\dot{L} = -(R + h/2)u_z. \tag{2.7}$$

It follows directly from Eqs. (2.4) and (2.7) that

$$r v_r = -(R + h/2)u_z. \tag{2.8}$$

The rate of viscous dissipation per unit volume during the deformation of membrane is given by [67]

$$\phi = 4\eta(v_r / r)^2 = 4\eta\left(\frac{(R + h/2)u_z}{r^2}\right)^2, \tag{2.9}$$

where $\eta$ is the viscosity of the bilayer. Integrating Eq. (2.9) on the entire plane of the bilayer, we obtain the rate of viscous dissipation associated with the viscous deformation of the membrane as

$$\Phi = \int_V \phi dV = \int_{R+h/2}^{r_e} 4\eta\left(\frac{(R + h/2)u_z}{r^2}\right)^2 h \cdot 2\pi r' dr'. \tag{2.10}$$

On the other hand, the free energy change during the wrapping process is given by

$$F = \left( \frac{1}{2} k_c c^2 - \Delta\gamma \right) \cdot 2\pi (R + h/2) L \,, \tag{2.11}$$

where $k_c$ is the bending modulus, $c = 1/(R + h/2)$ is the curvature of wrapped bilayer and $\Delta\gamma$ is the work of adhesion between the nanotube and the bilayer. Power balance during the wrapping of the tube requires

$$\Phi = -dF/dt \,. \tag{2.12}$$

Combining Eqs. (2.6), (2.10), (2.11) and (2.12) yields

$$u_z = \frac{\Delta\gamma (R + h/2)}{2\eta h} \left( 1 - \frac{1}{2} \frac{k_c}{\Delta\gamma (R + h/2)^2} \right) \left( \frac{r_0^2 - 2(R + h/2)L}{r_0^2 - 2(R + h/2)L - (R + h/2)^2} \right). \tag{2.13}$$

Since the overall size of the membrane is much larger than the tube, for simplicity we assume $r_0 \to \infty$ and simplify Eq. (2.13) as

$$u_z \approx \frac{\Delta\gamma (R + h/2)}{2\eta h} \left( 1 - \frac{1}{2} \frac{k_c}{\Delta\gamma (R + h/2)^2} \right). \tag{2.14}$$

To check the reliability of this model in describing the wrapping process, a series of MD simulations with nanotubes of different radii are performed and the wrapping rates are shown in Figure 2.8, together with Eq. (2.14) where the parameters are chosen as $h = 4$ nm, $\Delta\gamma / 2\eta = 0.52$ nm/ns and $k_c / 2\Delta\gamma = 0.35$ nm$^2$. We emphasize that these are reasonable values since the bending modulus is about $4 \times 10^{-20}$ J [61, 68], the viscosity of membrane at 323 K is about $15 \times 10^{-3}$ Pa·s [69] and the work of adhesion in our simulations is about 0.047 N/m.

For the piercing mode of entry, we adopt a vacancy diffusion model which has been previously developed to describe impression induced creep of a thin film [70].

Figure 2.7B shows a cylindrical punch being pushed into the bilayer with velocity $u$ under stress $\sigma$. The two free surfaces of the membrane are assumed to be a constant source of vacancies with concentration $C_0$. Considering steady state vacancy diffusion, we write Fick's second law

$$D_r \frac{1}{r}\frac{\partial}{\partial r}\left(r\frac{\partial C}{\partial r}\right)+D_z\frac{\partial^2 C}{\partial Z^2}=0 \qquad 0<Z<h, \tag{2.15}$$

with associated boundary conditions

$$C=C_0 \qquad Z=0, \quad r>R, \tag{2.16a}$$

$$C=C_0 \qquad Z=h, \tag{2.16b}$$

$$\frac{\partial C}{\partial Z}=\frac{u}{\Omega D_z} \qquad Z=0, \ 0<r<R, \tag{2.16c}$$

where $D_r$ and $D_z$ are vacancy diffusion coefficients in the radial $(r)$ and vertical $(z)$ directions, and $\Omega$ is the molar volume of the diffusion species. During the piercing, the mechanical work due to punch stress is transformed into the chemical energy as

$$\frac{N_A k_B T}{\pi R^2}\int_S \ln\left(\frac{C_0}{C(r,0)}\right)ds=\sigma\Omega, \tag{2.17}$$

where $N_A$ is Avogadro's number, $k_B$ is Boltzmann's constant, $T$ is the temperature and $S$ the area of the cross section area of the punch. Solving the above equations gives

$$u=u^* f(\chi)\chi, \tag{2.18}$$

where $u^*=\dfrac{3\pi\Omega^2 C_0\sigma D_z}{4N_A k_B T h}$, $\chi=\alpha h/R$, $\alpha=\sqrt{D_r/D_z}$ and

$$\frac{1}{f(\chi)}=1-\frac{\xi(3)}{3\pi}\chi^{-3}+\frac{2\xi(5)}{5\pi}\chi^{-5}+\frac{1}{9}\left(\frac{\xi(3)}{\pi}\right)^2\chi^{-6}+O(\chi^{-7}), \tag{2.19}$$

$\xi(n)$ being the Riemann zeta function. Eq. (2.19) is an asymptotic series which converges with the condition $\chi > 1$. The mobility of lipid molecules in the bilayer is usually much larger in the lateral direction (inter-membrane diffusion) than in the vertical direction (flip-flop), suggesting $\alpha >> 1$. For nanotubes with radius comparable to the thickness of the bilayer, $\chi$ is much larger than 1 and as discussed in [70], Eq. (2.19) would converge to 1 and the rate of piercing becomes inversely proportional to the radius of the tube. To check the validity of this model, CGMD simulations are performed with tubes of different radii piercing into the membrane (the degrees of freedom of some lipid molecules in the direction perpendicular to the plane of the bilayer is constrained to prevent them from wrapping around the tube). Figure 2.8 shows that the theoretical model fits the CGMD results if the parameters in Eq. (2.18) are chosen such that $u^* \alpha h = 0.75\,\mathrm{nm}^2/\mathrm{ns}$, i.e. $u = 0.75/R$.

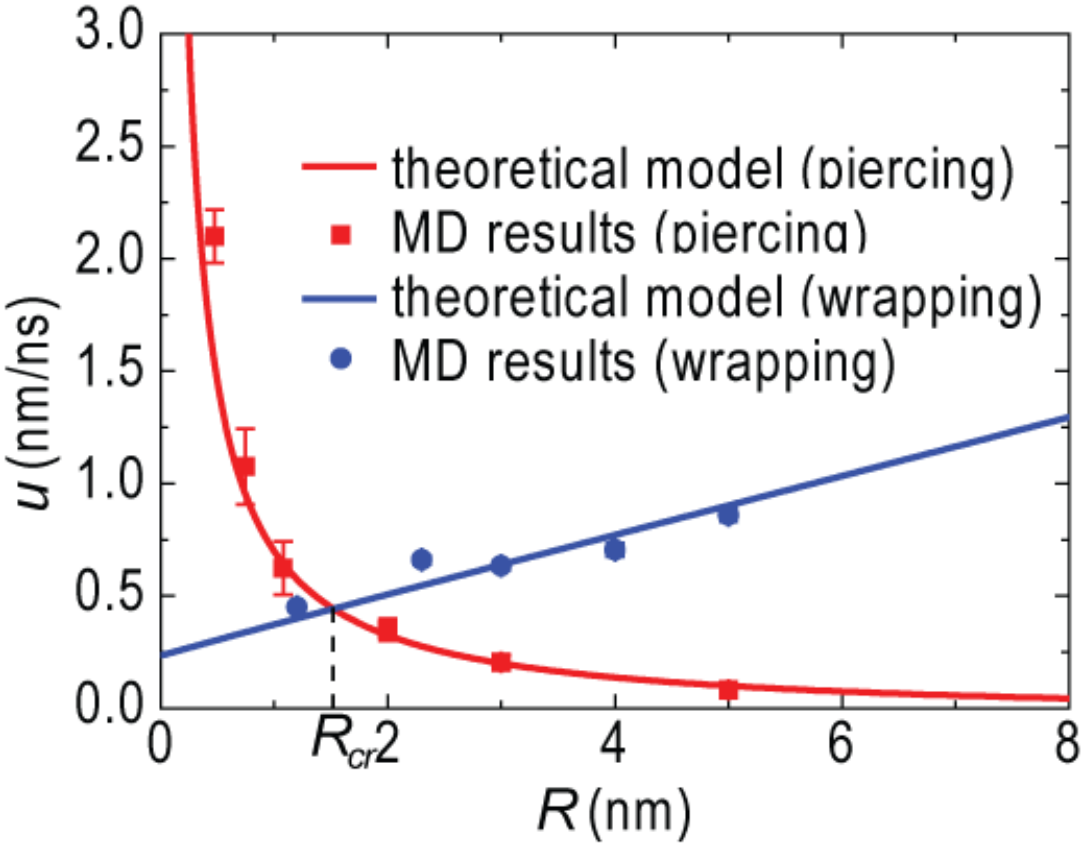


Figure 2.8: The rates of entry associated with wrapping and piercing of nanotubes as a function of the tubes radius. The blue line denotes the theoretical model for the wrapping case and the red one denotes that for the piercing case. The blue dots denote the CGMD simulation results for the wrapping mode of entry and the red dots denote simulation results for the piercing mode of entry. The intersection of the two lines gives rise to a critical size for transition. [54]

Figure 2.8 shows that the observed change of pathway from wrapping to piercing as the radius of the nanotube is reduced to below a critical size may be understood from a kinetic competition between the two modes of entry. For piercing, the rate of entry is governed by the diffusivity of lipid molecules beneath the nanotube to be pushed outward by the tube. In contrast, for wrapping, the rate of entry is controlled by the viscous flow of lipid molecules near the nanotube to wrap around the tube. Below the critical radius $R_{cr}$, the piercing mode is faster due to small distance of diffusion underneath the tube

while the wrapping mode becomes less favorable due to the high curvature associated with wrapping. Above the critical radius, the wrapping mode becomes dominant compared to piercing as the curvature energy is reduced and the diffusion distance is extended. In this way, the radius of the nanotube plays an important role in selecting the pathway of entry into a cell.

## 2.2 Tip entry of carbon nanotubes into the cell

It has been found experimentally that MWCNTs tend to enter the cell through a tip entry mechanism in which one tube end is engulfed by the lipid membrane while the other end remains outside the cell [17]. The tip entry mechanism is of particular interest since similar entry mechanisms of fibrous materials with large aspect ratios (e.g. asbestos) are known to induce frustrated endocytosis/phagocytosis [71-73].To clarify the tip entry mechanism of nanotubes, we conduct CGMD simulations as well as theoretical modeling of a MWCNT entering the cell via receptor-mediated endocytosis.

### 2.2.1 CGMD simulation details

Coarse grained molecular dynamics (CGMD) simulations are performed to investigate the tip entry of CNTs into the cell with the code ESPRESSO [74]. Each DPPC lipid molecule is approximately modeled by three connected beads with one hydrophilic head-bead and two hydrophobic tail-beads (Fig. 2.9). To construct a bilayer of appropriate thickness, the bead diameter, $\sigma$, is set to be 1 nm. Some lipid molecules are selected to model receptors with strong attractive interactions with the MWCNTs. As shown in Figure 2.9, the CG model of a capped MWCNT is constructed from three SWCNTs with

all nearest and second nearest beads connected by harmonic spring with spring constant $k = 400\varepsilon$. The nearest neighbor distance of the beads on the outermost surface of CNTs is $2\sigma$. The bead-bead interactions are described by the following potentials:

$$
\begin{aligned}
U_{WCA}(r) &= 4\varepsilon\left[\left(\frac{b}{r}\right)^{12} - \left(\frac{b}{r}\right)^{6} + \frac{1}{4}\right] \quad \left(0 < r < r_{\text{cut}} = 2^{1/6} b\right), \\
U_{COS}(r) &= \begin{cases} -\varepsilon + U_{WCA}(r) & \left(r < r_{cut} = 2^{1/6}\sigma\right) \\ -\varepsilon \cos^2 \dfrac{\pi(r - r_{cut})}{2w} & \left(r_{cut} \le r \le r_{cut} + w\right) \end{cases}, \\
U_{FENE}(r) &= -\frac{1}{2} k_{FENE} r_{\infty}^2 \ln\left(1 - \frac{r^2}{r_{\infty}^2}\right) \quad \left(0 < r < r_{\infty}\right).
\end{aligned}
\tag{2.20}
$$

The nearest neighbor beads of lipid are connected by FENE bond with $k_{FENE} = 30\varepsilon$ and $r_{\infty} = 1.5\sigma$. The head bead is also connected with the second tail bead by a harmonic potential with rest length $r_0 = 4\sigma$ and force constant $k_{bend} = 10\varepsilon$. The non-bonded interaction parameters are listed in the Table 2.1.

**Table 2.1: Interaction between different bead types.**

| bead type | bead type | interaction | parameters |
|---|---|---|---|
| lipid/receptor head | lipid/receptor head | WCA | $b = 0.95\sigma$ |
| lipid/receptor head | lipid/receptor tail | WCA | $b = 0.95\sigma$ |
| lipid/receptor tail | lipid/receptor tail | COS | $b = \sigma$, $w = 1.6\sigma$ |
| lipid head | CNT | WCA | $b = 0.95\sigma$ |
| receptor head | CNT | COS | $b = \sigma$, $w = 1.6\sigma$ |
| lipid tail | CNT | WCA | $b = 0.95\sigma$ |
| receptor tail | CNT | WCA | $b = 0.95\sigma$ |

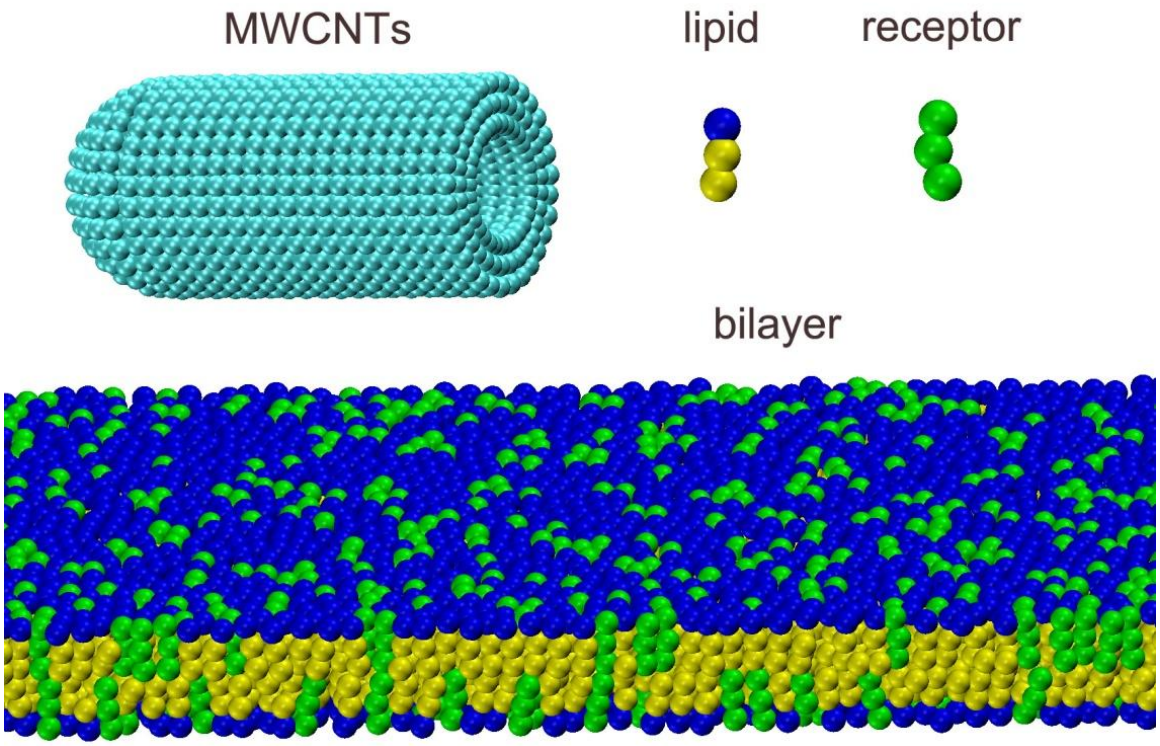


Figure 2.9: Schematic illustration of lipid and receptor molecules formed by one hydrophilic head-bead and two hydrophobic tail-beads. A flat patch of lipid bilayer spanning the simulation box consists of lipid and receptor molecules. The CG model of a capped multi-walled carbon nanotube (MWCNT) with diameter *d*=20 nm and length *L*=46 nm formed from three single walled carbon nanotubes.

The CGMD simulations are performed at constant temperature ($k_B T = 1.1\varepsilon$) and pressure with a dissipative particle dynamics (DPD) thermostat. A damping parameter $\Gamma = 1.0\,\varepsilon\tau/\sigma^2$ and a cut-off distance $d_{\text{cut}} = 3.0\sigma$ are used in the thermostat. The barostat controls the lateral tension of bilayer through altering the simulation box size in the plane of the bilayer. The damping parameter $\Gamma_{\text{A}} = 0.0001\varepsilon\tau/\sigma^4$ , piston mass $M = 0.0005\varepsilon\tau^2/\sigma^4$ and zero external pressure are used in the barostat. A similar procedure has been previously used to investigate the aggregation and vesiculation of membrane proteins [75].

### 2.2.2 Simulation results and discussions

Initially, the MWCNTs are arranged in close proximity above the surface of the bilayer which has a total of 16326 lipids and receptors with dimensions $100\sigma \times 100\sigma$. The angle between the axis of the MWCNT and the bilayer is set at $\theta_0$=45°. To investigate the influence of the density of receptors, we select different fractions of receptors $\phi = 0.25, 0.33, 1.0$ among all molecules that constitute the membrane. For $\phi = 0.25$, Figure 2.10A shows that the receptors (green) diffuse along the flat bilayer and aggregate around the MWCNT due to the attractive interaction between the beads of the receptors and the nanotube. With more and more receptors gathering and adhering to the surface of the MWCNT, the nanotube is pulled down and wrapped by the bilayer. Meanwhile, we see that the MWCNT spontaneously rotates and adjusts the entry angle to 90°. It will be shown shortly that this phenomenon is due to the relaxation of the elastic energy of the membrane which favors the 90° entry. For $\phi = 0.33$, however, Figure 2.10B shows that the MWCNT no longer rotates to 90° before it is fully wrapped. In the extreme case when $\phi = 1$, the membrane on the right side of the nanotube wraps around the tube much faster than that on the left side, leading to horizontal entry (Fig. 2.10C). In such an extreme case, diffusion of receptors is no longer needed for successful binding between the membrane and the tube, and the strong adhesive interaction on the right side of the rube becomes dominant compared to the elastic energy of membrane. As a result, the tube is pulled down to the membrane with a small entry angle. This process is also theoretically investigated in Reference [76]. Since the increase in density of receptors results in an increase in the aggregation speed of receptors, we conclude that there are two competing

kinetic processes during the MWCNT's entry: One is the nanotube's rotating induced by the membrane elastic energy, and the other is the difference of wrapping speeds on the two sides of the nanotube. When the former prevails, the final entry angle is close to 90 °. It should be pointed out that the extreme case in Figure 2.10C (the nonspecific interaction) would never happen in a real cellular system, because the density of receptors is usually small in specific interaction between the membrane and the WMCNT.

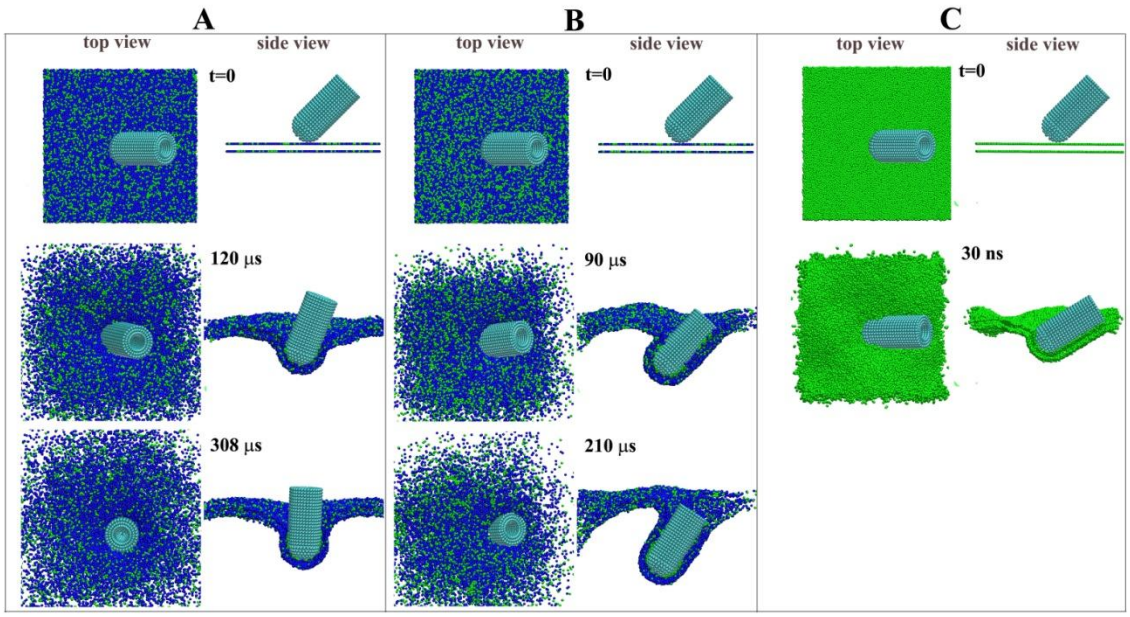


Figure 2.10: A sequence of snapshots of a MWCNT wrapped by a lipid membrane with initial entry angle $\theta_0$=45 °. The fractions of modeled receptors (green) are (**A**) $\phi = 0.25$, (**B**) $\phi = 0.33$, and (**C**) $\phi = 1$.

To investigate the influence of the initial entry angle $\theta_0$, we repeat the simulations with $\theta_0$=85 °. Figure 2.11A shows that at $t$=120 μs, the entry angle of the nanotube has not changed significantly. In the previous case of $\theta_0$=45 °, the nanotube is seen to have rotated by a large angle already at $t$=120 μs (Fig. 2.10A). This implies that the nanotube has larger rotating speeds at smaller entry angles. We also note that larger initial entry angles

result in 90 °entry at larger receptor densities. For example, when the initial entry angle is 85 °, the nanotube has enough time to rotate to 90 °entry even at $\phi$=0.33, (Fig. 2.11B). In the extreme case of $\phi = 1$, a rotation toward horizontal entry is observed, similar to the case of $\theta_0$=45 °.

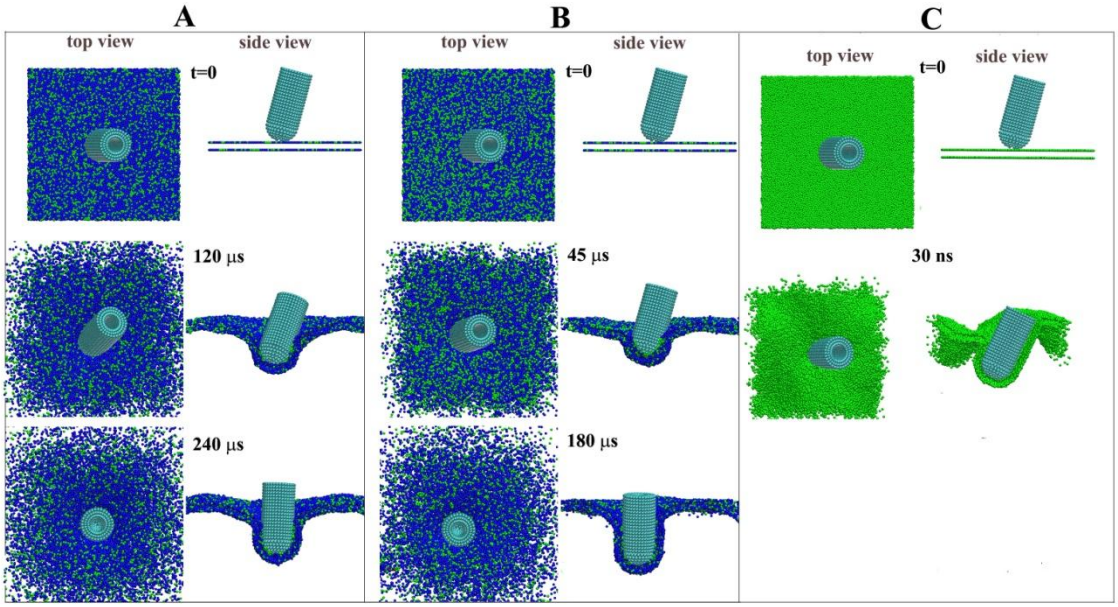


Figure 2.11: A sequence of snapshots of a MWCNT wrapped by a lipid membrane with initial entry angle $\theta_0$=85 °. The fractions of modeled receptors (green) are (**A**) $\phi = 0.25$, (**B**) $\phi = 0.33$, and (**C**) $\phi = 1$.

### 2.2.3 Theoretical modeling and discussions

The CGMD simulations have provided some insights into the mechanism of MWCNTs entry into the cell. The simulations suggest that the final entry angle of the nanotube is determined by a competition between the rotating and wrapping speeds of MWCNTs. However, due to the limitations of molecular dynamics simulation, the wrapping time scale in a real cellular system cannot be reached (~minutes). In the present CGMD

simulations, we have amplifed the wrapping speed by increasing the density of receptors as well as decreasing its size to accelerate the diffusivity. In this sesne, the CGMD simulations can only be used to qualitatively investigate the tip entry problem. Meanwhile, the viscosity of cytosol could be orders of magnitude larger than that of the extracellular medium [77] and is not realistically captured in the CGMD model. The receptor mediated wrapping of a nanoparticle by a cell membrane has been theoretically investigated in References [22, 78]. It was shown that the wrapping time can be expressed as $t_w = \frac{L_i d}{2\alpha^2 D}$, where $D$ is the diffusivity of receptor, $d$ is the diameter of the nanotube, $L_i$ is the length of the tube wrapped by the membrane, and $\alpha$ is the so-called "speed factor" determined by the balance of free energy as $e_{\mathrm{RL}} - \frac{1}{2} B \frac{1}{(d/2)^2 \xi_L} + \ln f(\alpha) - f(\alpha) + 1 = 0$, where $e_{RL} k_B T$ is the energy of a single receptor-ligand bond, $Bk_B T$ is the bending modulus of membrane, $f(\alpha) = \tilde{\xi} + \frac{\alpha^2 (1 - \tilde{\xi}) E_1(\alpha^2)}{\alpha^2 E_1(\alpha^2) - \mathrm{e}^{-\alpha^2}}$, $\tilde{\xi} = \xi_0 / \xi_L$ with $\xi_0$ and $\xi_L$ being the densities of receptor and ligand, and $E_1(z) = \int_z^\infty \frac{\mathrm{e}^{-u}}{u} \mathrm{d}u$. Here we emphasize that the curvature of the membrane and the radius of the nanotube have insignificant influence on the speed factor $\alpha$. In the following analysis, the speed factor is treated as identical on both sides of the nanotube. With the parameters selected as $D$=$10^3$~$10^4$ nm$^2$s$^{-1}$, $e_{RL} = 15$, $B$=20, $\xi_L = 5000$ μm$^{-2}$, $\tilde{\xi} = 0.1$, $d$=100 nm [22, 78], the wrapping time is shown in Figure 2.12A as a function of the wrapped length of the nanotube. It is seen that full wrapping of a 30 μm

long nanotube requires almost $2\times10^2$ seconds when $D$=$10^4$ nm$^2$s$^{-1}$ (Fig. 2.12A, blue line) and $2\times10^3$ seconds when $D$=$10^3$ nm$^2$s$^{-1}$ (Fig. 2.12A, red line).

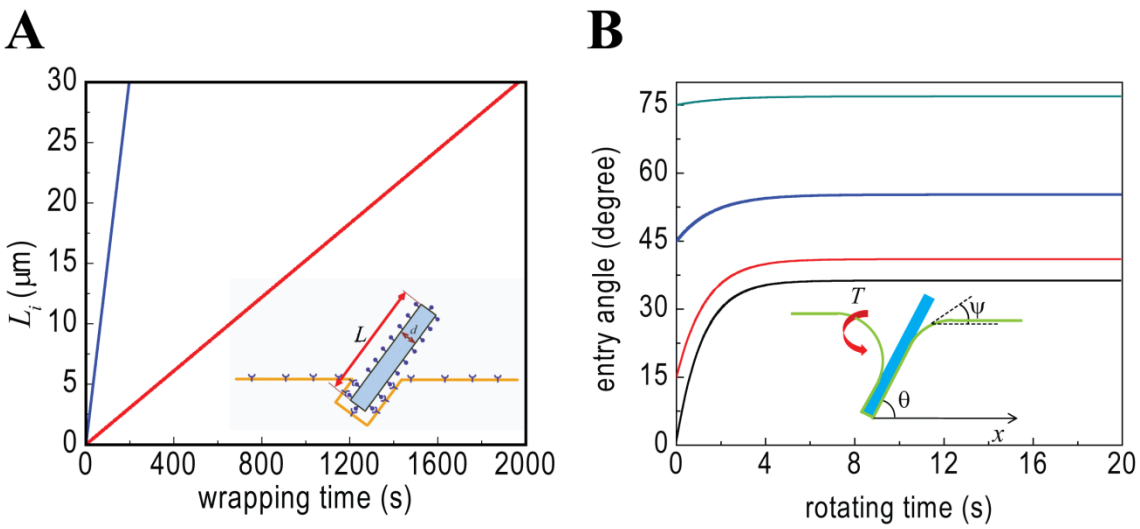


Figure 2.12: (**A**) The wrapping time as a function of the wrapped length of a MWCNT with the parameters selected as $e_{RL}=15$, $B$=20, $\xi_L=5000$ μm$^{-2}$, $\tilde{\xi}=0.1$, $d$=100 nm and $D$=$10^3$ (red line) or $10^4$ nm$^2$s$^{-1}$ (blue line). Inset is a schematic illustration of particle entry into a cell via receptor-mediated endocytosis. (**B**) The evolution of the entry angle of a MWCNT with initial entry angle $\theta_0$=1°, 15°, 45° and 75°. The other parameters are selected as $d$=100 nm, $L=L_i+L_e=30$ μm, $\eta_e=10^{-3}$ Pa s, $\eta_i=1$ Pa s, $\kappa=20\ k_BT$, $\sigma_t=0.001$ N/m. Inset is the schematic show of entry of MWCNTs into the bilayer with angle $\theta$ (2D). The curved bilayer exerts a torque $T$ onto the MWCNTs.

The rotating motion of a MWCNT partially wrapped by a lipid bilayer is attributed to the torque $T$ exerted by the curved bilayer (Fig. 2.12B). To express the torque in an explict closed formula, we select a 2D model to describe the balanced profile of the membrane. The profiles of the curved membrane on the right and left sides of the nanotube are described as $\psi_r=4\arctan\left[\exp\left(-s\sqrt{\sigma_t/\kappa}\right)\tan(\theta/4)\right]$ and $\psi_l=4\arctan\left[\exp\left(-s\sqrt{\sigma_t/\kappa}\right)\tan((\pi-\theta)/4)\right]$ [79], where $s$ is the arc length, $\psi$ is the angle between the $x$ axis and the tangent to the profile, $\theta$ is the final entry angle, $\kappa$ is the

bending modulus of membrane and $\sigma_t$ the membrane tension. The elastic energy per unit length stored inside the membrane is $E = E_1 + E_2 + E_0$ where $E_1 = 4\sqrt{\sigma_t \kappa}\left(2 - \sqrt{2}\sin\left(\frac{\theta}{2} + \frac{\pi}{4}\right)\right)$ is the energy stored in the free part of membrane, $E_2 = \sigma_t \frac{d}{2}\left[\pi - 2\sin\theta + (\pi - 2\theta_0)(1 - \cos\theta)\right]$ describes the tension energy within the contact region, $E_0$ is a reference value independent of $\theta$ and $\theta_0$ is the initial entry angle. More details of this part are described in Reference [76]. Subsequently the total energetic torque per unit length of the nanotube is calculated as $T = -\frac{dE}{d\theta} = 2\sqrt{2\sigma_t \kappa}\cos\left(\frac{\theta}{2} + \frac{\pi}{4}\right) + \sigma_t d\left(\cos\theta - \sin\theta\left(\frac{\pi}{2} - \theta_0\right)\right)$. It is seen that the torque depends on the entry angle $\theta$: The smaller the entry angle, the larger the torque. At nanoscale, the intra/extracellular enviroment is considered as a low Reynolds number medium where the inertia force is ignored and the applied force is balanced by the drag force. The rotating angular velocity is then expressed as $\frac{d\theta}{dt} = \frac{3Td}{4\pi\left[\frac{\eta_i L_i^3}{C_i} + \frac{\eta_e L_e^3}{C_e}\right]}$ [80], where $\eta_i$ and $\eta_e$ are the viscosities of intra- and extracellular environment, $L_i = 2\alpha^2 Dt/d$ and $L_e$ are the lengths of the nanotube inside and outside the membrane, $C_i = \ln p_i - 0.662 + 0.917/p_i - 0.05/p_i^2$ with $p_i = \frac{L_i}{d}$ and $d$ the diameter of nanotubes, and $C_e = \ln p_e - 0.662 + 0.917/p_e - 0.05/p_e^2$ with $p_e = \frac{L_e}{d}$. The differential equation is solved with $d$=100 nm, $L = L_i + L_e = 30$ μm, $\eta_e = 10^{-3}$ Pa s, $\eta_i = 1$ Pa s, $\kappa = 20\ k_B T$,

$\sigma_t = 0.001$N/m. Figure 2.12B shows the evolution of the entry angle as the nanotube enters the cell. The analysis shows that the entry angle can reach a steady-state value within 10s. The decreasing slope of the profiles indicates decreasing rotating speeds of the nanotube as it enters deeply into the cell. For low entry angles (e.g., $\theta_0$=1 °), the initial slope is larger than that of high entry angles (e.g., $\theta_0$=75 °), indicating the rotating speed is entry angle dependent, which is consistent with our CGMD simulations. At a very small initial entry angle, e.g. $\theta_0$=1 °, the nanotube has a strong tendency to rotate to a large entry angle. Compared with the time scale for full wrapping (200~2000 s), the rotating time scale (10 s) is one or two orders of magnitude smaller. So apparently the rotating motion is relatively fast that tip entry is a favorable way for MWCNTs to enter the cell.

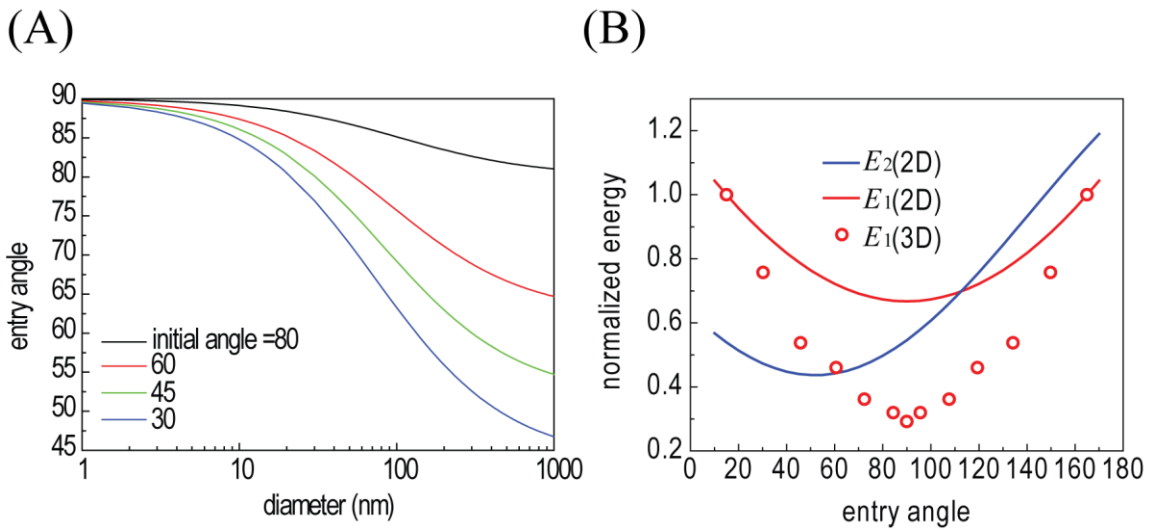


Figure 2.13: **(A)** The final entry angle corresponding to the steady state is dependent on the diameter and initial contact angle. **(B)** Decomposed elastic energy normalized by $E_1(\theta = 15^\circ)$ with parameters selected as $\theta_0$=45 ° and $\sigma_t d^2/\kappa = 1$.

It is worth pointing out that in CGMD simulations the final entry angle is nearly 90 ° and independent of the initial entry angle. However in our 2D theoretical modeling,

the final entry angle is greatly dependent on the initial entry angle: For small initial entry angle, the final angle can deviate significantly from the 90 °. We attribute this discrepancy to the following two factors. One is that in CGMD simulations the diameter of the nanotube is 20 nm, much smaller than the value selected in our theoretical modeling (100 nm). As shown in Figure 2.13A, for nanotubes of smaller sizes, the final entry angle is closer to 90 ° with less sensitivity to the initial entry angle. Another factor is that the CGMD simulations are 3D while our theoretical model is 2D. To see the difference in 2D and 3D models, we compare the elastic energy stored in the free part of the membrane $E_1$ calculated by the 2D model and from CGMD simulations. Figure 2.13B shows that the minimum of $E_1$ occurs at 90 ° while that of $E_2$, the membrane tension energy within the contact region, occurs at a smaller angle. In the 2D case, the minimum total energy, the sum of $E_1$ and $E_2$, occurs at an intermediate value between the two angles, corresponding to the final entry angle. In the 3D case, we calculate the $E_1$ through CGMD simulations and find that the well of the energy profile is much deeper than that in the 2D case. Assume that $E_2$ does not change significantly in 2D and 3D, we conclude that the elastic energy $E_1$ stored in the free part of the membrane becomes more dominant in 3D, which renders the final entry angle near 90 °.

### 2.3 Role of particle stiffness in cellular uptake

Recent experiments have also illustrated the effects of elastic deformation on cellular uptake of nanoparticles. It was found that human immunodeficiency virus (HIV) particles regulate their mechanical properties at different stages of the life cycle through internal

morphological reorganization: They become stiffer during uptake and softer after fusing from the cell [23]. Beningo and Wang [81] have shown that phagocytosis of soft microparticles can be weakened by deformation. In drug delivery, softer, more flexible particles are expected to inhibit phagocytosis, leading to longer lifetime of particles in circulation. These experimental observations are calling for efforts to understand the effect of elastic deformation of vesicle and nanoparticles on cellular uptake.

To simulate the wrapping of a particle in 2-dimension (2D), we adopt a simple carbon nanotube (CNT)-graphene ribbon (GR) system which has the same energy profile as an elastic cylindrical shell-membrane system. Driven by the adhesion energy, the GR acts as a one-atom-thick membrane wrapping around the CNT. The total elastic energy of GR is composed of in-plane stretching energy and bending energy, similar to that of the cell membrane. In the MD simulations, periodic boundary conditions are imposed in the axial direction of CNT during the wrapping process. The LAMMPS [82] code is used with the second generation of Brenner's potential [83, 84] to model the graphene and CNT. The interaction between CNT and graphene is described by the Lennard-Jones potential ($4\varepsilon\left[\left(\frac{\sigma}{r}\right)^{12}-\left(\frac{\sigma}{r}\right)^{6}\right]$) with force constant $\varepsilon$. An extra CHARMM style dihedral interaction ($K(1+\cos(n\phi-d))$) is enforced on the CNT to tune its rigidity by adjusting the force constant $K$. The GR is stretched by tension force $\sigma_t$ on its two free sides. For simplicity, the temperature is fixed at 1 K in all simulations to eliminate the thermal effect. Through tuning the three parameters, $\varepsilon$, $K$, and $\sigma_t$, the system can simulate all the situations in which different particle-membrane interaction energy $\gamma$, particle stiffness $\kappa_0$, and membrane tension $\sigma_t$ are investigated.

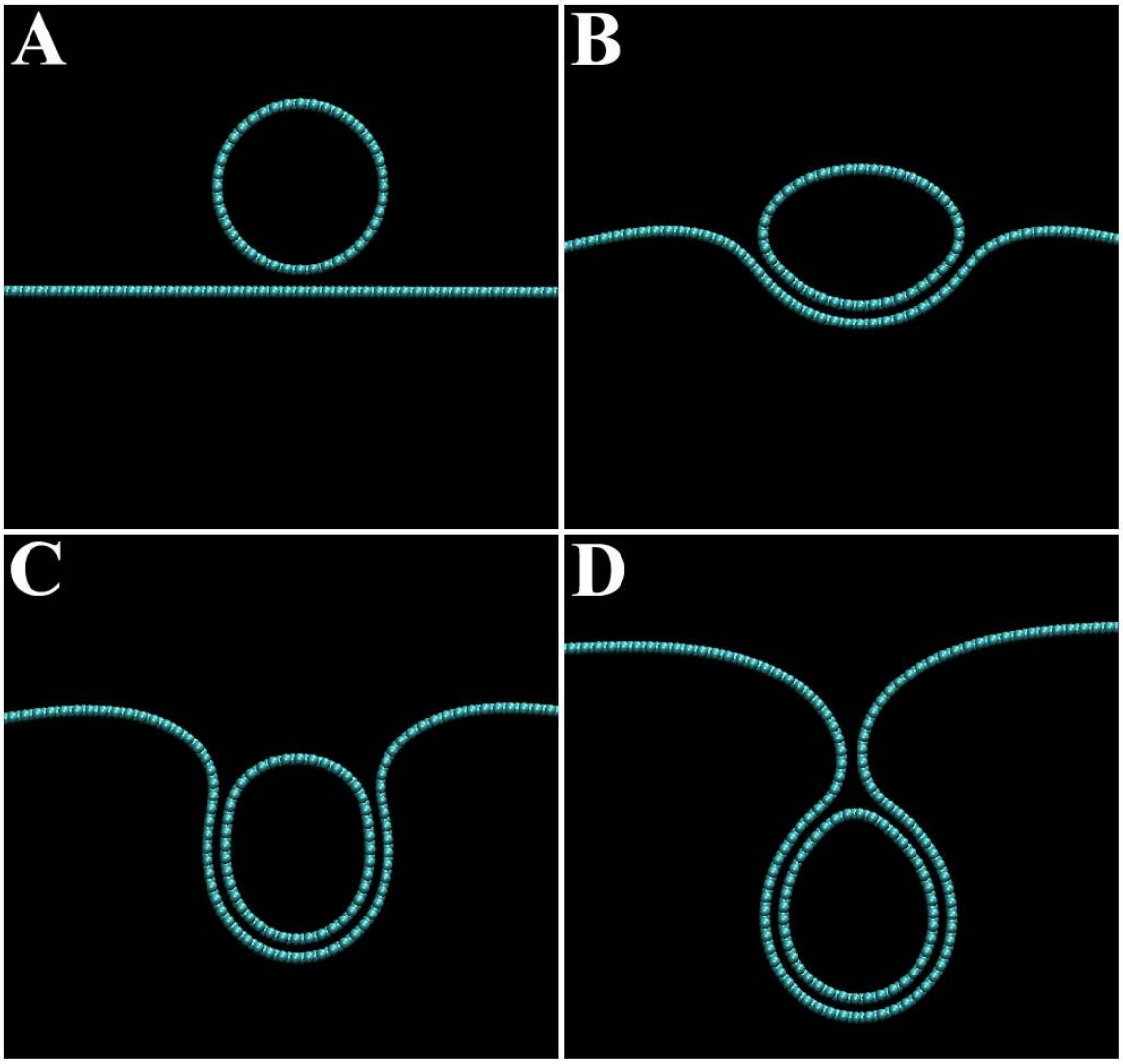


Figure 2.14: A sequence of snap shots of a CNT being wrapped by a graphene ribbon. The wrapping degree is (**A**) 0, (**B**) 0.5, (**C**) 0.75, and (**D**) 1.0. The parameters are selected as $\bar{\gamma} = 2\gamma a^2/\kappa = 10$ , $\bar{\sigma}_t = 2\sigma_t a^2/\kappa$ , $\kappa_0/\kappa = 1$, where 2*a*=3 nm is the diameter of CNT and $\kappa = 0.17$ nNnm the bending stiffness of GR.

Figure 2.14 shows a sequence of snapshots of a CNT being wrapped by a GR. It is seen that the CNT has different conformation at different wrapping degree. As the wrapping degree increases, the shape of the vesicle changes from a spreading ellipse (Fig. 2.14B) to a dangling drop-like shape (Fig. 2.14C). Decreasing the stiffness of the CNT

leads to more severe deformation. Most interestingly, under fixed membrane tension and interaction energy between CNT and GR, it is found that the CNT cannot be fully wrapped as its bending stiffness decreases to a critical value. This finding indicates that the stiffness of particles could play essential roles in their uptake.

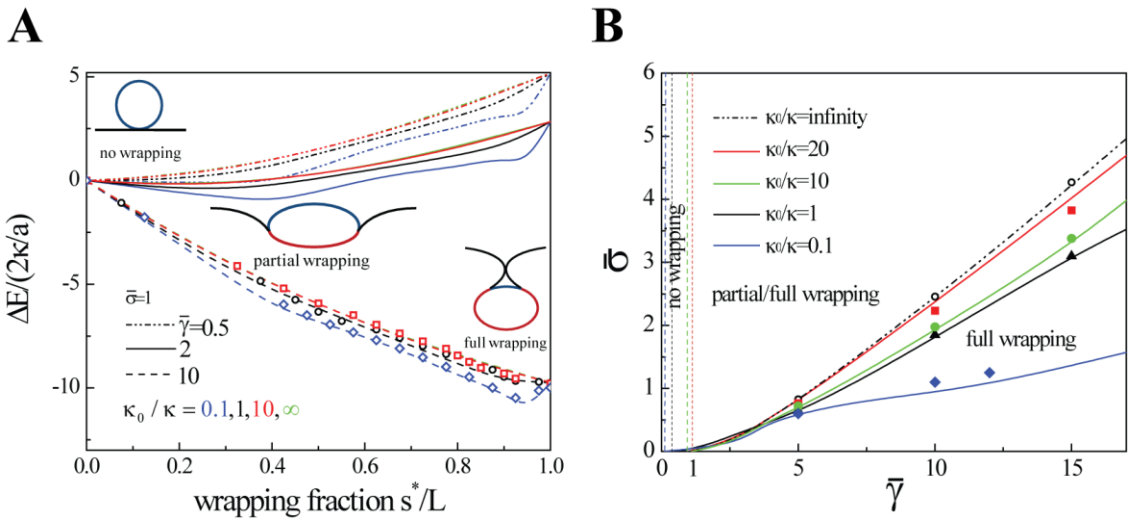


Figure 2.15: **(A)** Potential energy of the wrapping system as a function of the wrapping degree. **(B)** Wrapping phase diagram in the plane of normalized adhesion constant $\bar{\gamma}$ and surface tension $\bar{\sigma}$ for different $\kappa_0/\kappa$. The scatters are from MD simulations and lines from theoretical modeling.

To elucidate the mechanism of how the particle stiffness influences the wrapping process, we calculate the potential energy of the system. As shown in Figure 2.15A, the potential energy at different wrapping degrees is calculated. It is seen that only when the energy monotonically decreases as the wrapping fraction increases can the CNT be fully wrapped. If the energy monotonically increases, there is no wrapping; if the energy first decreases and then increases, there is partial wrapping. Based on this energy criterion, we construct a phase diagram shown in Figure 2.15B. In the $\bar{\sigma}_t - \bar{\gamma}$ phase diagram, it is seen that under fixed tension, the wrapping degree transits from no wrapping to partial

wrapping, and partial wrapping to full wrapping as the CNT-GR interaction energy increases. Meanwhile, the stiffness of CNT greatly influences the wrapping degree. The phase diagram indicates that full wrapping of a softer CNT requires lower tension and stronger CNT-GR interaction. Therefore, it is more difficult for a cell membrane to engulf a softer particle. This study thus clearly shows that the stiffness plays as important roles in the cellular uptake of nanoparticle as the tension of membrane and the interaction energy between membrane and particle.

Adopt a framework developed by Helfrich et al. [85-87], we also theoretically investigate the effect of stiffness of particle on cellular uptake. Through the variation of the free energy of the system which consists of bending energy of the membrane and particle, tension energy of the membrane as well as interaction energy between the membrane and particle, the shape functions of the membrane and particle are obtained and numerically solved with provided boundary conditions. Further details of the theoretical model are left to Reference [88]. We find the MD simulation results agree very well with the theoretical predictions.

# *Chapter 3*

# *Basic structure of carbon nanoscrolls*

### 3.1 Theoretical Model

The remaining part of this thesis will be dedicated to the mechanics of carbon nanoscrolls (CNSs), a class of carbon nanomaterials constructed from single sheets of graphene. Although CNSs were experimentally discovered in 2003 [24, 29] (see also Reference [25-28]) and also investigated extensively by molecular dynamics simulations [30-36], quantitative theories describing their existence and assembly process are still lacking. In the following, we present a theory on the dynamics and equilibrium state of this assembly process [89, 90].

Figure 3.1 shows a graphene sheet of length *B* and width *L* rolled up into a scroll with inner core radius $r_0$, outer radius *R* and interlayer spacing *h* which can be described by a radial function as

$$r = r_0 + \frac{h}{2\pi}\vartheta, \tag{3.1}$$

The total length of the graphene sheet is

$$B \approx \int_0^{2\pi N} \left( r_0 + \frac{h}{2\pi} \vartheta \right) \mathrm{d}\vartheta = 2\pi r_0 N + \pi h N^2 , \tag{3.2}$$

where $N$ is the number of coils.

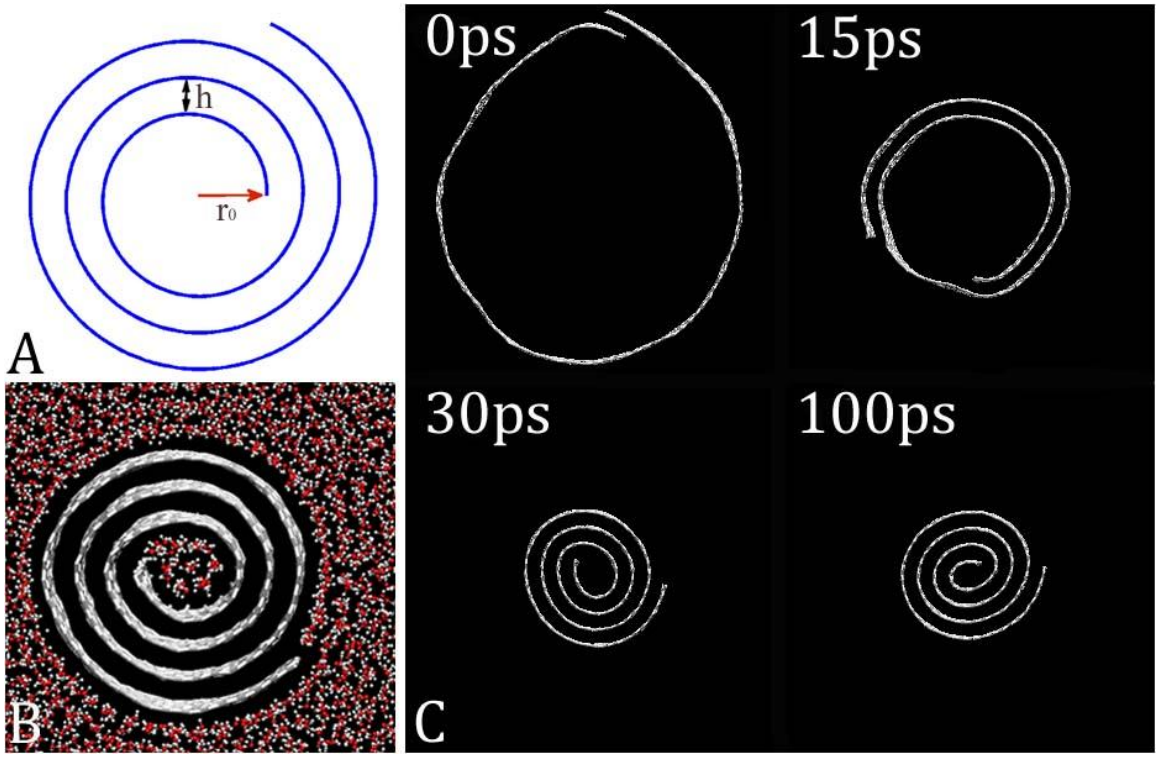


Figure 3.1 (**A**) Carbon nanoscroll with inner core radius $r_0$ and interlayer spacing $h$. (**B**) Equilibrium core size in water. (**C**) MD snapshots on the spontaneous assembly of a zigzag graphene strip ($3 \times 24\,\mathrm{nm}^2$) winding at 0, 15, 30, 100 ps. [89]

The elastic energy per unit area in the graphene is taken as

$$\frac{\mathrm{d}W}{\mathrm{d}A}(r) = \frac{D}{2}\frac{1}{r^2} . \tag{3.3}$$

where $D$ is the bending stiffness. Note that $\mathrm{d}A \approx L r \mathrm{d}\vartheta$. The total elastic energy in the scroll is thus obtained by integrating Eq. (3.3) as

$$W = \frac{\pi DL}{h} \ln\left(\frac{R}{r_0}\right), \tag{3.4}$$

Consider an infinitesimal change in the core radius $r_0$ of the scroll. The change in strain energy would be

$$\mathrm{d}W = \frac{\pi DL}{h}\left(\frac{\mathrm{d}R}{R} - \frac{\mathrm{d}r_0}{r_0}\right). \tag{3.5}$$

It can be shown that

$$\frac{\mathrm{d}N}{\mathrm{d}r_0} = -\frac{N}{R}, \tag{3.6}$$

$$\frac{\mathrm{d}R}{\mathrm{d}r_0} = 1 + \frac{\mathrm{d}N}{\mathrm{d}r_0} h = 1 - \frac{Nh}{R} = \frac{r_0}{R}. \tag{3.7}$$

Therefore, the change in elastic strain energy can be expressed as

$$\mathrm{d}W = -\frac{\pi DL}{h} \frac{R^2 - {r_0}^2}{R^2} \frac{\mathrm{d}r_0}{r_0}, \tag{3.8}$$

On the other hand, the change in total surface energy of the scroll is

$$\mathrm{d}\Gamma = 2\pi\gamma L\left(\mathrm{d}r_0 + \mathrm{d}R\right) = 2\pi\gamma L\left(1 + \frac{r_0}{R}\right)\mathrm{d}r_0, \tag{3.9}$$

where $\gamma$ is the surface energy per unit area. The virtual work associated with an infinitesimal perturbation in the core size due to the pressure is

$$\mathrm{d}\Phi = -p_i 2\pi L r_0 \mathrm{d}r_0 + p_e 2\pi LR\mathrm{d}R = -2\pi L r_0 \mathrm{d}r_0 p, \tag{3.10}$$

where $p = p_i - p_e$. Therefore, the change in free energy $E$ associated with a "virtual core expansion" is

$$\frac{\mathrm{d}E}{\mathrm{d}r_0} = \frac{\mathrm{d}W}{\mathrm{d}r_0} + \frac{\mathrm{d}\Gamma}{\mathrm{d}r_0} + \frac{\mathrm{d}\Phi}{\mathrm{d}r_0}. \tag{3.11}$$

The equilibrium core size can be calculated by setting $\mathrm{d}E = 0$, which yields

$$2\pi\gamma\left(1+\frac{r_0}{R}\right) = \frac{\pi D}{h}\frac{R^2 - r_0^{\,2}}{R^2}\frac{1}{r_0} + 2\pi r_0 p\,. \tag{3.12}$$

This leads to the following equation governing the core size of the CNS,

$$\frac{2\gamma h}{D} = \frac{1}{r_0} - \frac{1}{R} + \frac{2hp}{D\left(1/r_0 + 1/R\right)}, \tag{3.13}$$

or

$$p_i - p_e = \frac{D}{2h}\left(\frac{2\gamma h}{D} - \frac{1}{r_0} + \frac{1}{R}\right)\left(\frac{1}{r_0} + \frac{1}{R}\right). \tag{3.14}$$

Together with the mass conservation equation

$$B = \frac{\pi}{h}\left(R^2 - r_0^{\,2}\right), \tag{3.15}$$

the equilibrium core radius $r_0$ and the outer radius $R$ of the scroll can be determined under fixed $B$, $h$, $p$, $D$, and $\gamma$.

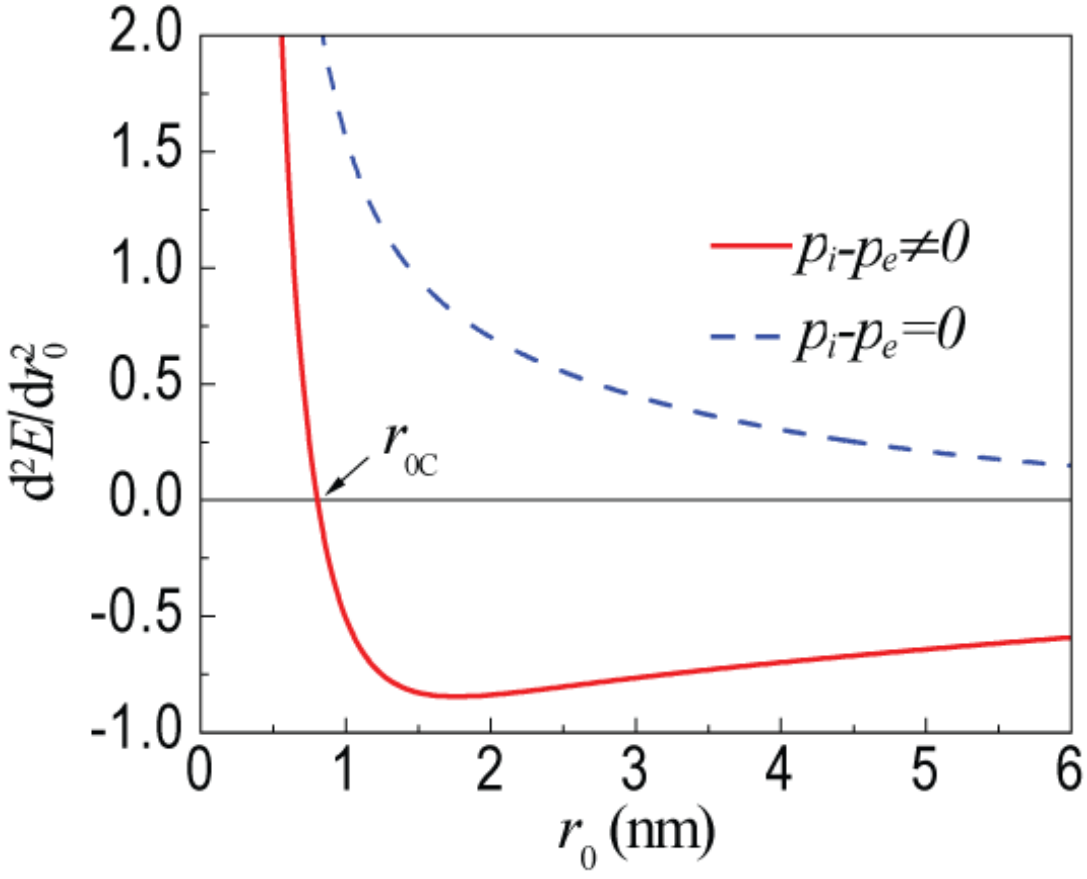


Figure 3.2: Second derivative of free energy of a CNS with respect to its core size. The dash line is for the case without pressure difference ( $p_i - p_e = 0$ ) and solid line for a finite pressure difference ( $p_i - p_e \neq 0$ ). [90]

The stability of the system requires $\frac{\mathrm{d}^2 E}{\mathrm{d}r_0^2} \geq 0$. Under constant pressure, this condition is reduced to

$$\frac{\mathrm{d}^2 E}{\mathrm{d}r_0^2} = \frac{DBL}{R^2 r_0^2} + \frac{2DBL}{R^4} + 2\pi\gamma L\left(\frac{1}{R} - \frac{r_0^2}{R^3}\right) - 2\pi L\left(p_i - p_e\right) \geq 0. \tag{3.16}$$

Taking the parameters as $D$=0.11 nN·nm, $\gamma = 0.4$ nN/nm, $h$=0.34 nm, $B$=200 nm, Figure 3.2 shows the second derivative of free energy with respect to the core size. In the

absence of a pressure difference ( $p = p_i - p_e = 0$ ), $\frac{\mathrm{d}^2 E}{\mathrm{d}r_0^2}$ is always greater than zero, indicating that the equilibrium configuration of CNS is stable. Figure 3.3A shows how the surface energy, the bending stiffness, the interlayer spacing of graphene and the length of graphene sheet influence the core size of the CNS. Figure 3.3B plots the evolution of potential energy (elastic energy plus surface energy) as a function of the core size. The results shown in Figures 3.2 and 3.3 clearly indicate that there exists a stable configuration of CNS with an equilibrium core size.

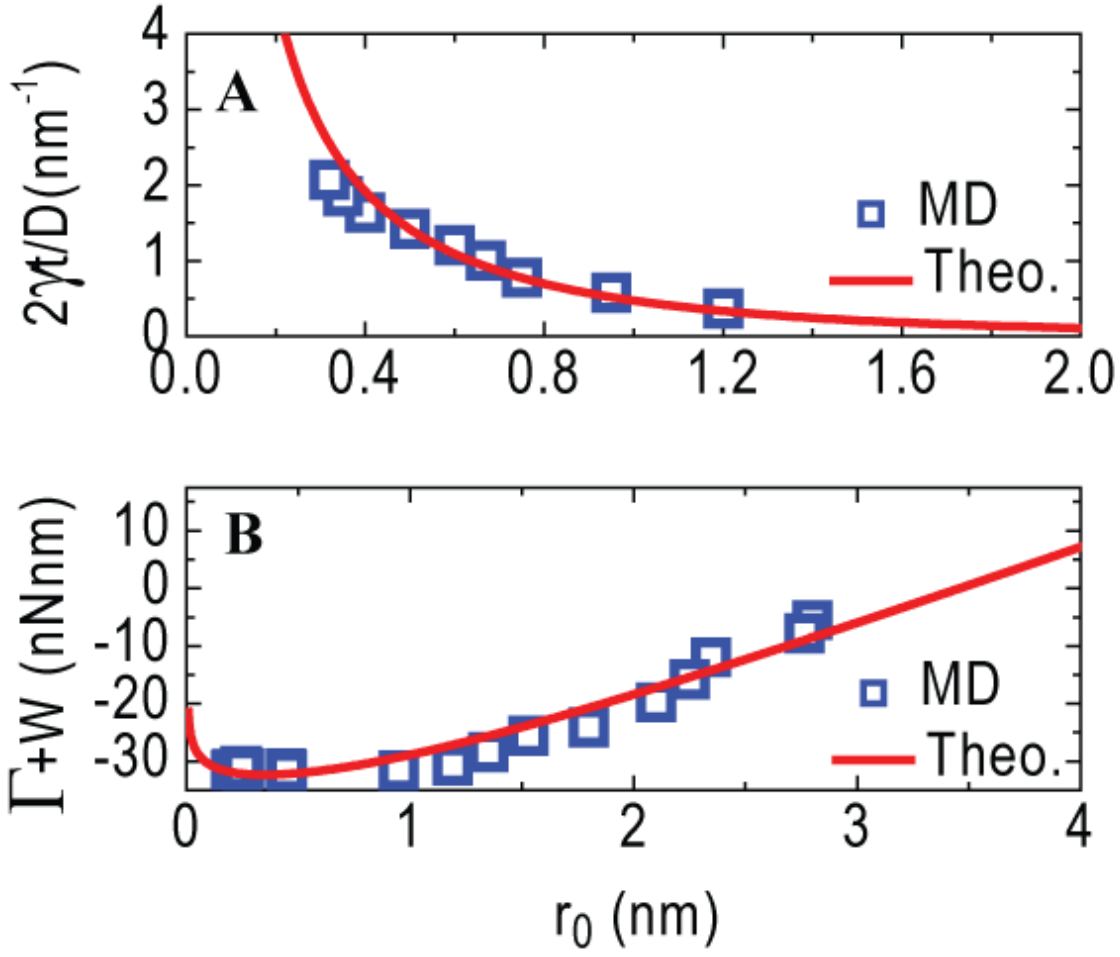

Figure 3.3: (**A**) The ratio between surface energy and bending modulus of graphene as a function of the CNS core size. (**B**) The potential energy as a function of the core size. All results are obtained in vacuum. Blue squares are the MD results and red line is the theoretical prediction. [89]

Under constant pressure $p = p_i - p_e \neq 0$, however, $\frac{\mathrm{d}^2 E}{\mathrm{d}r_0^2}$ is greater than zero only when the core size is below some critical value $r_{0C}$ (Fig. 3.2). This indicates that there is a critical pressure, beyond which the CNS becomes unstable under constant pressure. To further investigate the influence of pressure on the core size of CNS, a critical radius $r_0 = r_{0C}$ for unstable expansion under constant pressure is determined from

$$\frac{\mathrm{d}p(r_0)}{\mathrm{d}r_0} = \gamma\left(-\frac{1}{r_0^2} - \frac{r_0}{R^3}\right) + \frac{D}{h}\left(\frac{1}{r_0^3} - \frac{r_0}{R^4}\right) = 0. \tag{3.17}$$

Inserting $r_{0C}$ into Eq. (3.14) yields the critical pressure as

$$p_C = p(r_0 = r_{0C}). \tag{3.18}$$

Closed form solutions exist in the two asymptotic limits, corresponding to "thin" or "thick" CNSs. For thick CNSs, $R = r_0\sqrt{1+\alpha}$ where $\alpha = \frac{Bh}{\pi r_0^2} \to \infty$ (note that $\alpha$ is the ratio between the cross-sectional area of the CNS and that of its inner core); accordingly, Eq. (3.14) becomes $p(r_0) \approx \frac{\gamma}{r_0} - \frac{D}{2hr_0^2}$. In the absence of pressure, setting $p = 0$ gives the equilibrium core radius $r_{0e} \approx \frac{D}{2\gamma h}$. The critical core radius for unstable expansion under constant pressure can be derived according to Eq. (3.17) as

$$r_{0C} \approx \frac{D}{\gamma h} = 2r_{0e}. \tag{3.19}$$

The corresponding critical pressure is

$$p_C \approx \frac{\gamma^2 h}{2D}. \tag{3.20}$$

For thin CNSs, $R = r_0\sqrt{1+\alpha}$ with $\alpha = \frac{Bh}{\pi r_0^2} \to 0$; Eq. (3.14) becomes $p(r_0) \approx \frac{2\gamma}{r_0} - \frac{BD}{2\pi r_0^4}$.

For $p = 0$, the equilibrium core radius is $r_{0e} \approx \left(\frac{BD}{4\pi\gamma}\right)^{1/3}$. The critical core radius for unstable expansion under constant pressure is

$$r_{0C} \approx \left(\frac{BD}{\pi\gamma}\right)^{1/3} = 4^{1/3} r_{0e}. \tag{3.21}$$

The corresponding critical pressure is

$$p_C \approx \frac{3}{2}\left(\frac{\gamma^4 \pi}{BD}\right)^{1/3}. \tag{3.22}$$

Figure 3.4 shows the predicted equilibrium core size as a function of the pressure. As the core of CNS is expanded, the pressure increases first, reaches the peak at a critical core radius, and then drops. The asymptotic results for thick and thin CNSs are indicated as crosses in Figure 3.4. It is seen that the pressure used to expand the core of a thick CNS with large graphene length *B* is generally smaller than that used for a thin CNS, indicating a counterintuitive result that it is easier to expand a thick CNS to a specific core size than a thin CNS.

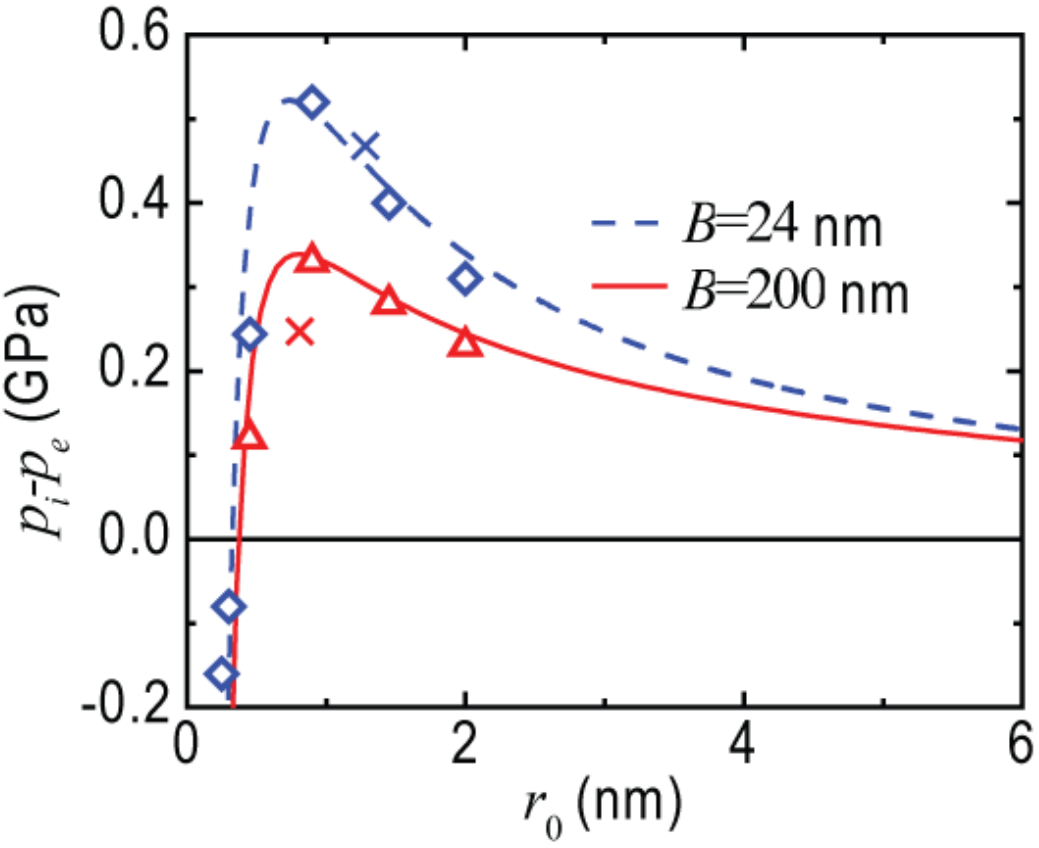


Figure 3.4: Pressure difference vs equilibrium core size of CNSs for different graphene lengths calculated from theory (line) and MD simulations (scatters). The crosses are the asymptotic solutions for thick and thin CNSs. [90]

To investigate the constitutive behavior of a pressurized CNS, Eq. (3.14) is rewritten as

$$p_i - p_e = \gamma\left(\sqrt{\frac{\pi L}{V - BhL}} + \sqrt{\frac{\pi L}{V}}\right) - \frac{DB\pi L^2}{2V(V - BhL)}, \tag{3.23}$$

where $V = \pi R^2 L$. Figures 3.5A and 3.5B show the pressure difference as a function of volume, with result showing similar features as Figure 3.4. The biaxial modulus of the CNS can be defined as

$$K = -V\frac{\partial p}{\partial V} = \frac{\gamma}{2}\left(\sqrt{\frac{\pi L}{V}} + \sqrt{\frac{\pi L V^2}{(V-BhL)^3}}\right) - \frac{BD\pi L^2}{2(V-BhL)^2} - \frac{BD\pi L^2}{2V(V-BhL)}. \quad (3.24)$$

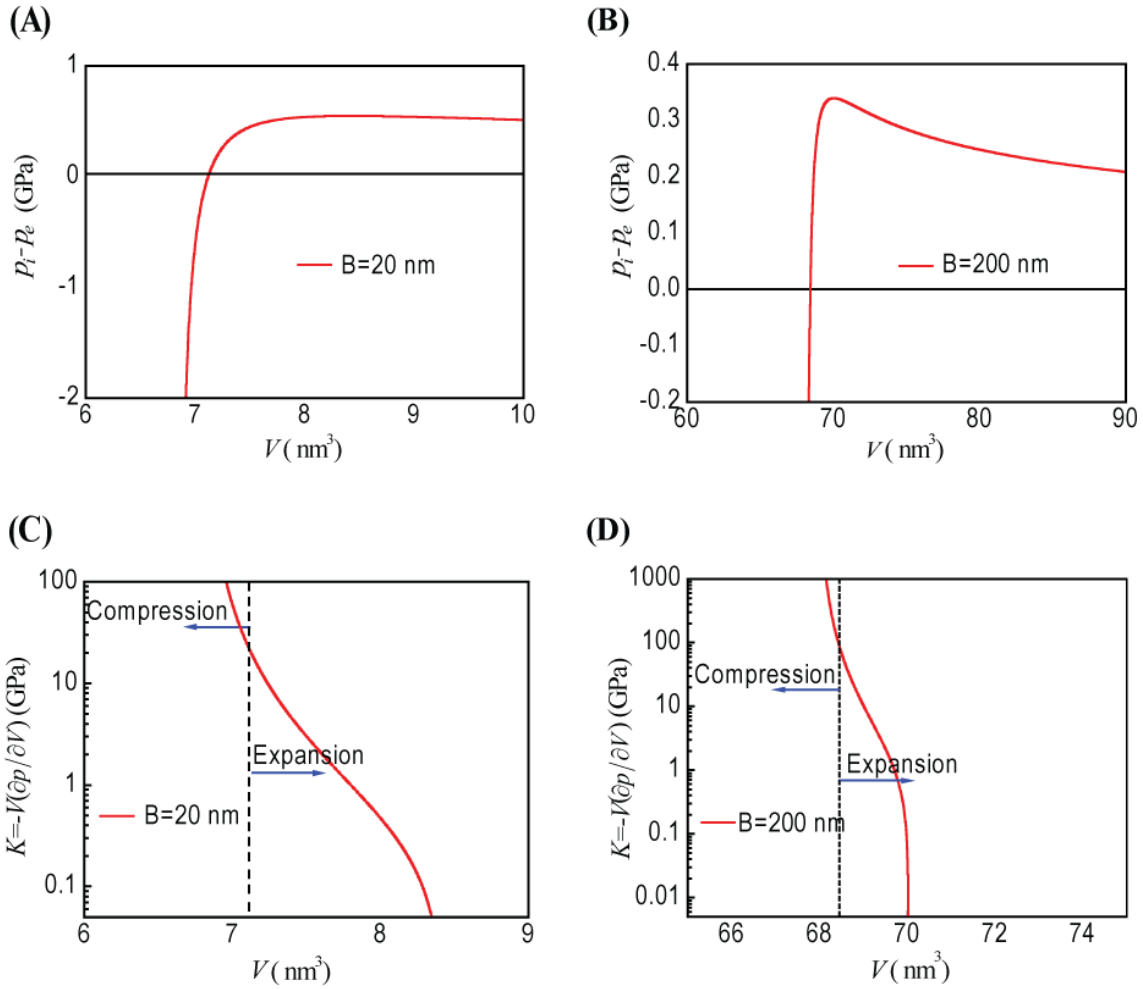


Figure 3.5: Pressure difference as a function of volume of a CNS with two different graphene length (**A**) *B*=20 nm and (**B**) *B*=200 nm. The biaxial modulus of the CNS as a function of volume for (**C**) *B*=20 nm and (**D**) *B*=200 nm. The dash lines indicate the volume when $p_i - p_e = 0$. [90]

Figures 3.5C and 3.5D show that the biaxial modulus of a CNS varies with its volume. The dash lines indicate the volume when $p_i - p_e = 0$. It is seen that the biaxial modulus

increases as the core is compressed and decreases as the core is expanded. When $p_i - p_e = 0$, the biaxial modulus is 20 GPa for *B*=20 nm and 80 GPa for *B*=200 nm. We would like to point out that these values are greatly affected by the surface energy of the CNS. In Figure 3.5C, the surface energy has been taken as $\gamma = 0.4$ nN/nm, and the biaxial modulus is 20 GPa; decreasing the surface energy to $\gamma = 0.2$ nN/nm reduces the biaxial modulus to 3 GPa.

### 3.2 Molecular dynamics simulation verification

Molecular dynamics (MD) simulations are performed and the results show that the assembly of CNS occurs very fast (Figure 3.1C) in absence of pressure. The equilibrium core size varies with different environment, large in water (Figure 3.1B) and small in vacuum (Figure 3.1C), for instance. The package Gromacs 4 [91] is used here to simulate the formation of CNSs from a graphene sheet. The graphene is described by a Morse bond, a harmonic cosine term for the bond angle, a cosine term for torsion and a Lennard-Jones (L-J) term for the van der Waals (vdW) interaction as [92]

$$\begin{aligned} U\left(r_{ij},\theta_{ijk},\phi_{ijkl}\right) = {} & K_{Cr}\left[e^{-k_C\left(r_{ij}-r_C\right)}-1\right]^2 + \frac{1}{2}K_{C\theta}\left(\cos\theta_{ijk}-\cos\theta_C\right)^2 \\ & + \frac{1}{2}K_{C\phi}\left(1-\cos 2\phi_{ijkl}\right) + 4\varepsilon_{CC}\left[\left(\frac{\sigma_{CC}}{r_{ij}}\right)^{12} - \left(\frac{\sigma_{CC}}{r_{ij}}\right)^{6}\right], \end{aligned} \tag{3.25}$$

where $k_C$ defines the steepness of Morse potential well, $r_{ij}$ denotes distance between two bonded atoms, $\theta_{ijk}$ and $\phi_{ijkl}$ are the bending and torsional angle, $r_C, \theta_C$ and $\phi_C$ are the reference geometrical parameters for graphene, $K_{Cr}, K_{C\theta}$ and $K_{C\phi}$ are the force constants of stretching, bending and torsion, respectively, and $\sigma_{CC}$ and $\varepsilon_{CC}$ are the L-J parameters

for carbon. The spontaneous assembly of CNS is simulated in both vacuum and water. For the latter case, the graphene strips are solvated in a periodic $4\times10\times10$ nm orthorhombic box with Tip3p water [93]. The electrostatic interaction of water solvent is evaluated by the particle mesh Ewald method (PME) [94, 95].

**Table 3.1: Parameters of interaction potential used in the molecular dynamics simulations.** [92]

| | | |
|---|---|---|
| $K_{Cr} = 47890\text{kJmol}^{-1}\text{nm}^{-2}$ | $r_C = 0.142\text{nm}$ | $k_C = 21.867\text{nm}^{-1}$ |
| $K_{C\theta} = 562.2\,\text{kJmol-1}$ | $\theta_C = 120^0$ | |
| $K_{C\phi} = 25.12\ \text{kJmol-1}$ | $\phi_C = 180^0$ | |
| $\varepsilon_{CC} = 0.4396\ \text{kJmol-1}$ | $\sigma_{CC} = 0.385\text{nm}$ | |
| $\varepsilon_{CO} = 0.529\ \text{kJmol-1}$ | $\sigma_{CO} = 0.35\,\text{nm}$ | |

The water-graphene interaction is described by the L-J potential with parameters $\sigma_{CO}$ and $\varepsilon_{CO}$. Unless mentioned elsewhere, all the simulation parameters are listed in Table 3.1. Room temperature (300 K) and atmospheric pressure (1 bar) are maintained in all simulations.

To investigate the effect of chirality on the CNS assembly, three deferent types of graphene strips, zigzag, armchair and chiral, are selected in the present simulations. To obtain the initial configuration shown in Figure 3.1C (t=0 ps), external forces are initially applied to bring the two ends of a planar strip to a close vicinity. Thereafter the forces are removed and the system is set-free. The snapshots of the MD trajectory for a zigzag graphene ( $3\times24\,\text{nm}^2$ ), shown in Figure 3.1C, indicate that the graphene strip spontaneously winds into CNSs and the winding process occurs very fast. The first loop is completed in $t = 15\,\text{ps}$ and three loops have already formed at $t = 30\,\text{ps}$. After 50 ps,

both the inner and outer radii have reached equilibrium, indicating the end of winding. The interlayer spacing is kept at a constant value 0.34 nm during the winding, exactly the same as that of the multiwalled carbon nanotube. The evolutions of the inner and outer radii are plotted in Figure 3.6 A, which indicates the speed of winding. To reveal the physical mechanism of the winding process, we plot the graphene-graphene interaction energy in Figure 3.6 B. At the initial state, the bending energy of the graphene is small because of the large radii. At this stage, the interaction energy dominates and drives the winding of the scroll. This process continues until the driving force is equivalent to the resistance force induced by the bending energy. To investigate the effect of graphene chirality, two additional graphene strips, armchair ($3\times 24\,\mathrm{nm}^2$) and chiral ($2.4\times 23\,\mathrm{nm}^2$), are used and the simulations are repeated. The similarly fast winding speed and the nearly same equilibrium core size suggest that the spontaneous winding of graphene is chirality independent. We also performed a simulation with a wider zigzag graphene strip ($6\times 24\,\mathrm{nm}^2$). The results are similar, indicating that the effect of scroll width is negligible.

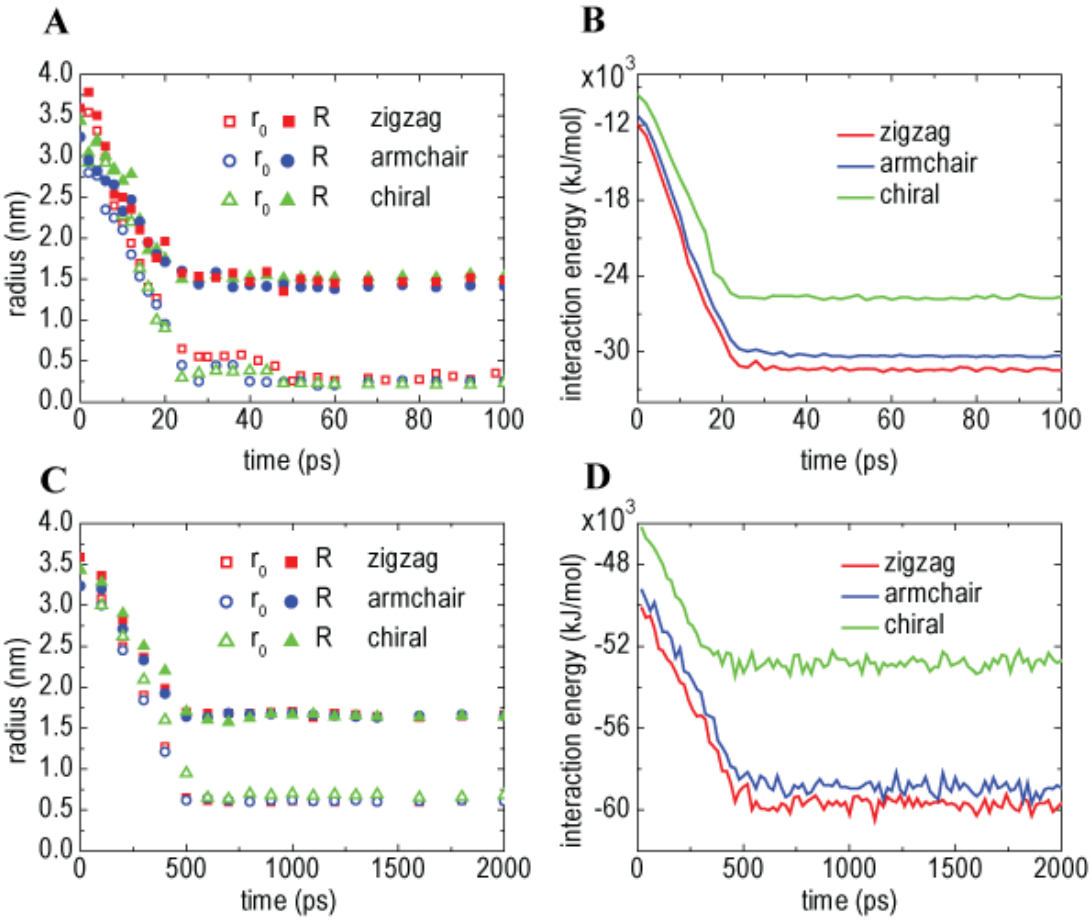


Figure 3.6: (**A**) The simulated inner and outer radii of selected CNS in vacuum as a function of the simulation time. Three types of graphene strips are simulated here: zigzag, armchair and chiral. (**B**) The simulated evolution of graphene-graphene interaction energy in vacuum as a function of time in the winding process. The steep slope at the initial state indicates that the surface energy of graphene is dominant. (**C**) The simulated inner and outer radii of selected CNS in water as a function of the simulation time. (**D**) The simulated evolution of the total interaction energy as a function of time. Here the total interaction energy is taken to be the sum of graphene-graphene, water-water and graphene-water interaction energy. [89]

In a box of water solvent, the winding process is slower because water molecules have to be squeeze out of the inner core in order for the winding process to complete. One interesting finding is that some water molecules remain inside the inner core even at equilibrium and the water molecules also form a spiral roll similar to the graphene sheet (Figure 3.1B). This phenomenon is attributed to the confinement of the inner core and the

finding that the structure of encapsulated water mimics that of the confining graphene structure is similar to the previous study on water structure confined in carbon nanotubes [41].

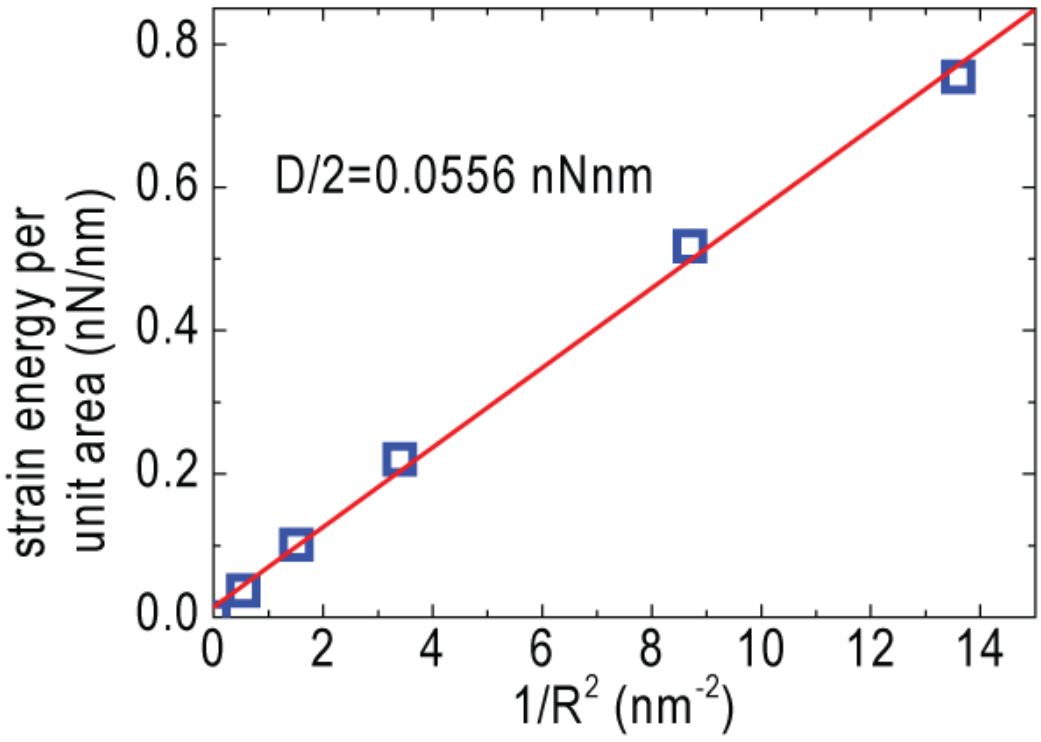


Figure 3.7: The elastic strain energy of a carbon nanotube as a function of its radius. Blue squares are the molecular simulations results and red line is the linear fitting. The slope of the red line is half of the bending modulus. [89]

To aid theoretical calculations on the core size of buckyrolls, we adopt a simple method to determine the bending modulus $D$ of graphene. We calculate the strain energy of a series of carbon nanotubes with different radii. With the force field used in the

present work, the relation between the strain energy per unit area and the tube radius is plotted in Figure 3.7. With the definition of bending energy

$$E_{bending} = \frac{1}{2} D \frac{1}{R^2}, \tag{3.26}$$

we obtain the bending modulus of graphene $D = 0.11\,\text{nN} \cdot \text{nm}$, in excellent agreement with results in the literature [84]. To find the surface energy $\gamma$, we plot the interaction energy versus the size of the buckyroll.

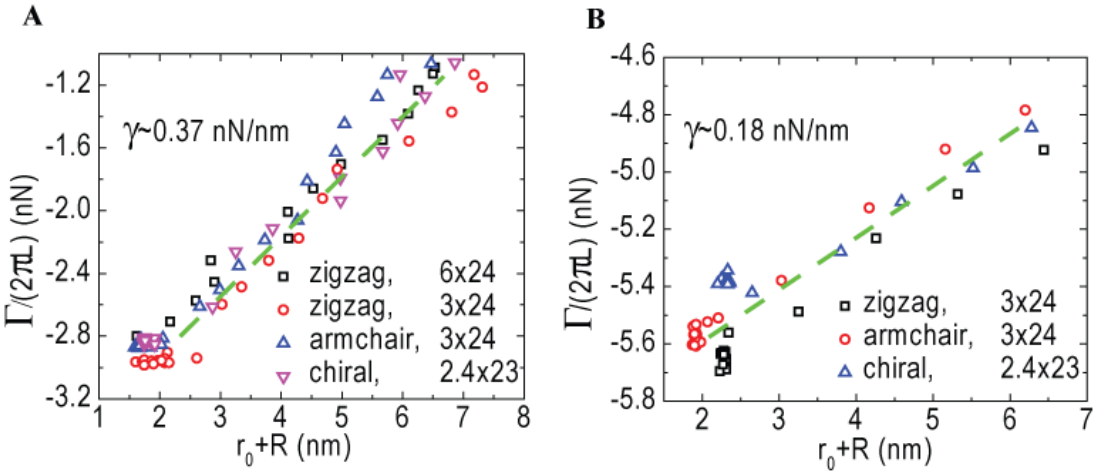


Figure 3.8: (**A**) The interaction energy of CNS in vacuum as a function of their size. Four different kinds of graphene are simulated with results indicating that the surface energy is about 0.37 nN/nm. (**B**) The total interaction energy of CNS in water as a function of their size. The results provide an estimate of the surface energy of graphene in water to be about 0.18 nN/nm. [89]

According to the Eq. (3.9) the increment of interaction energy is a linear function of the increment of $r_0 + R$ with a slope of $2\pi\gamma L$. Therefore, the slope in Figure 3.8 (green line) corresponds to the surface energy. The interaction energy of a buckyroll in water solvent consists of three parts: graphene-graphene, water-water and graphene-water interactions.

The surface energy of graphene in water is reduced to about half its value in vacuum. The simulated equilibrium configurations for different types of CNSs are in excellent agreement with the corresponding theoretical predictions (Table 3.2). The simulations also show a constant contraction speed of CNSs in approaching their equilibrium core size. This phenomenon is consistent with a viscous damping process under a constant driving force,

$$-\frac{\mathrm{d}(W+\Gamma)}{\mathrm{d}r_0} = c(T)\dot{r}_0, \tag{3.16}$$

where $c(T)$ is the damping coefficient, which depends on the temperature of the system.

**Table 3.2: Comparison between predicted (Theo.) and simulated (MD) equilibrium configurations of CNSs of different types.** [89]

| | $r_0$ (nm) | | $R$ (nm) | |
|---|---|---|---|---|
| Theo/MD comparison | MD | Theo. | MD | Theo. |
| Zigzag$^{(v)a}$ | 0.32 | 0.37 | 1.50 | 1.65 |
| Armchair$^{(v)}$ | 0.25 | 0.36 | 1.42 | 1.64 |
| Chiral$^{(v)}$ | 0.23 | 0.33 | 1.56 | 1.61 |
| Zigzag$^{(w)}$ | 0.60 | 0.59 | 1.59 | 1.7 |
| Armchair$^{(w)}$ | 0.61 | 0.56 | 1.60 | 1.68 |
| Chiral$^{(w)}$ | 0.68 | 0.79 | 1.67 | 1.73 |
| Zigzag$^{(v,\,halfvdW)b}$ | 0.67 | 0.63 | 1.76 | 1.73 |

[a](v) means in vacuum and (w) means in water, [b]50% reduction in van der Waals interaction.

We also investigate the influence of pressure on the structure of CNS. Due to the anti-symmetric spiral form of CNS, it is actually difficult to directly apply force to the

inner surface of CNS in MD simulations. As shown in Figure 3.9B, one can mimic an applied internal pressure by inserting a carbon nanotube (CNT) into the core of CNS. By calculating the internal force between the CNT and CNS, the inner pressure of CNS can be determined. Following this method, the pressure levels for different core sizes of CNS are obtained by inserting CNTs with different radii.

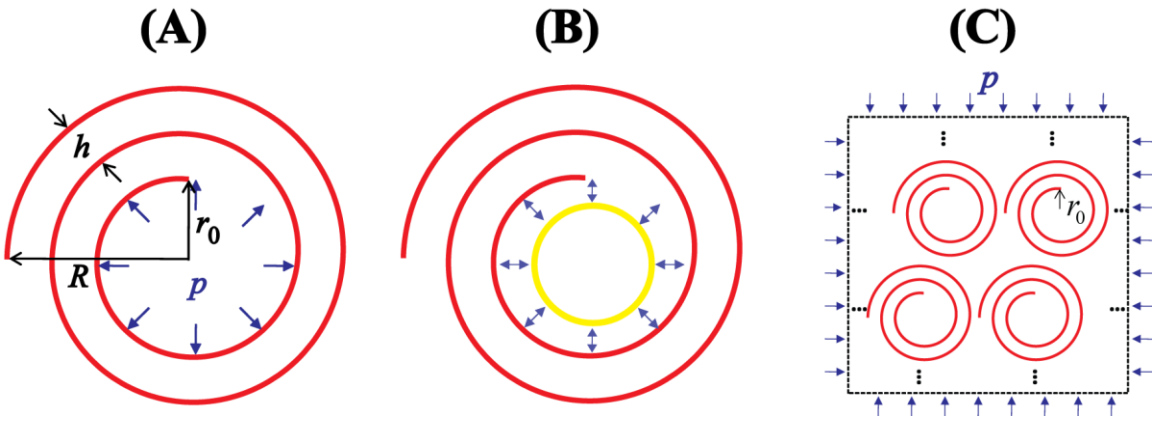


Figure 3.9 (**A**) Schematic illustration of a carbon nanoscroll with inner core radius $r_0$, outer radius $R$ and interlayer spacing $h$. (**B**) An internal pressure is applied by inserting a carbon nanotube inside the core. (**C**) A CNS crystal under biaxial compression. [90]

In studying the contraction of CNS when $p_i - p_e < 0$, we encountered similar difficulty described above. In this case, we constructed a crystal consisting of a closed packed bundle of CNSs (Fig. 3.9C). The CNS crystal is then subjected to biaxial compression, which can be easily realized in MD simulations. Assuming that the pressure near the center of the CNS crystal is uniformly distributed, we calculate the core size of the CNS as a function of the applied pressure on the CNS crystal. The results listed in Figure 3.4 show excellent agreement with the corresponding theoretical predictions.

# *Chapter 4*

# *Tuning surface energy of CNS by external electric field*

In Chapter 3 we studied the equilibrium structure of CNS and found that the equilibrium core size of a CNS is controlled by its surface energy, the bending modulus of graphene, the difference between the pressure inside the core of the CNS and that on its outer surface, the interlayer space and the basal graphene length. Changing each of these parameters would lead to a change in the core size of the CNS. This gives us the hint that we may tune the core size of a CNS by changing any one of these parameters such as the surface energy. In this Chapter, we demonstrate theoretically that the surface energy of a CNS can be reduced by an electric field [96].

## 4.1 Dipole-dipole interaction

Electric field can cause the carbon atoms to be polarized with the following dipole-dipole interactions [97]

$$V(\vec{r}_{12}) = \frac{1}{4\pi\varepsilon_0 |\vec{r}_{12}|^3}\left[ |\vec{p}_1||\vec{p}_2| - \frac{3(\vec{r}_{12}\cdot\vec{p}_1)(\vec{r}_{12}\cdot\vec{p}_2)}{|\vec{r}_{12}|^2}\right], \tag{4.1}$$

where $\vec{r}_{12}$ is the distance between dipole 1 and dipole 2, $\vec{p}_1 = 4\pi\varepsilon_0\alpha_1 E$ is the induced dipole moment, $E$ being the applied electric field, $\varepsilon_0$ the vacuum permittivity and $\alpha_1$ the polarizability of atom 1. It has been previously shown that the polarizability of single-walled carbon nanotubes (SWCNTs) in the axial direction is one order of magnitude higher than that perpendicular to the axis [98]. Therefore, for simplicity, we will only consider the axial polarizability of carbon atoms in the CNS. To calculate the total dipole-dipole interaction energy, we assume there are two dipoles induced by electric field $E$ with dipole moment $\vec{p}_1$ and $\vec{p}_2$ as shown in Figure 4.1.

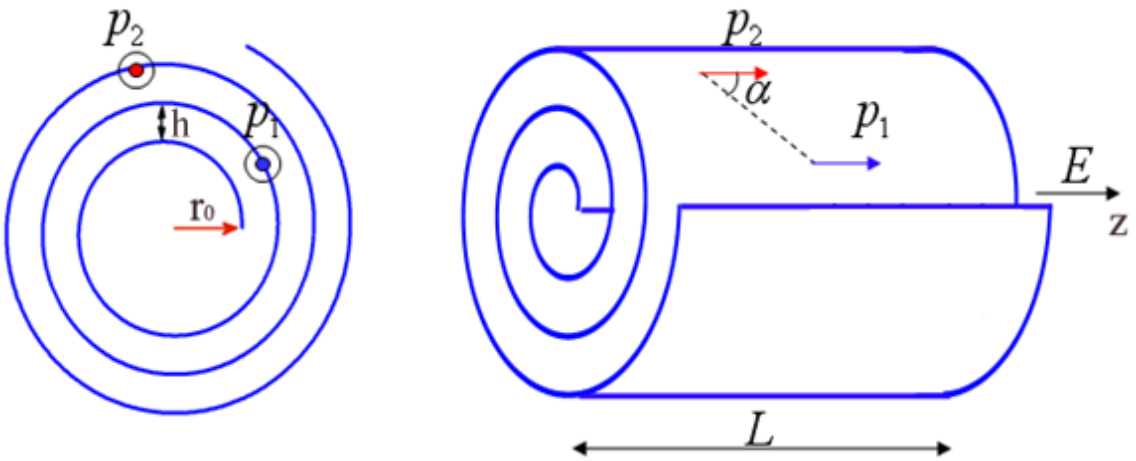


Figure 4.1: Schematic show of two dipoles in CNS induced by electric field applied in axial direction. [96]

The distance of the two dipoles is

$$|\vec{r}_{12}| = \sqrt{\tilde{r}_1^2 + \tilde{r}_2^2 - 2\tilde{r}_1\tilde{r}_2\cos(\theta_1 - \theta_2) + z^2}\,, \tag{4.2}$$

where

$$\begin{aligned}\tilde{r}_1 &= r_0 + \frac{h}{2\pi}\theta_1, \\ \tilde{r}_2 &= r_0 + \frac{h}{2\pi}\theta_2.\end{aligned} \tag{4.3}$$

Suppose each carbon atoms in the CNS is polarized in the electric field, then the total dipole-dipole interaction is

$$\Phi_{dipole} = \sum_{i \neq j} V\left(\vec{r}_{ij}\right), \tag{4.4}$$

which can be calculated as

$$\Phi_{dipole} = \rho_1 \rho_2 \int_0^L dz' \int_0^{2\pi N} \tilde{r}_1 d\theta_1 \int_{\theta_1}^{2\pi N} \tilde{r}_2 d\theta_2 \int_{-z'}^{L-z'} \frac{1}{4\pi\varepsilon_0 \left|\vec{r}_{12}^{\,3}\right|} \left[p_1 p_2 - 3 p_1 p_2 \cos^2\alpha\right] dz, \tag{4.5}$$

where $\rho_1, \rho_2$ are the dipole densities, $N$ is the winding number of the CNS, $\cos\alpha = \dfrac{z}{\left|\vec{r}_{12}\right|}$.

Integrate Eq. (4.5) we obtain

$$\Phi_{dipole} = \frac{\left(4\pi\varepsilon_0 E\right)^2 \rho_1 \rho_2}{2\pi\varepsilon_0} e_{dipole}\left(N, L, r_0, t\right), \tag{4.6}$$

where

$$e_{dipole}\left(N, L, r_0, t\right) = \int_0^{2\pi N} \int_{\theta_1}^{2\pi N} \tilde{r}_1 \tilde{r}_2 \alpha_1 \alpha_2 \left( \frac{1}{\sqrt{\tilde{r}_1^{\,2} + \tilde{r}_2^{\,2} - 2\tilde{r}_1 \tilde{r}_2 \cos\left(\theta_1 - \theta_2\right)}} - \frac{1}{\sqrt{\tilde{r}_1^{\,2} + \tilde{r}_2^{\,2} + L^2 - 2\tilde{r}_1 \tilde{r}_2 \cos\left(\theta_1 - \theta_2\right)}} \right) d\theta_2 d\theta_1. \tag{4.7}$$

For the axial polarizability $\alpha_i$, Langlet et al. [98] have found the relationship between $\alpha_i$ and CNTs radius $r$ as

$$\alpha_i = \left(50.1348 r + 10.8091\right). \tag{4.8}$$

Since the value of $\alpha_i$ obtained in Reference [98] is polarizability (unit in $nm^3$) per unit length of CNTs, we transform it to polarizability per atom in our case by

$$\alpha_i = (50.1348\tilde{r}_i + 10.8091)\frac{\sqrt{3}a}{2\pi\tilde{r}_i}0.5a, \tag{4.9}$$

where *a* is the carbon-carbon bond length. It is worth pointing out that in Reference [98] the authors have considered the local electric field effect, i.e. the electric field induced by dipole, so by adopting the results, we have indeed included the dipole screening effect into our model.

### 4.2 Surface energy reduction

As shown in Chapter 3, the surface energy of the CNS due to dipole-dipole interaction can be extracted as

$$\gamma_{dipole} = \frac{1}{2\pi L}\frac{d\Phi_{dipole}}{d(r_0 + R)} \tag{4.10}$$

where *R* is the outer radius of CNS. The total effective surface energy of the CNS is thus

$$\gamma_{eff} = \gamma_{vdW} + \gamma_{dipole}, \tag{4.11}$$

where $\gamma_{vdW}$ is the surface energy due to van der Waals interaction between carbon atoms. Figure 4.2A shows that the total dipole interaction energy is indeed linearly proportional to the sum of the inner and outer radii of the CNS, with a negative slope proportional to $\gamma_{dipole}$, in perfect consistency with Eq. (4.10). The fact that $\gamma_{dipole}$ is negative indicates that the applied electric field decreases the effective surface energy. Figure 4.2B shows how the applied electric field influences the dipole induced surface energy $\gamma_{dipole}$

normalized by $\gamma_{vdW}$, typically about 0.2 N/m. The result shows that an applied electric field of $E$=0.3 V/nm would decrease the surface energy of the CNS by about 11.5% for graphene length $B = 50$ nm and by 36% for $B = 500$ nm. As the electric field $E$ varies in the range from 0 to 0.5 V/nm, the normalized dipole surface energy changes from 0 to 32.7% for $B = 50$ nm and from 0 to 100% for $B = 500$ nm, indicating that the electric field can significantly alter the surface energy. This is somewhat similar to the effect of dipole-dipole interaction on the surface energy of a thin film [99].

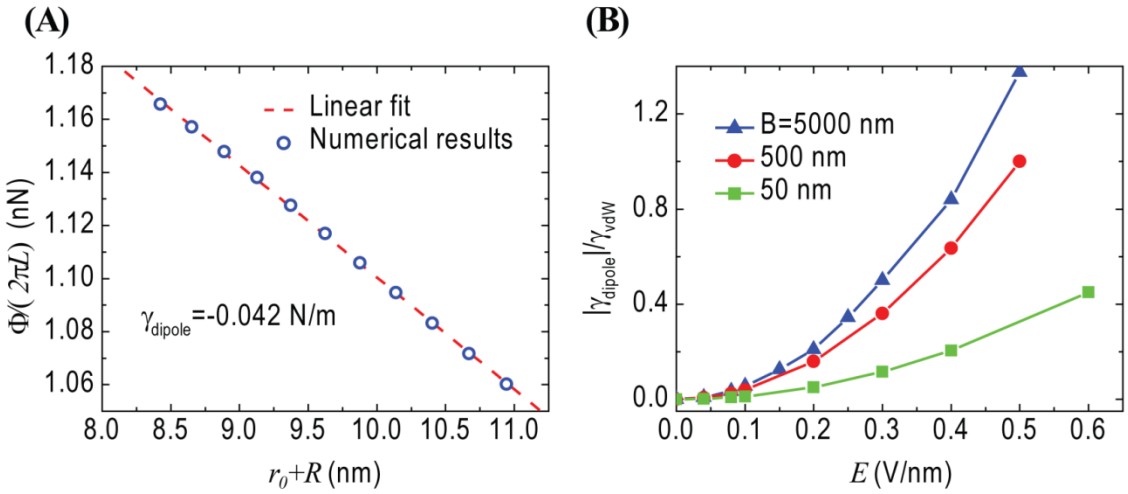


Figure 4.2: (**A**) Dipole-dipole interaction energy of a CNS as a function of the sum of the inner and outer radii. The slope provides an estimate of the dipole induced surface energy of the CNS to be about -0.042 nN/nm with an electric field of $E$=0.1V/nm. (**B**) Dipole induced surface energy (normalized by vdW interaction energy) as a function of the applied electric field for different lengths of graphene. [96]

# *Chapter 5*

# *CNS-based breathing oscillator*

One of the interesting properties of CNS is that the core size of a CNS is not fixed, but can change according to the surface energy and the length of the basal graphene sheet. This flexibility suggests that the inner core of a CNS can be controlled by tuning the effective surface energy via an applied DC/AC electric field. In view of their smooth and ultralow friction spiral layers, it will be interesting to explore potential applications of CNSs as nanoactuators and nanooscillators. Here we perform theoretical study and molecular dynamics (MD) simulations to investigate the "breathing" oscillatory motion of a CNS [100].

## 5.1 Theoretical model

Figure 5.1 illustrates schematically the breathing oscillatory motion of a CNS. Such oscillation can be initiated by suddenly decreasing the interlayer interaction energy to generate a small perturbation in the system. As a consequence of this perturbation, the CNS starts to oscillate with periodic expansion and contraction phases with

circumferential velocity $v_C$ and radial velocity $v_R$. During the expansion phase, the kinetic energy first increases as the potential energy decreases to a minimum value (Figure 5.1B) and then decreases as the potential energy increases to a maximum value (Figure 5.1C). At that point, the contraction phase starts, with potential and kinetic energies going through a similar cycle of growth and decay as in the expansion phase. In this way, the CNS moves back to its initial configuration (Figure 5.1A) and one oscillatory cycle is completed.

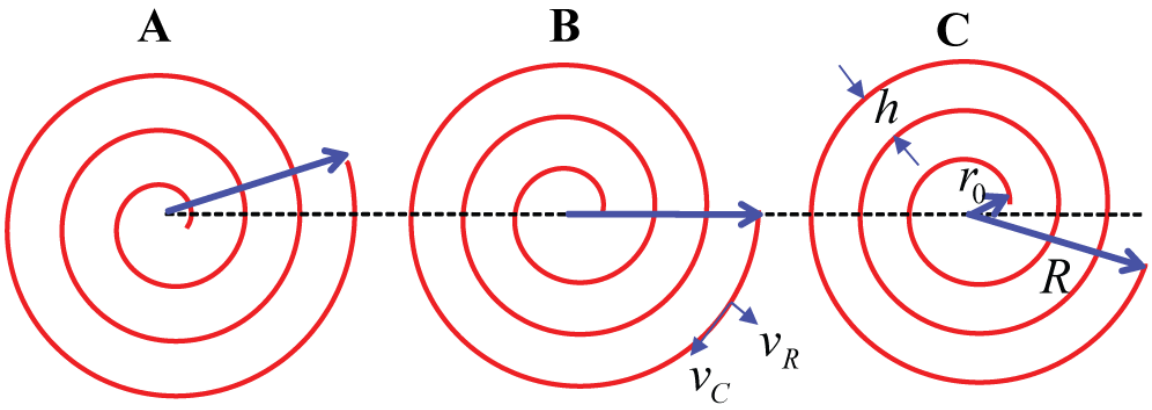


Figure 5.1: The "breathing" oscillatory motion of a carbon nanoscroll. (**A**) The initial configuration. The oscillation is initiated by suddenly decreasing the interlayer interaction energy in the system (via, e.g. an applied electric field), at which the CNS starts to expand. (**B**) The configuration of maximum kinetic energy and minimum potential energy, corresponding to the statically equilibrium state. (**C**) The end of the expansion phase with zero kinetic energy and maximum potential energy, at which the CNS will soon start contracting. [100]

To quantify the above oscillatory motion, it will be convenient to consider the core radius of a CNS as the controlling degree of freedom. It has been previously shown that a stable equilibrium value of $r_0$ can be uniquely determined from the basal graphene length *B*, the interlayer spacing *h*, the interaction energy $\gamma$ and the bending stiffness *D*. Given the existence of such an equilibrium value for $r_0$, the breathing oscillation is

defined as the oscillatory motion associated with slight perturbations of $r_0$ from its equilibrium value. Consider a CNS with inner core radius $r_0$, outer radius $R$ and interlayer spacing $h$. The basal graphene sheet has length $B$ and width $L$. The breathing motion of the CNS can be described using Lagrange's equation

$$\frac{\partial(K-V)}{\partial r_0}-\frac{\mathrm{d}}{\mathrm{d}t}\frac{\partial(K-V)}{\partial \dot{r}_0}-\frac{\partial F}{\partial \dot{r}_0}=0, \tag{5.1}$$

where $K$ denotes the kinetic energy and $V$ the potential energy; $F$ is Rayleigh's dissipation function, $t$ is the time and over-dot represents time derivative. The potential energy of the system has been previously derived. A slightly more general form, taking into account the effect of pressure, is

$$V=\frac{\pi DL}{h}\ln\left(\frac{R}{r_0}\right)+2\pi\gamma L\left(r_0+R\right)-\pi r_0^2 Lp, \tag{5.2}$$

where $R=\sqrt{\frac{Bh}{\pi}+r_0^{\,2}}$ is the outer radius, $D$ is the bending modulus and $\gamma$ is the surface energy per unit area, $p=p_i-p_e$ with $p_e$, $p_i$ being the external and internal pressures. To evaluate the kinetic energy in the system, we first derive the circumferential velocity $v_C=\mathrm{d}s/\mathrm{d}t$ of an infinitesimal arc length $\mathrm{d}s\approx r\mathrm{d}\vartheta$. Noting that the spiral geometry is described by $r=r_0+\frac{h}{2\pi}\vartheta$ and $\mathrm{d}r=\frac{h}{2\pi}\mathrm{d}\vartheta$, we immediately obtain $v_C=\frac{\mathrm{d}s}{\mathrm{d}t}=r\frac{\mathrm{d}\vartheta}{\mathrm{d}t}=\frac{2\pi r}{h}\frac{\mathrm{d}r}{\mathrm{d}t}$. Since the length of the spiral within radius $r$ is a constant $\ell=\frac{\pi}{h}\left(r^2-r_0^{\,2}\right)$, simple differentiation shows $r_0\frac{\mathrm{d}r_0}{\mathrm{d}t}=r\frac{\mathrm{d}r}{\mathrm{d}t}$ and consequently $v_C=\frac{2\pi r_0}{h}\frac{\mathrm{d}r_0}{\mathrm{d}t}$, indicating that the circumferential velocity is constant along the entire

spiral. On the other hand, the radial velocity of the arc length $\mathrm{d}s \approx r\mathrm{d}\vartheta$ is given by $v_R(r) = \frac{\mathrm{d}r}{\mathrm{d}t} = \frac{r_0}{r}\frac{\mathrm{d}r_0}{\mathrm{d}t}$. Since $v_C / v_R = 2\pi r / h >> 1$, we can assume $v = \sqrt{{v_C}^2 + {v_R}^2} \approx v_C$. Accordingly, the kinetic energy in the system could be evaluated as $K = \frac{1}{2}Mv_C^2 = \frac{2\pi^2 M r_0^2 \dot{r}_0^2}{h^2}$, where $M$ is the total mass of the CNS. In Chapter 3 the atomistic simulations also suggest there exists a viscous damping force with $\frac{\partial F}{\partial \dot{r}_0} = C(T)\dot{r}_0$, where $C(T)$ is a damping coefficient which depends on the temperature $T$ of the system. Combining all terms together, the Lagrange's equation of motion is derived as

$$\frac{\pi DL}{h}\left(1 - \frac{r_0^2}{Bh/\pi + {r_0}^2}\right)\frac{1}{r_0} - 2\pi\gamma L\left(1 + \frac{r_0}{\sqrt{Bh/\pi + {r_0}^2}}\right) + 2\pi r_0 Lp - \frac{4\pi^2 M}{h^2}\left(r_0\dot{r}_0^2 + r_0^2\ddot{r}_0\right) - C\dot{r}_0 = 0 \tag{5.3}$$

which can be used to study dynamic expansion/contraction of a CNS. In particular, for the breathing oscillatory motion around an equilibrium configuration, we would search for a solution in the form $r_0(t) = r_{0e} + \varepsilon(t)$, where $\varepsilon(t)$ is a small perturbation and $r_{0e}$ is a static equilibrium core size satisfying the relation

$$\frac{2\gamma h}{D} = \frac{1}{r_{0e}} - \frac{1}{R} + \frac{2hp}{D(1/r_{0e} + 1/R)}, \tag{5.4}$$

which can be easily derived from the static energy balance $\frac{\partial V}{\partial r_0}(r_0 = r_{0e}) = 0$. A similar result in the absence of the pressure term has been shown previously. For the small perturbation $\varepsilon(t)$, we retain the first order terms $\varepsilon, \dot{\varepsilon}, \ddot{\varepsilon}$ only in the Lagrange's equation

and obtain a governing equation for the breathing oscillation as $\ddot{\varepsilon}+2\varsigma\omega_0\dot{\varepsilon}+\omega_0^2\varepsilon=0$, where

$$\omega_0=\sqrt{\frac{\pi D}{4\rho B^3h^2}\left[\frac{\alpha^3(\alpha+3)}{(1+\alpha)^2}+2\frac{\gamma}{D}\sqrt{\frac{Bh^3}{\pi}}\frac{\alpha^2\sqrt{\alpha}}{(1+\alpha)^{3/2}}-2\frac{Bh^2p}{\pi D}\alpha\right]} \tag{5.5}$$

is identified as the oscillation frequency and

$$\varsigma=\frac{C\alpha}{8\pi\rho LB^2\omega_0} \tag{5.6}$$

is the effective damping factor. Here, $\rho$ is the material density and $\alpha=\frac{Bh}{\pi r_{0e}^2}$ is the ratio between the cross-sectional area of the CNS and that inside the core. Eq, (5.5) suggests that the oscillatory frequency $\omega_0$ is related to the bending modulus *D*, the surface energy $\gamma$, the length of graphene *B*, the interlayer spacing *h* and the relative pressure *p*. The effective damping $\varsigma$ is related to the frequency $\omega_0$, the CNS width *L* as well as the damping coefficient *C* (Eq. (5.6)). Figure 5.2c plots the relation between the oscillatory frequency and surface energy by taking the rest of the parameters as *p*=0, *B*=24 nm, *D*=0.11 nNnm, $\rho=2267\text{kg}/\text{m}^3$ and *h*=0.34 nm. The result indicates that the oscillatory frequency increases with surface energy. On the other hand, if the surface energy is fixed at $\gamma=0.1\,\text{nN}/\text{nm}$, Figure 5.2d shows the oscillatory frequency as a function of the graphene length *B*, indicating that the frequency can be increased by shortening the graphene length.

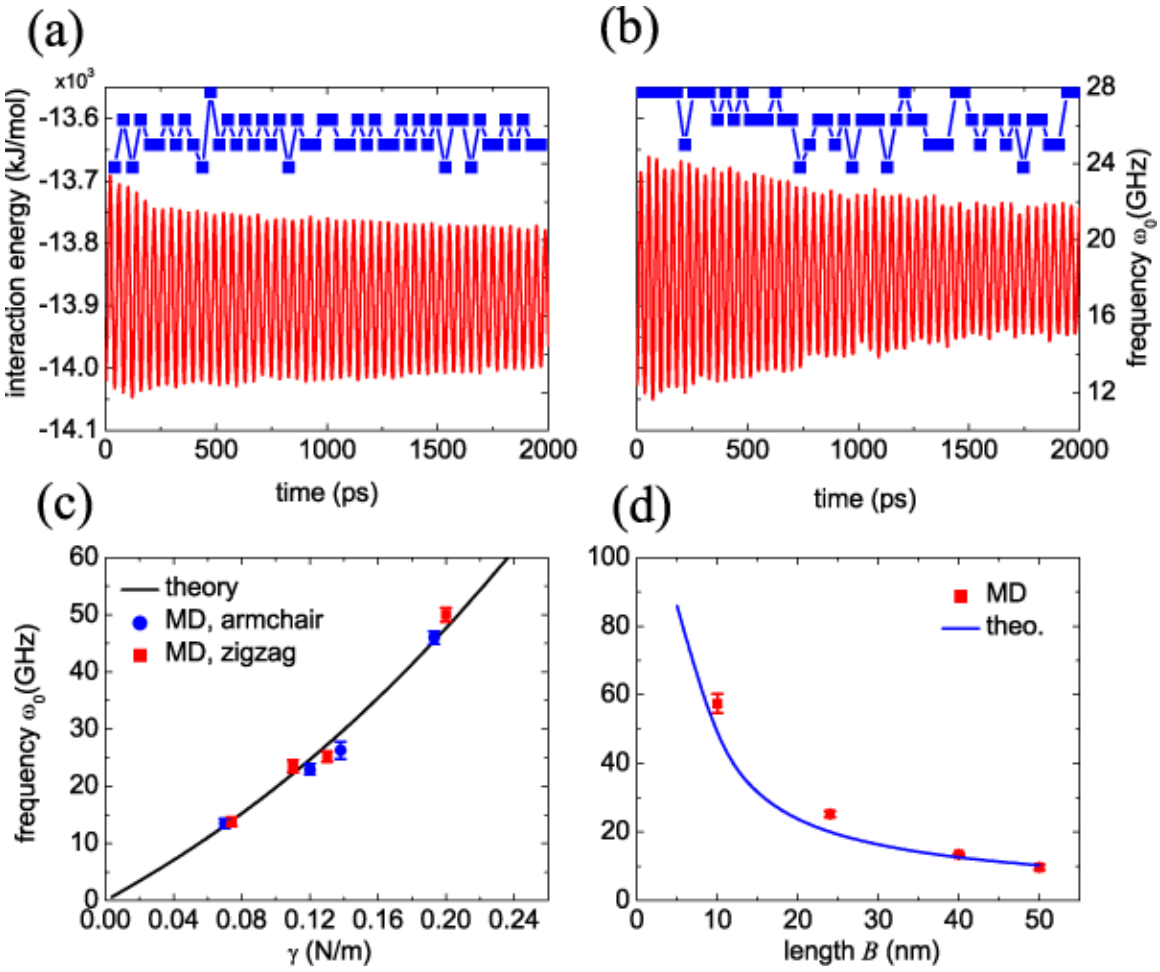


Figure 5.2: Gigahertz oscillatory motion of carbon nanoscrolls (CNSs). Molecular dynamics simulation results for the evolution of interlayer interaction energy (red line) and fundamental frequency (blue square) as functions of time for (**a**) zigzag and (**b**) armchair CNSs. The length $B$ of the basal graphene sheet is taken to be 24 nm and tuning parameter $\lambda$ is 0.8. **(c)** The fundamental frequency as a function of the surface energy of CNSs. Solid line is the theoretical prediction, and red squares and blue circles are the simulation results for zigzag and armchair CNSs, respectively. **(d)** The fundamental frequency as a function of the grapehene length. Blue line is the theoretical prediction, and red squares are the simulation results for zigzag CNSs. [100]

## 5.2 Fundamental frequency

To verify our theoretical model, we have conducted MD simulations with the bonded interactions among carbon atoms on CNSs described by a Morse bond, a harmonic cosine of the bending angle and a twofold torsion potential [92]. The resulting bending modulus

(0.11 nNnm) agrees well with that calculated using Brenner's potential [84]. The non-bonded vdW interactions are described by the Lennard-Jones (LJ) potential

$$U(r_{ij},\lambda)=4\lambda\varepsilon_{CC}\left[\left(\frac{\sigma_{CC}}{r_{ij}}\right)^{12}-\left(\frac{\sigma_{CC}}{r_{ij}}\right)^{6}\right], \tag{5.7}$$

where $\varepsilon_{CC}=0.3601$kJ/mol, $\sigma_{CC}=0.34$nm and $\lambda$ is a tuning parameter ($0<\lambda\le 1$) that can be used to tune the core size of a CNS. In MD simulations of oscillation around a equilibrium configuration characterized by a specific $\lambda$, we first set up an initial equilibrium structure at a slightly perturbed state $\lambda+\delta\lambda$, where $\delta\lambda$ is typically taken to be $0.2$. The oscillation of the CNS is initiated by setting the tuning parameter back to the reference value $\lambda$. Experimentally, the small perturbation $\delta\lambda$ can be imposed by applying an electric field to reduce the effective surface energy of the CNS. The simulations are conducted using Gromacs4 [91] with microcanonical NVE ensemble, initial temperature 10 K and time step 1 fs. The total energy variation remains within 0.003% in all simulations. To investigate the temperature effect on the dissipation of CNS oscillation, we have also conducted MD simulations under different initial temperatures $T_0$.

Our simulation results confirm the gigahertz breathing oscillatory motion of CNSs. For a zigzag CNS rolled up from a basal graphene sheet of length *B*=24 nm, the mean oscillatory frequency is about 25.2 GHz when $\lambda=0.8$ (Figs. 5.2a, c). Our theoretical result in Eq. (5.5) shows that the oscillating frequency depends on the surface energy which is controlled by the vdW interaction parameter $\lambda$ in our simulations. We found that the frequency increases from 25.2 to 50 GHz as $\lambda$ is raised from 0.8 to 1.0, and decreases from 25.2 to 22.7 GHz as $\lambda$ is reduced from 0.8 to 0.6. The results of an

armchair CNS with the same length $B$=24 nm show similar behaviors as that of the zigzag CNS (Figs. 5.2b, c), suggesting that the effect of chirality on oscillating frequency is relatively minor. To investigate the effect of the graphene length $B$ on the oscillating frequency, three zigzag CNSs with $B$=10, 40, 50 nm are simulated with $\lambda = 0.8$. It is found that the shorter the graphene length, the higher the oscillating frequency (Fig. 5.2d). Figures 5.2c and 5.2d show that the MD results are in good agreement with the corresponding predictions from our theoretical model.

Note that our theoretical model has assumed that the interlayer spacing remains constant and the basal graphene layer is inextensible during the breathing oscillation. These assumptions are fully supported by our MD simulations which indicate that the breathing motion is indeed dominated by relative sliding of the scroll layers, rather than by any significant changes in interlayer spacing or stretching of the graphene layer.

### 5.3 Dissipation

To investigate energy dissipation associated with the CNS oscillation, we plot the amplitude of vdW interaction energy in Figure 5.3a as a function of simulation time for a CNS with $B$=24 nm, $\lambda = 0.8$ and initial temperature 10 K. It is estimated that energy is dissipated at a rate of 30 kJ/mol/ns. Similar energy dissipation has been found in the co-axial oscillation of a carbon bitube [101-104] or oscillation of a graphene-graphene bi-layer [105]. Unlike previous findings [101-103] that the oscillating frequency of a carbon bitube tends to increase with energy dissipation in the system, we do not find any apparent correlation between energy dissipation and frequency, which is consistent with our theoretical model.

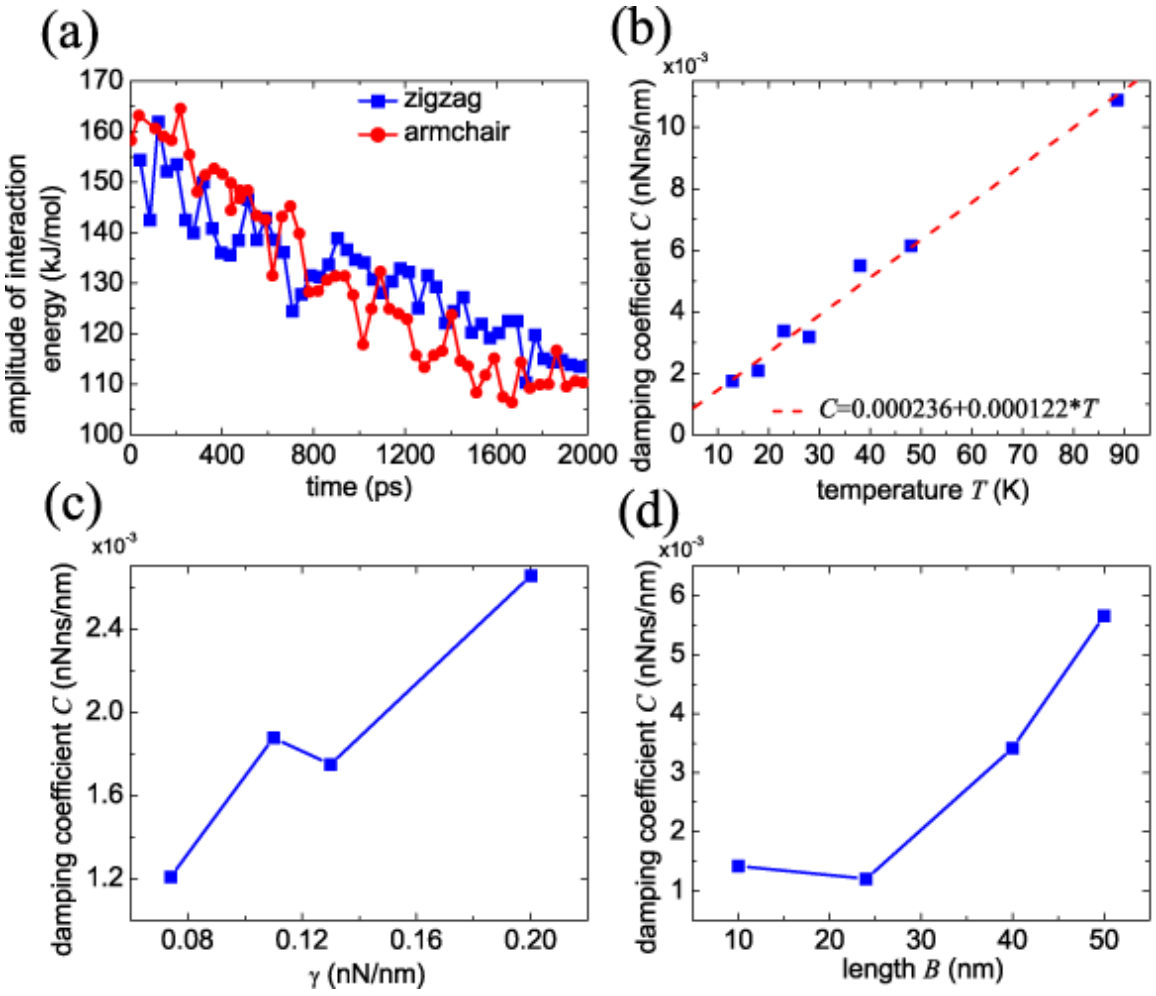


Figure 5.3: Energy dissipation during gigahertz CNS oscillation. **(a)** Simulated evolution of oscillating amplitude of interlayer interaction energy as a function of time for a zigzag (blue squares) and an armchair (red circles) CNSs with *B*=24 nm and tuning parameter $\lambda$ =0.8. **(b)** Damping coefficient as a function of simulation temperature. A linear correlation (red dash line) between damping coefficient and temperature is identified as $C = 0.000236 + 0.000122T$ . In all simulations, the length of CNSs *B* is taken to be 24 nm and tuning parameter $\lambda$ is 0.8. **(c)** The damping coefficient as a function of surface energy $\gamma$ . **(d)** The damping coefficient as a function of graphene length *B*. [100]

Our simulations show that the energy dissipation rate of CNS oscillation depends on the total interlayer area as well as the edge interactions of the basal graphene sheet. A thorough investigation of these geometrical effects on the energy dissipation of CNS

oscillator is beyond the scope of the present work. Here we focus on some environmental factors which might be useful in controlling energy dissipation in a given CNS system. First, we explore the effect of the initial temperature by conducting a series of MD simulations with fixed *B*=24 nm and $\lambda = 0.8$, while allowing the initial temperatures $T_0$ to vary from 10 K to 160 K. The simulations show similar oscillating frequency (~26 GHz) but different energy dissipation rates. We estimate the damping ratio $\varsigma$ from our MD simulations according to $\varsigma = 1\Big/\sqrt{1+\left(\frac{2\pi}{\delta}\right)^2}$, where $\delta = \frac{1}{n}\ln\frac{x_0}{x_n}$ is the logarithmic decrement, $x_0$ and $x_n$ being two amplitude peaks separated by *n* periods. According to our theoretical prediction $\varsigma = \frac{C\alpha}{8\pi\rho LB^2\omega_0}$, the estimated damping coefficients *C* at different temperatures are listed in Figure 5.3b. Interestingly, we find that the damping coefficient increases linearly with the temperature as $C = 0.000236 + 0.000122T$. To investigate other factors that may influence the damping coefficient, we have further investigated two simulation systems: One with the basal graphene length fixed at *B*=24 nm while the surface energy is taken to be $\lambda = 1.0, 0.8, 0.6, 0.4$; another with the surface energy fixed at $\lambda = 0.8$ while the basal graphene length is taken to be *B*=10, 24, 40, 50 nm. All simulations are conducted at an initial temperature of 10 K. The results indicate that the damping coefficient increases with the surface energy $\gamma$ (Figure 5.3c) as well as the graphene length *B* (Figure 5.3d). The plateau in Figure 5.3d for *B*<20 nm can be attributed to the failure of our theoretical model in this regime, where $v_C/v_R = 2\pi r/h$ is not much greater than one and the radial velocity $v_R$ is no longer negligible. These

findings suggest that lower temperature, shorter graphene length and surface energy lead to lower dissipation rates.

### 5.4 Resonant frequency

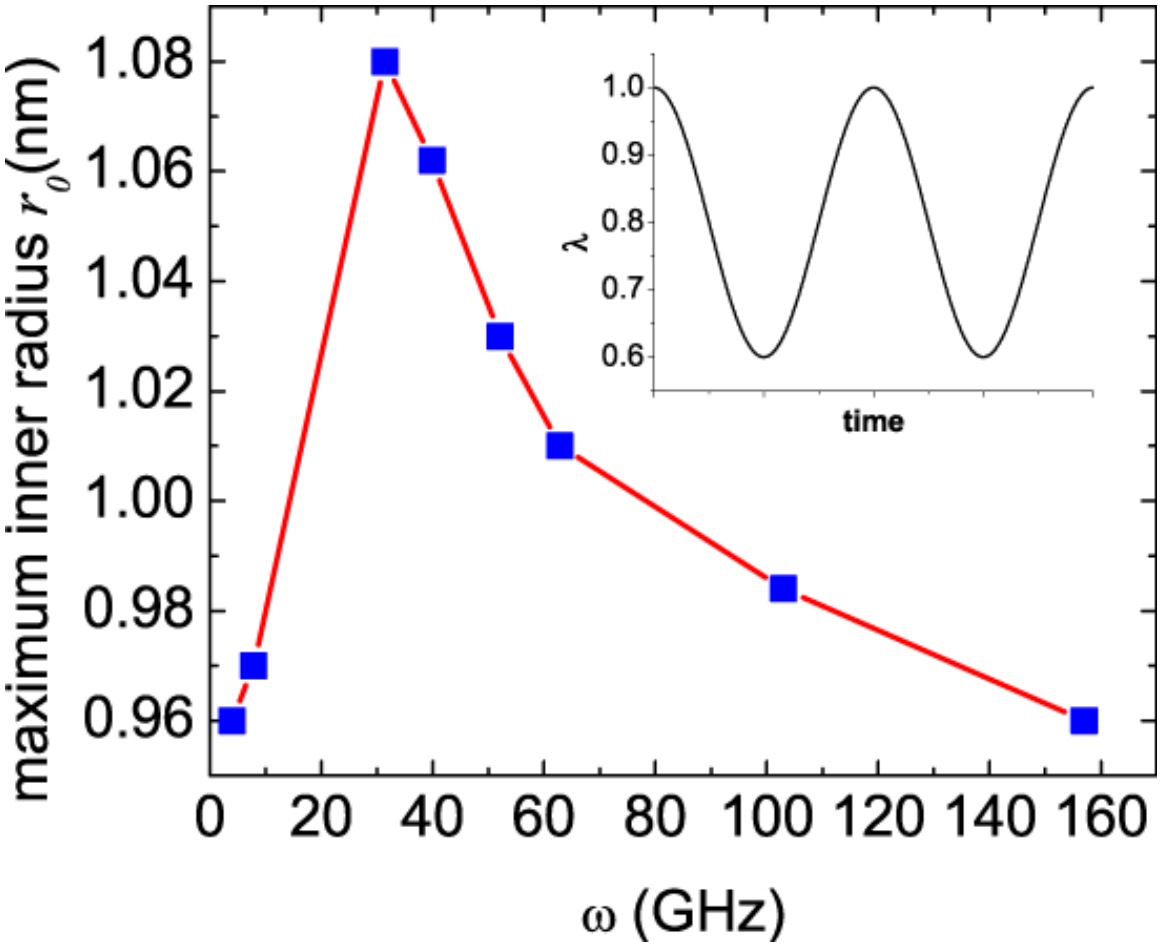


Figure 5.4: The maximum core radius of a CNS subjected to an oscillating interlayer interaction energy with frequency $\omega$ (inset), simulating resonance under an applied AC electric field. [100]

An interesting question is how a CNS responds to an applied oscillating field near the resonant frequency of the system. To mimic an applied AC electric field, we let the energy tuning parameter vary according to

$$\lambda(t) = \frac{1-\beta}{2}\left[1+\cos(\omega t)\right] + \beta, \tag{5.8}$$

where $\omega$ is the frequency of the applied field and $\beta$ is a parameter depending on the field strength. The effect of an applied electric field on surface energy has been previously investigated in Chapter 4. We consider a simulation system with *B*=24 nm and set $\beta = 0.6$ so that $\lambda$ varies from 0.6 to 1 with a mean value of 0.8 (see the inset of Figure 5.4). Figure 5.4 shows that the maximum inner core radius varies with the applied frequency $\omega$, with a peak value at $\omega \sim 30\,\text{GHz}$, which is quite close to the fundamental frequency about 25 GHz at $\lambda = 0.8$ for the selected CNS. The discrepancy between the observed resonance frequency and the fundamental frequency may be partly attributed to damping ($\varsigma \sim 10^{-3}$) in our simulation system. Note that the core of the CNS is significantly widened at the resonant frequency. This phenomenon may be particularly useful in designing controllable CNS-based drug and gene loading/release systems.

# *Chapter 6*

# *CNS-based translational nanoactuator*

An actuator is a mechanical device designed to move or control a system by converting electric or other forms of energy into mechanical motion. The development of nanotechnology has brought the concept of actuation to a new stage in which synthesized nanoactuators are broadly applied in nanoelectromechanical systems (NEMS) such as nanomotors, nanorobots and nanosensors [39, 40, 106, 107]. The materials considered for these applications are typically carbon nanotubes or nanobelts. Here we propose a class of novel, controllable nanoactuators based on substrate-supported carbon nanoscrolls (CNS) whose motion can be controlled over a broad size range by an applied DC/AC electric field [108].

## 6.1 Theoretical model

It has been shown that the equilibrium core size of a CNS depends on the length and bending modulus of the basal graphene sheet, as well as the interlayer spacing and interaction energy in the CNS structure. Upon externally applied stimuli which typically

decrease the interaction energy, the CNS would adjust to a new equilibrium state with an expanded inner core. In this way, the core size of a CNS can be controlled by tuning the effective surface energy via an applied DC/AC electric field. The previous studies, however, have been focused on systems with suspended CNSs. Inspired by recent experiments on the fabrication of CNSs on solid substrates [25], here we develop a theory of linear actuator based on substrate-supported CNSs and conduct molecular dynamics simulations to demonstrate the principle of such linear actuation through controlled forward and backward rolling of a CNS on a graphite substrate as its surface energy is tuned by an applied DC/AC electric field.

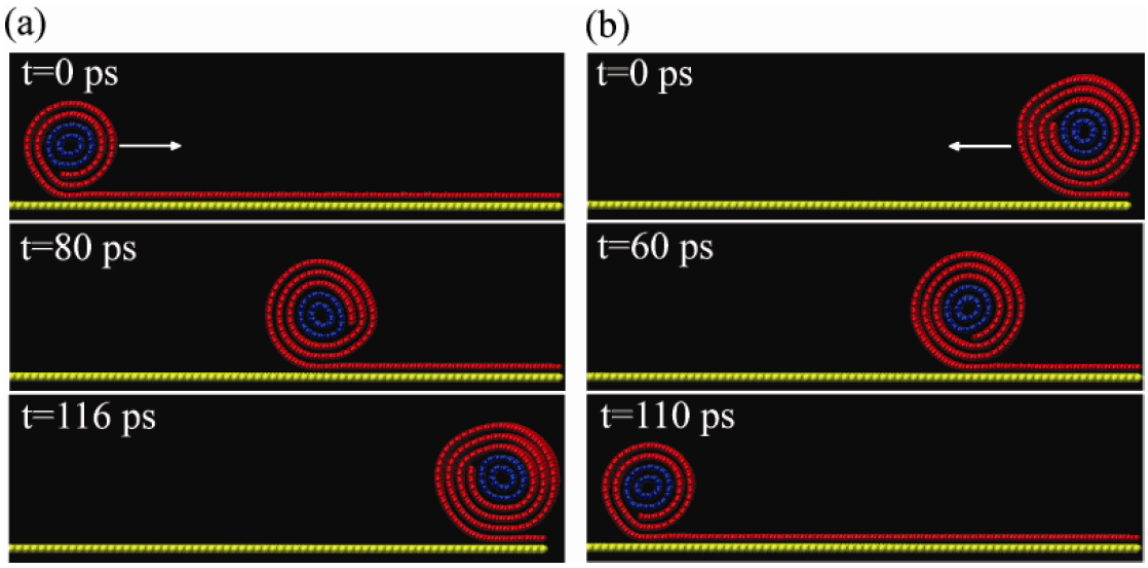


Figure 6.1: Snapshots of molecular dynamics simulation of carbon nanoscrolls (CNS) (red color) rolling along the graphite substrate (yellow color). The tuning parameter for CNS-CNS interaction is (**a**) $\lambda_{CC} = 1.0$ and (**b**) $\lambda_{CC} = 0.6$ . The tuning parameter for CNS-Graphite interaction is $\lambda_{CS} = 0.8$ in both systems. To constrain the core size of CNS, multi-walled carbon nanotubes (MWCNTs) are inserted inside the core of CNS (blue color). [108]

Figure 6.1 displays some snapshots from molecular dynamics simulations of a linear nanoactuator based on a CNS supported on a Graphite substrate. A multiwalled

carbon nanotube (MWCNT) has been added to the system to aid the initial formation of the CNS as well as to constrain its inner core size during linear motion. With fixed CNS-substrate interaction, the CNS would roll rightward if the CNS-CNS interaction is strong enough to overcome the CNS-Graphite interaction as well as the contribution from elastic bending of CNS (Figure 6.1a). On the other hand, it would roll leftward if the CNS-CNS interaction is reduced by an applied electric field (Figure 6.1b). In this manner, the CNS is controlled to move rightward or leftward by tuning the CNS-CNS interaction energy.

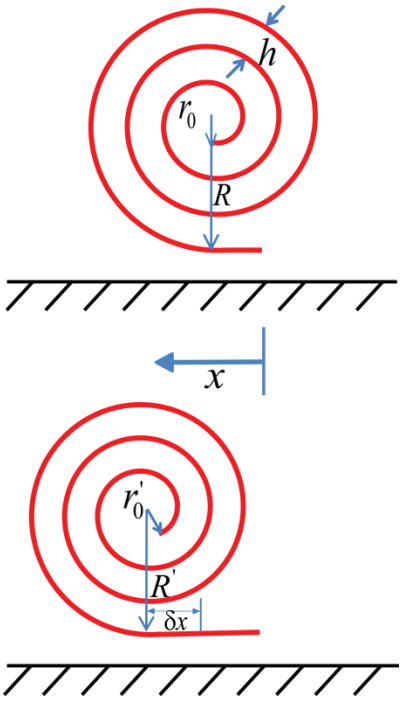


Figure 6.2: Schematic illustration of CNS on substrate. As the CNS rolls forward an infinitesimal displacement $\delta x$ , the inner and outer radii of CNS change to $r_0^{'}$ and $R^{'}$ from $r_0$ and $R$ , respectively. [108]

To develop a theory for the CNS linear actuator shown in Figure 6.1, we consider a graphene sheet of length $B$ and width $L$ rolled up into a carbon nanoscroll on a rigid substrate (Fig. 6.2). The nanoscroll has a fixed inner core radius $r_0$, outer radius $R$ and

interlayer spacing $h$, and can be rolled out into a flat graphene sheet along the substrate. In this process, the nanoscroll part of the structure can be described by a radial function as $r = r_0 + \frac{h}{2\pi}\vartheta$, where $B$, $h$, $R$ and $r_0$ are related as $\pi\left(R^2 - r_0^2\right) = (B - x)h$, where $x$ denotes the length of the rolled out part of the graphene sheet on substrate. The elastic energy per unit area of CNS is taken to be

$$\frac{\mathrm{d}W(r)}{\mathrm{d}A} = \frac{D}{2}\frac{1}{r^2}. \tag{6.1}$$

where $D$ is the bending modulus. Noting that $\mathrm{d}A \approx L\mathrm{d}\vartheta$, the total elastic energy in the CNS can be obtained by integrating Eq. (6.1) as $W = \frac{\pi DL}{h}\ln\left(\frac{R}{r_0}\right)$. Our simulation results, to be discussed in the next section, will show that a key to realizing the linear motion of CNS is to fix its inner core radius $r_0$ by inserting a carbon nanotube. Therefore, in the theory, we shall keep $r_0$ constant during the forward and backward rolling motion. As the CNS is unrolled by an infinitesimal distance $\delta x$, the outer radius $R$ of the CNS would decrease by $2\pi R\delta R = -h\delta x$. The change in strain energy is then $\delta W = \frac{\pi DL}{h}\frac{\delta R}{R} = -\frac{DL}{2\left(\frac{(B-x)h}{\pi} + r_0^2\right)}\delta x$. At the same time, the total surface energy of the CNS is altered by $\delta\Gamma = L(\gamma_{CC} - \gamma_{CS})\delta x$, where $\gamma_{CC}$ is the interlayer interaction energy of CNS and $\gamma_{CS}$ is the interaction energy per unit area between the rolled out graphene sheet and substrate. Adding the contributions from elastic energy and surface energy, the change in total potential energy associated with an unrolling displacement $\delta x$ is

$$\frac{\delta V}{\delta x} = \frac{\delta\Gamma}{\delta x} + \frac{\delta W}{\delta x}. \tag{6.2}$$

The energy release rate per unit area, corresponding to the energetic force associated with unrolling, is therefore

$$\frac{f}{L} = -\frac{1}{L}\frac{\delta V}{\delta x} = \gamma_{CS} - \gamma_{CC} + \frac{D}{2\left(\frac{(B-x)h}{\pi} + r_0^2\right)}. \tag{6.3}$$

The above equation shows that the net driving force can be either positive or negative, depending on the relative magnitudes of the self-affinity ($\gamma_{CC}$) of the graphene sheet and its affinity with the substrate ($\gamma_{CS}$). Assuming the system is mainly dominated by surface energy (for reasons to be discussed shortly), the CNS would roll forward if $\gamma_{CS} - \gamma_{CC} > 0$, and backward if $\gamma_{CS} - \gamma_{CC} < 0$. Therefore, the translational motions of CNS can be fully controlled by adjusting the value of $\gamma_{CS} - \gamma_{CC}$. The equation of motion for such translational motion can be derived from Lagrange's equation

$$\frac{\partial(K-V)}{\partial x} - \frac{d}{dt}\left(\frac{\partial(K-V)}{\partial \dot{x}}\right) = 0, \tag{6.4}$$

where $K$ denotes the kinetic energy and $V$ the potential energy of the system; $t$ is the time and over-dot the time derivative. The potential energy can be derived by integrating Eq. (6.2) as

$$V = \frac{\pi DL}{h}\ln\left(\frac{R}{r_0}\right) + L(\gamma_{CC} - \gamma_{CS})x + V_0, \tag{6.5}$$

where $V_0$ is a reference value independent of $x$ and $\dot{x}$. To evaluate the kinetic energy in the system, we consider a rolling CNS as a rolling cylinder on a substrate with kinetic energy

$$K = \frac{1}{2}M\dot{x}^2 + \frac{1}{2}J_A\omega_A^2, \tag{6.6}$$

where $J_A = \frac{1}{2}MR^2$ is the moment of inertia of the cylinder, $\omega_A = \frac{\dot{x}}{R}$ is the angular velocity and $M = \rho L(B-x) + M_0$ is the mass of the rolling CNS, $\rho$ being the mass density of graphene and $M_0$ the mass of the constricting tube in the core. Inserting Eqs. (6.5) and (6.6) into Eq. (6.4) yields

$$\frac{3}{2}\left[\rho L(B-x)+M_0\right]\ddot{x} - \frac{3}{4}\rho L\dot{x}^2 + L\left[\gamma_{CC} - \gamma_{CS} - \frac{D}{2\left(\frac{(B-x)h}{\pi} + r_0^2\right)}\right] = 0. \qquad (6.7)$$

Given initial conditions and properties of the CNS and substrate, Eq. (6.7) can be integrated to predict the translational motion of the CNS.

### 6.2 Molecular dynamics simulation verification

To verify our theoretical model, we have conducted a series of MD simulations with bonded interaction among carbon atoms described by a Morse bond, a harmonic cosine of the bending angle and a twofold torsion potential [92]. The non-bonded vdW interactions are described by the Lennard-Jones (LJ) potential

$$U(r_{ij}, \lambda) = 4\lambda\varepsilon\left[\left(\frac{\sigma}{r_{ij}}\right)^{12} - \left(\frac{\sigma}{r_{ij}}\right)^{6}\right], \qquad (6.8)$$

where $\varepsilon = 0.3601\,\text{kJ/mol}$, $\sigma = 0.34\,\text{nm}$ and $\lambda$ is a tuning parameter ($0 < \lambda \le 1$) used to tune the strengths of CNS-CNS, CNS-CNT and CNS-substrate interactions. For all simulations, the CNS-substrate and CNS-CNT interactions are fixed by setting the tuning parameter at 0.8 and 1.0, respectively. The CNS-CNS interactions, however, are tuned to different levels by setting the tuning parameter at $\lambda_{CC} = 0.5, 0.6, 0.7$ to unroll the CNS

leftward, and $\lambda_{CC} = 0.9, 1.0$ to roll it rightward. Two layers of graphene with dimension $31 \times 3.8\,\text{nm}^2$ are used in the system: The bottom layer is fixed to model the graphite substrate and the top one is rolled up into a CNS with right end fixed. A MWCNT consisting of (5,5) and (10,10) SWCNTs is inserted into the core of CNS. Two initial configurations of partially rolled up CNSs are selected in the simulation: One with $x = 15.2\,\text{nm}$ (Fig. 6.1a) and another with $x = 1.1\,\text{nm}$ (Fig. 6.1b). The initial velocities are set to be zero. The simulations are conducted using Gromacs4 [91] with microcanonical NVE ensemble, with initial temperature 10 K and time step 2 fs.

To find the surface energy $\gamma$ corresponding to different values of the tuning parameter $\lambda$, we plot the CNS-CNS interaction energies determined from MD simulations versus the rolling displacement of CNS. According to Equation $\delta\Gamma = L(\gamma_{CC} - \gamma_{CS})\delta x$, the increment of CNS-CNS interaction energy $\delta\Gamma_{CC}$ is a linear function of the rolling displacement $\delta x$ with a slope of $\gamma_{CC}L$. Therefore, the slope in Figure 6.3a (dashed lines) corresponds to the surface energy. The CNS-substrate interaction energy is determined in a similar way, as shown in Figure 6.3b for $\lambda_{CS} = 0.8$. It is shown in Figure 6.3c that $\gamma_{CC}$ and $\lambda_{CC}$ obeys a linear relationship, which is consistent with Eq. (6.8), where the interaction energy is linearly dependent on $\lambda$.

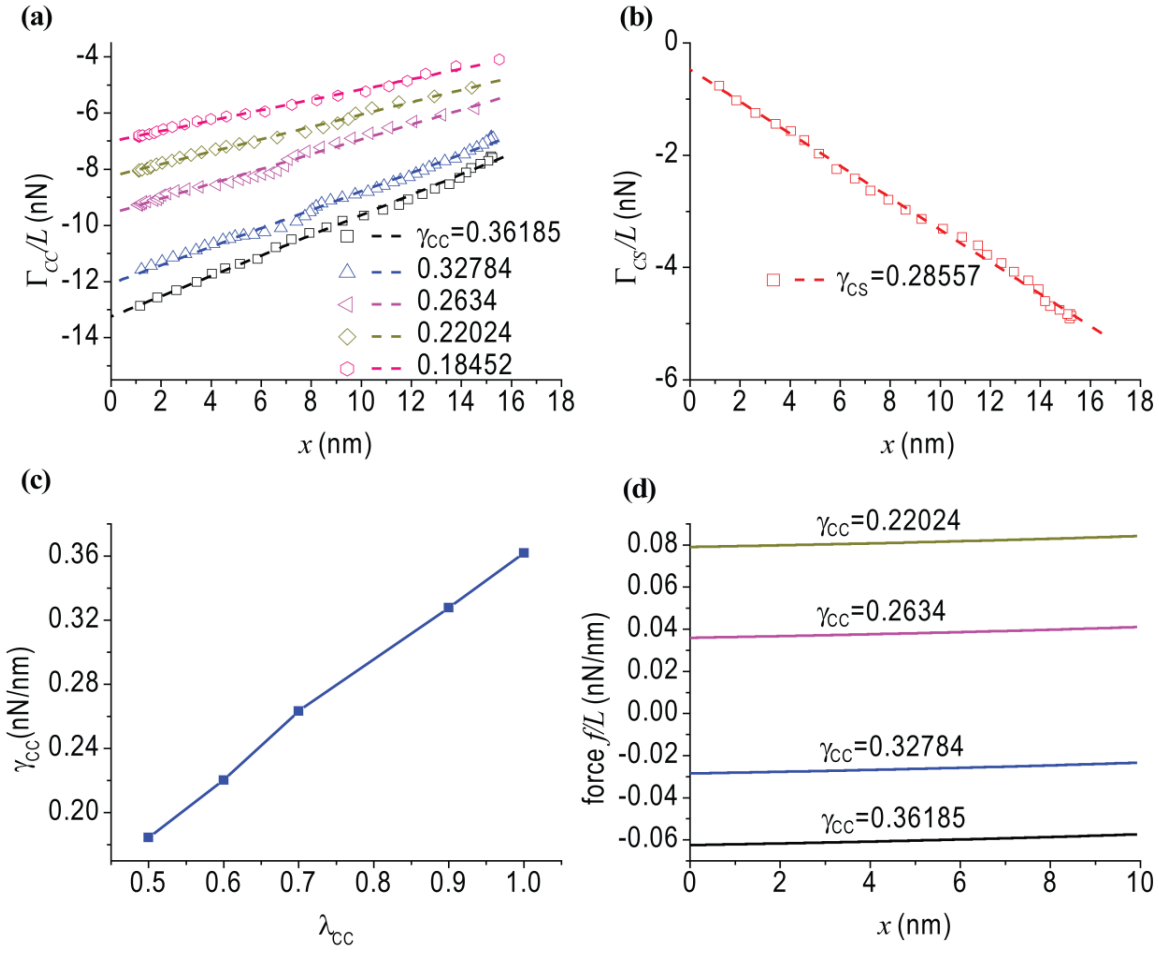


Figure 6.3: **(a)** The interaction energy of CNS-CNS as a function of the position of CNS. Five simulation results are shown with tuning parameters $\lambda_{CC}$ at 1.0, 0.9, 0.7, 0.6 and 0.5, corresponding to different CNS surface energy 0.36185, 0.32784, 0.2634, 0.22024 and 0.18452 nN/nm, respectively. **(b)** The interaction energy of CNS-Graphite as a function of the position of CNS with $\lambda_{CS} = 0.8$, corresponding to the CNS-Graphite surface energy 0.28557 nN/nm. **(c)** The surface energy of CNS $\gamma_{CC}$ as a function of tuning parameter $\lambda_{CC}$. **(d)** The total force per unit length applied on CNS as a function of position of CNS for different levels of interaction. [108]

With the surface energy $\gamma$ obtained, we calculate the energy release rate per unit area associated with the translational motion according to Eq. (6.3), with other parameters selected as $B = 31\,\text{nm}$, $h = 0.34\,\text{nm}$, $r_0 = 0.8\,\text{nm}$ and $D = 0.11\,\text{nNnm}$. Figure 6.3d shows the variation of the force with CNS rolling along the substrate. Interestingly,

in the present simulation system, the force only shows small variations as the CNS rolls forward or backward. According to Eq. (6.3), the variations are mainly due to the elastic bending part $\frac{D}{2\left(\frac{(B-x)h}{\pi}+r_0^2\right)}$, indicating that the elastic energy makes only minor contributions to the total force. We note that the energy release rate per unit area is on the order of $-0.06$ nN/nm for $\lambda_{CS}=0.8$ and $\lambda_{CC}=1.0$, and 0.08 nN/nm for $\lambda_{CS}=0.8$ and $\lambda_{CC}=0.6$. Therefore, the range of driving force is about $-0.6\sim 0.8$ nN for a CNS-based nanoactuator with width 10 nm, and $-6\sim 8$ nN with width 100 nm.

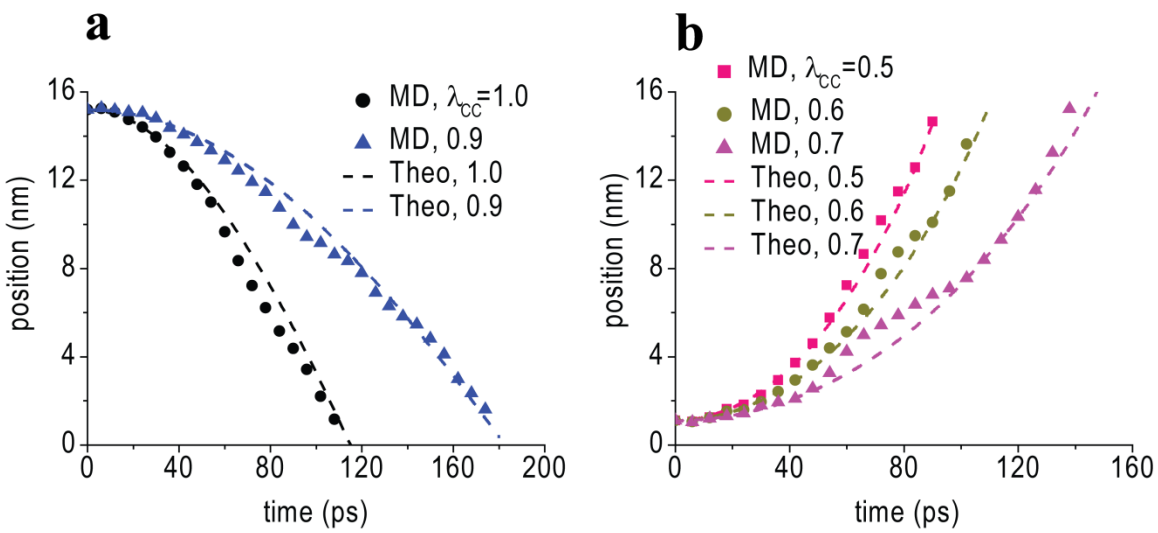


Figure 6.4: Position of CNS as a function of time. Dash lines show the theoretical results and scatters show the MD results. The CNS rolls **(a)** rightward and **(b)** leftward with different CNS-CNS interactions. [108]

To further investigate the linear motion of CNS on substrate, we numerically solve Eq. (6.7), with additional parameters set as $\rho=\frac{12\times 1.66054\times 10^{-27}}{3\sqrt{3}/4\times 0.142^2\times 10^{-18}}$ kg/m2, $M_0=960\times 12\times 1.66054\times 10^{-27}$ kg and $L=3.8$ nm. The predicted motion of CNS for

different tuning parameters, as shown in Figure 6.4a and 6.4b (dashed lines), agrees well with the corresponding MD results (scatters), indicating that our theoretical model is capable of predicting the rolling motion of CNS on substrate. There are some slight deviations between MD results and theoretical prediction when the total force is small (Fig. 6.4, blue and magenta triangles). This is attributed to the insertion of MWCNT which causes the shape of CNS to deviate slightly from what is described by the radial function (Fig. 6.1).

### 6.3 Motions of carbon nanoscrolls on substrate

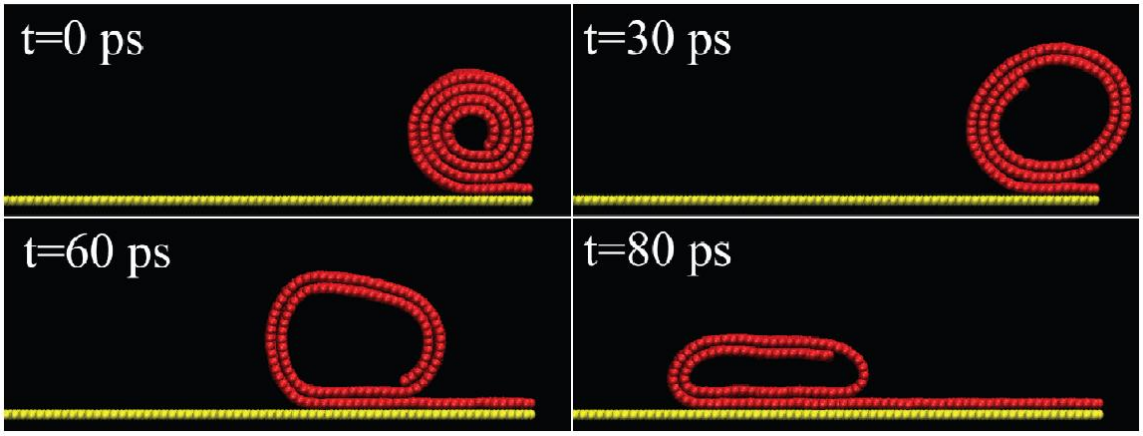


Figure 6.5: Snapshots of molecular dynamics simulation of carbon nanoscrolls (CNS) (red colour) expanding and rolling on the graphite substrate (yellow colour). The tuning parameter for CNS-CNS and CNS-Graphite interactions are $\lambda_{CC} = 0.6$ and $\lambda_{CS} = 0.8$. [108]

We emphasize that constraining the core size of the CNS is essential in realizing the controlled translational motion of CNS on substrate. To demonstrate this, we repeat the simulation without any insertion into CNS. The results are shown in Figure 6.5. It is seen that the CNS does not unroll leftward as the CNS-CNS interaction decreases. Instead it

remains at the initial position while expanding its core (Fig. 6.5, $t = 30$ ps). This simulation shows that, when its core is unconstrained, frictionless layer sliding with core expansion is the preferred mode of energy reduction. To reveal the underlying mechanism, we compare the energy release rates associated with the rolling and expansion of CNS. The energy release rate for expansion of CNS has been obtained in Chapter 5 as

$$f_{\text{expansion}} = \frac{\pi D}{h}\frac{R^2 - r_0^2}{R^2}\frac{1}{r_0} - 2\pi\gamma_{CC}\left(1 + \frac{r_0}{R}\right), \tag{6.9}$$

and that for rolling of CNS is given by Eq. (6.3).

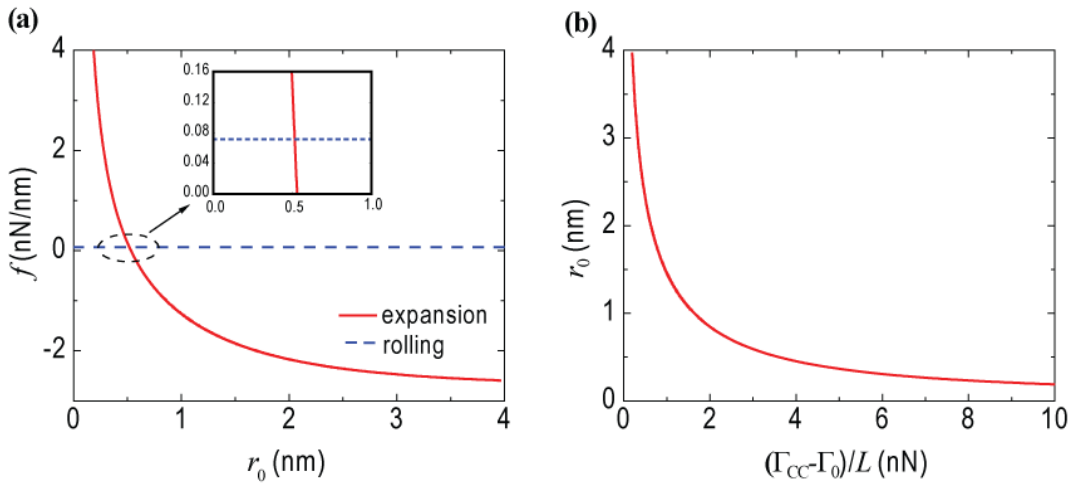


Figure 6.6: Competing core expansion and rolling motion of a CNS on substrate. (**a**) The energy release rate associated with core expansion of a CNS is seen to easily dominate over that associated with the CNS rolling on a substrate as the system is perturbed away far from equilibrium by an external field. (**b**) The equilibrium core size as a function of the surface energy of CNS. The parameters are selected as $B = 31$ nm, $h = 0.34$ nm, $D = 0.11$ nNnm, $\lambda_{CC} = 0.6$, and $\lambda_{CS} = 0.8$. [108]

These energy release rates are plotted as a function of the core radius in Figure 6.6a with typical parameters for the CNS on graphite. Figure 6.6b plots the core radius as a

function of surface energy of CNS. As an external field is applied, the surface energy decreases while the equilibrium core radius increases. In this case, Figure 6.6a shows that there is a tendency for the CNS core to expand toward the new equilibrium size, with energy release rate orders of magnitude higher than that associated with the rolling motion. Therefore, when an external field is applied to perturb the equilibrium state of CNS, the dominant mode of response of CNS is core expansion. As the inner core $r_0$ increases, the energy release rate $f_{\text{expansion}}$ associated with core expansion drops rapidly, and eventually the rolling motion is initiated for further energy reduction. As shown in Figure 6.5, the rolling motion starts only after substantial expansion of the inner core ($t = 60$ ps), at which the shape of CNS has changed so much that Eq. (6.1) can no longer be used to describe the elastic energy in the system. As the number of layers is reduced by core expansion, the CNS collapses on the substrate at $t = 80$ ps. In this situation, the motion of CNS is rather complicated and unpredictable. We thus conclude that the core size of CNS must be fully constrained in order to design a controllable CNS-based nanoactuator.

# *Chapter 7*

# *CNS-based tunable water channel*

Water transport through channel proteins across cell membranes has long been of strong interest to cell biology [109-111]. The development of nanotechnology has expanded the scope of water channels to including nanomaterials such as carbon nanotubes (CNTs). It has been shown that a single walled CNT can host a single chain of water molecules which can burst out of the CNT spontaneously [41]. This study has inspired a series of further studies on tunable CNT-based water channels. So far, a number of approaches have been explored in the literature to control water transport through a CNT, including use of an external force to adjust the internal capacity of the CNT [43], application of an electric field to change the dipole orientations of the confined water chain [44, 45] as well as ways to polarize carbon atoms [42, 46, 47] and to change electrostatic interactions by adding ions [48, 49] in the system.

Due to their rigid, closed tubular structure, the CNT-based water channels only have limited permeability. In contrast to the closed tubular structure of CNTs, the spiral structure of CNSs is much more flexible in the radial direction and thus more sensitive to

external stimuli. Here we propose a class of novel, tunable water channels based on carbon nanoscrolls (CNSs) whose core radius can be tuned over a broad size range by an applied DC/AC electric field [96].

### 7.1 Model description

In the proposed CNS-based water channel, the forming graphene with dimension $20 \times 4$ $nm^2$ is rolled into a zigzag CNS with axial length equal to 4 nm (Figs. 7.1B, C). The CNS is then embedded in a lipid bilayer consisting of 128 DPPC molecules which are downloaded from Reference [112] (Fig 7.1A). The head group of DPPC molecules is constrained along the axis direction of CNS with a force constant 1000 $kJmol^{-1}nm^{-1}$ to ensure a stable simulation system. Tip3p water molecules [93] are added until the membrane patch is fully hydrated at 50 water molecules per lipid. The simulation package Gromacs4 [91] is then used to simulate the structure and transport of water inside the CNS. The electrostatic interaction of water solvent is evaluated by the particle mesh Ewald method (PME) [94, 95]. A cut-off distance of 1.4 nm is used for both Ewald and van der Waals interactions. Room temperature of 300 K and atmospheric pressure of 1 bar are maintained by the v-rescale method [113] and the Parrinello-Rahman method [114], respectively, both at a time increment of 0.1 ps. Periodic boundary conditions and a simulation time step of 2 fs are adopted in all simulations. The system is first equilibrated for 2 ns, then followed by a 10 ns run to determine the flow rate of water. The carbon-carbon bond length 0.142 nm and angle $120^\circ$ are maintained by a Morse bond, a harmonic cosine of the bending angle and a twofold torsion potential [92].

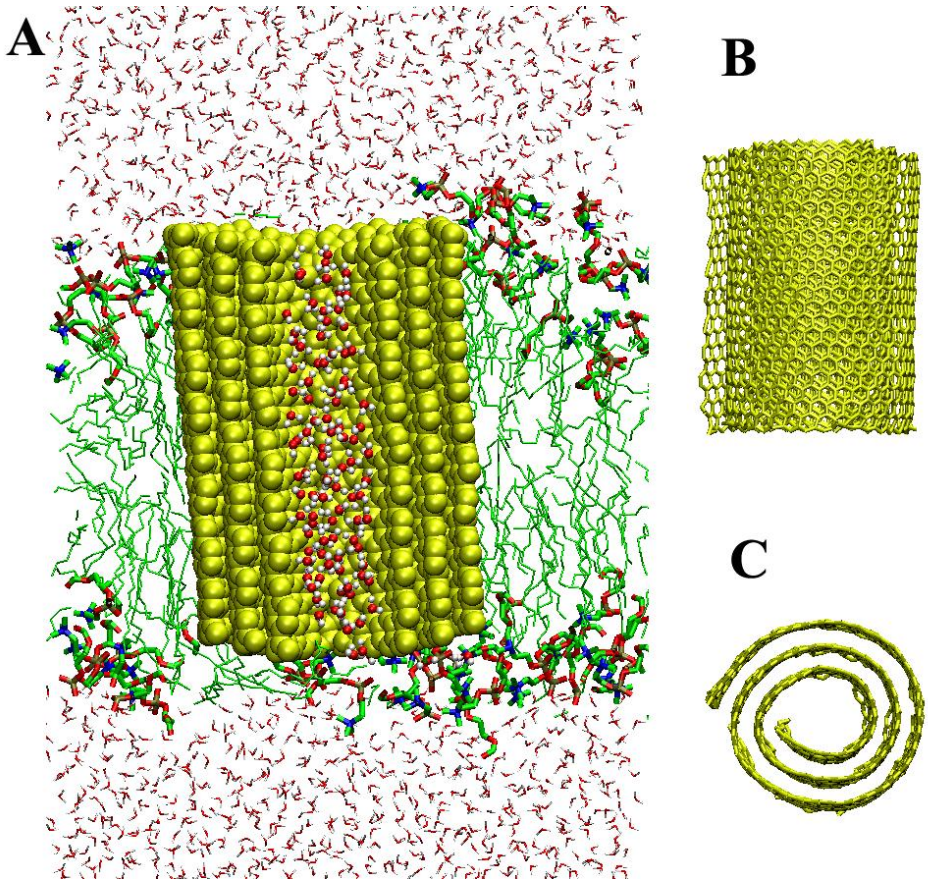


Figure 7.1: The CNS-based water channel. (**A**) The water box with the CNS serving as a water channel embedded inside a DPPC bilayer. (**B**) Side and (**C**) top views of the CNS. [96]

The nonbonded van der Waals interactions are described by the Lennard-Jones (LJ) potential with parameters listed in Table 7.1.

**Table 7.1: Interaction potential parameters** [41, 92]

| | |
|---|---|
| $\varepsilon_{OO} = 0.6367\text{kJ/mol}$ | $\sigma_{OO} = 0.3151\text{nm}$ |
| $\varepsilon_{CC} = 0.3601\text{kJ/mol}$ | $\sigma_{CC} = 0.34\text{nm}$ |
| $\varepsilon_{CO} = 0.4787\text{kJ/mol}$ | $\sigma_{CO} = 0.3275\text{nm}$ |

In our simulations, an external electric field is applied along the axial direction of CNS and directly influences the behaviors of water and lipid molecules. On the other hand, the carbon atoms in the CNS are modeled as non-polar, except that the core size of the CNS changes in response to the electric field. According to Figure 4.1, the effect of an applied electric field on CNS can be represented by an effective surface energy of CNS $\gamma_{eff}$ which is

$$\gamma_{eff} = \gamma_{vdW} + \gamma_{dipole}, \tag{7.1}$$

where $\gamma_{vdW}$ is the surface energy due to van der Waals interaction between carbon atoms and $\gamma_{dipole}$ is that due dipole-dipole interaction as described in Chapter 4.

**Table 7.2**: **Tuning parameter $\lambda$ for different carbon-carbon interactions and the corresponding effective surface energies and electric fields.** [96]

| | A | B | C | D | E | F | G | H | I |
|---|---|---|---|---|---|---|---|---|---|
| $\lambda$ | 0.4 | 0.5 | 0.6 | 0.7 | 0.8 | 0.9 | 1.0 | 1.2 | 1.6 |
| $r\,(\mathrm{nm})$ | 0.99 | 0.95 | 0.81 | 0.72 | 0.67 | 0.61 | 0.48 | 0.35 | 0.18 |
| $\gamma_{eff}\ (\mathrm{nN/nm})$ | 0.122 | 0.134 | 0.141 | 0.163 | 0.181 | 0.196 | 0.212 | 0.354 | 0.789 |
| $E\ (\mathrm{V/nm})$ | 0.39 | 0.36 | 0.34 | 0.29 | 0.23 | 0.16 | 0 | -- | -- |

In actual simulations, this is accomplished by multiplying the parameter $\varepsilon_{CC}$ by a tuning factor $\lambda$ so that the effective nonbonded carbon-carbon interaction is given by

$$U(r_{ij},\lambda)=4\lambda\varepsilon_{CC}\left[\left(\frac{\sigma_{CC}}{r_{ij}}\right)^{12}-\left(\frac{\sigma_{CC}}{r_{ij}}\right)^{6}\right]. \tag{7.2}$$

Table 7.2 lists all the values used in the simulations. Although the applied electric field tends to reduce the effective surface energy, i.e. $\lambda<1$, we have also considered the $\lambda>1$ case.

## 7.2 Enhanced flow rate and water diffusivity

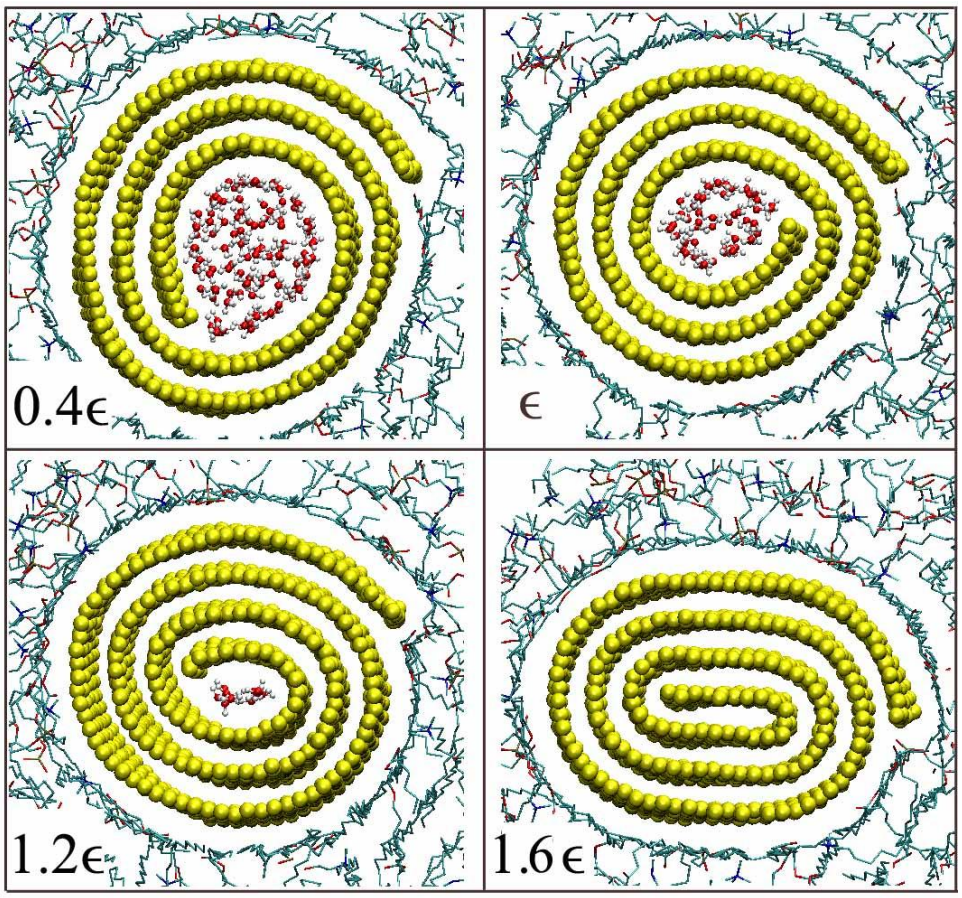


Figure 7.2: Simulation snapshots of CNSs with water molecules confined inside the inner core for different values of the effective surface energy. Water molecules outside the inner core are not shown for clarity. [96]

During the simulations, the CNS-water interaction energy decreases quickly for the first 0.4 ns simulations (Fig. 7.3A). Thereafter the interaction energy is seen to gradually saturate, indicating the approach of equilibrium. Figure 7.2 shows that the equilibrium water structure inside the core of CNSs depends on the effective surface energy. Reducing the surface energy tends to enlarge the core size, thereby incorporating more water molecules, while increasing the surface energy tends to reduce the core size. For example, substantially more water molecules are filled inside the core in case A ($\lambda = 0.4$) than in case G ($\lambda = 1.0$). As $\lambda$ is increased to 1.2, the core size becomes so small that the confined water molecules form two linear chains (Fig. 7.2, 7.4). Further increasing $\lambda$ to 1.6 results in complete depletion of water from the CNS core.

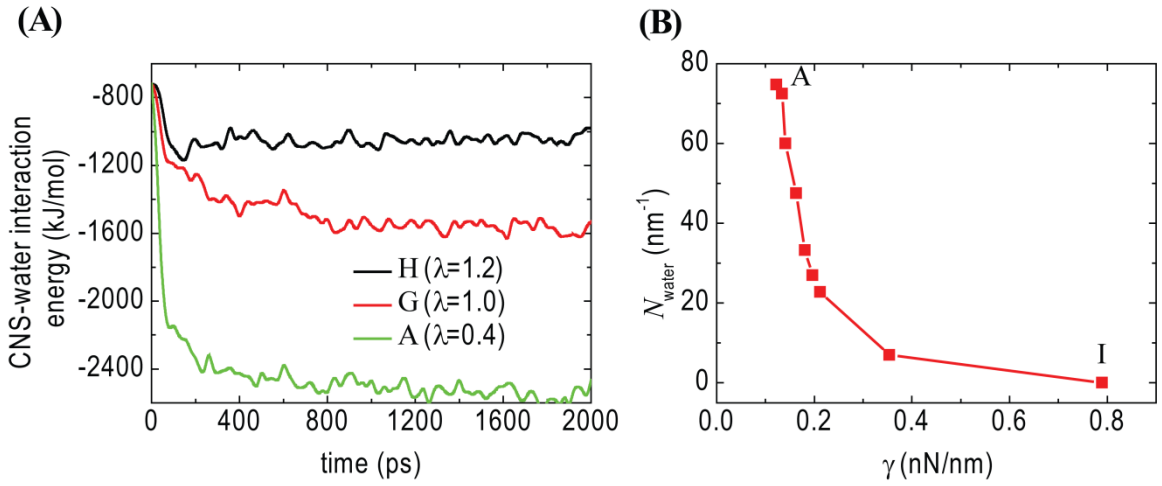


Figure 7.3: (**A**) The simulated evolution of CNS-water interaction energy as a function of the simulation time. The interaction energy decreases quickly for the first 400 ps and gradually reaches an equilibrium value. (**B**) The number of water molecules per unit axial length confined inside the CNS as a function of the effective surface energy. The parameters listed in Tables 7.1 and 7.2 are adopted. [96]

It can be seen in Figure 7.3A that the equilibrium CNS-water interaction energy decreases as more water molecules are incorporated into the core. Figure 7.3B shows that

the number of water molecules inside the CNS, $N_{water}$, scales with the inverse square of the effective surface energy, i.e. $N_{water} \propto 1/\gamma^2$, which can be explained from the relations $N_{water} \sim \pi r^2$ and $r \sim 1/\gamma$. It is also interesting that water molecules inside the CNS core form a spiral structure in extension of the CNS structure (Fig. 7.2). This phenomenon is similar to previous findings that the structure of encapsulated water molecules in carbon nanotubes tends to mimic that of the confining tubular structure of graphene [115].

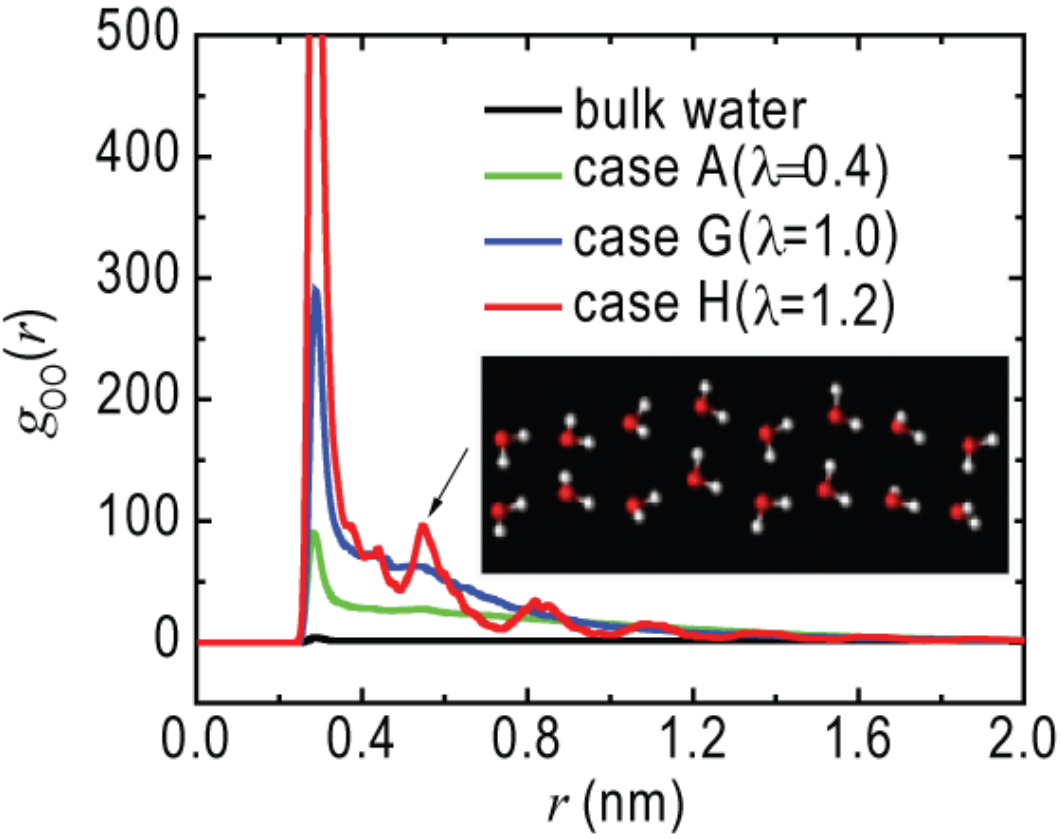


Figure 7.4: Radial distribution functions (RDF) of oxygen atoms in four different cases. Inset shows the configuration of two linear chains of confined water molecules in case H ($\lambda = 1.2$). [96]

Figure 7.4 plots the radial pair distribution function of oxygen-oxygen atoms. The first peak at $r = 0.28\,\text{nm}$ is due to the strong hydrogen-bonding network of water. For case H ($\lambda = 1.2$), a second peak appears at $r = 0.55\,\text{nm}$, corresponding to the diagonal distance of a rhombus structure formed by the two linear chains of water confined inside the core.

The flow rate of water is defined as the number of water molecules entering per unit time at one end of the CNS and leaving at the other end. Our simulations (Fig. 7.5A) indicate that the average flow rate increases monotonically with increasing inner radius (Fig. 7.5C). For the inner radius of 0.35 nm, the flow rate is about 30 $ns^{-1}$, which is comparable to Hummer's results for water flow inside a (6,6) CNT [41]. As the inner radius is increased to 0.95 nm, the flow rate increases to 284 $ns^{-1}$. Considering the fact that there is no osmotic pressure in our system, the change in flow rate can be attributed to changes in core size and water diffusivity in the axial direction $D_{axial}$. To determine $D_{axial}$, we first calculate the axial diffusivity of each water molecule that are or were once inside the CNS, and then perform a weighted average of the calculated values with respect to the corresponding probability distribution function shown in Figure 7.5B. Figure 7.5D displays the calculated diffusivity as a function of the core radius. In the absence of an electric field, the CNS-water interaction energy would decrease as the core size is increased, resulting in increasing water diffusivity. For example, the CNS-water interaction energy is about -17 kJ/mol when $r = 0.18\,\text{nm}$ ($\lambda = 1.6$) and -9.4 kJ/mol when $r = 0.35\,\text{nm}$ ($\lambda = 1.2$). These behaviors are consistent with previous findings that the diffusivity of water inside a CNT increases with the CNT radius [116]. However, this trend is seen to be completely reversed by the presence of an applied electric field. Fig. 7.5D shows that, as an electric field is applied to expand the core of CNS, water

diffusivity decreases, rather than increases as expected from the size effect alone. This phenomenon can be attributed to enhanced alignment of water dipoles along the direction of the electric field, which tends to decrease the diffusivity. Similar phenomenon has also been reported in the study of water flow through CNTs in the presence of an electric field [45].

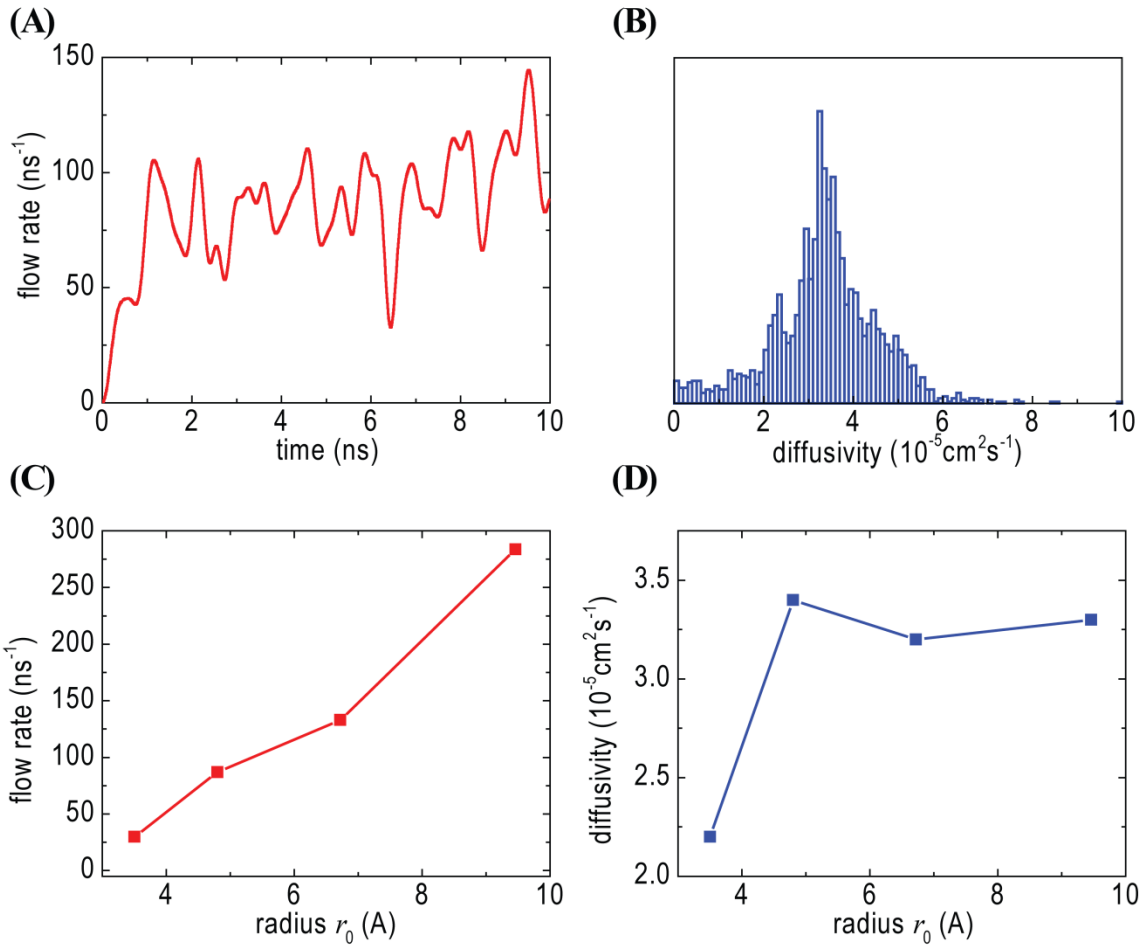


Figure 7.5: Flow rate and diffusivity of water in the CNS. (**A**) Flow rate as a function of time for case G ( $\lambda = 1.0$ ). The data has been smoothed with an FFT filter with 0.3 ns width. (**B**) Probability distribution of axial diffusivity of water confined inside the CNS for case G ( $\lambda = 1.0$ ). (**C**) Averaged flow rate as a function of the core size of the CNS. (**D**) Averaged water axial diffusivity as a function of the core size of the CNS. The four points represent $\lambda = 0.5$, 0.8, 1.0, 1.2, respectively. [96]

### 7.3 DC field and AC field

To investigate the effect of an applied AC electric field, in which case the effective surface energy changes with time, we consider

$$\lambda(t) = \frac{1-\beta}{2}\left[1+\cos(2\pi f t)\right] + \beta\,, \tag{7.3}$$

where $f$ is the frequency of the AC field and $\beta$ is a parameter depending on the field strength. Here we set $\beta = 0.4$ so that $\lambda$ varies from 0.4 to 1 (Fig. 7.6A).

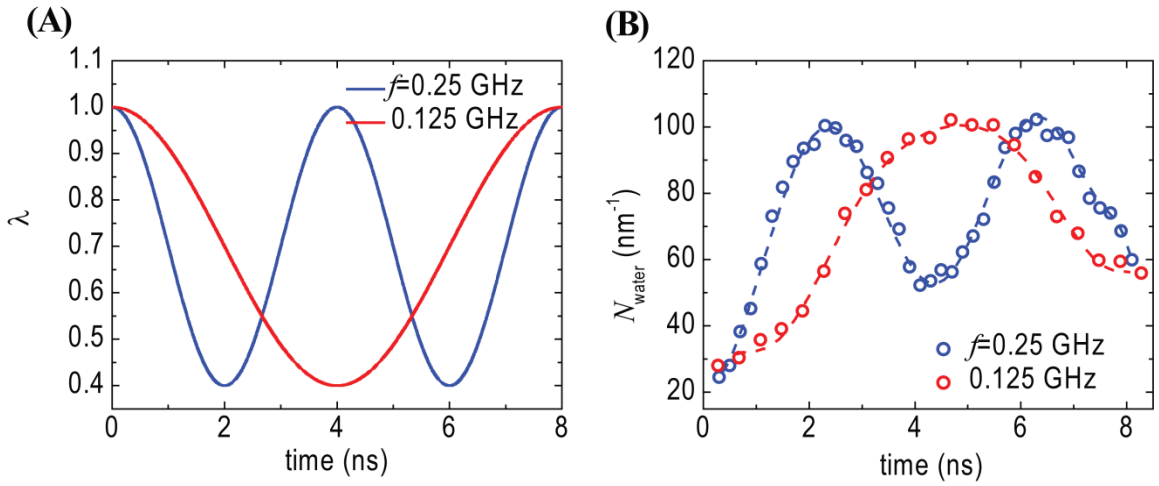


Figure 7.6: (**A**) Tuning parameter $\lambda$ as a function of time. (**B**) The number of water molecules per unit axial length confined inside the CNS as a function of time. [96]

Simulations are conducted with the frequency $f$ set at 0.25 and 0.125 GHz. The results show that the inner radius of the CNS varies periodically with the same frequency as that of the applied AC field. The variation of the number of water molecules inside the CNS is shown in Figure 7.6B. The maximum number of confined water molecules (about 100 $nm^{-1}$) is much larger than that in the DC case of $\lambda = 0.4$ (about 75 $nm^{-1}$), indicating that the core of the CNS can be expanded to a much larger size under an AC field. It is also

found that the AC flow rates are greatly enhanced in comparison with the corresponding results under a DC field, as shown in Table 7.3. When $f = 0.125$GHz and $\lambda$ varies from 0.4 to 1, the mean flow rate is about 386 $ns^{-1}$, which can be compared to the DC flow rate of 305 $ns^{-1}$ when $\lambda = 0.4$. When $f = 0.25$ GHz, the mean flow rate is further enhanced to 589 $ns^{-1}$, nearly twice the corresponding value in the DC case of $\lambda = 0.4$. This increase in mean flow rate at increasing frequency $f$, combined with the fact that the AC flow rates are significantly higher than the DC flow rates, may indicate a resonance phenomenon, although much further work is required to clarify the detailed mechanism. It seems that the enhanced AC flow rate can be attributed to pulsated flow stimulated by periodic contraction of the CNS. Table 7.3 also shows that the mean axial diffusivities of water molecules under an AC field are larger than the corresponding upper bound in the DC case of $\lambda = 0.4$ ($D_{\text{axial}} = 3.37 \times 10^{-5}$ $cm^2s^{-1}$). Therefore, it seems that an AC electric field can greatly stimulate and enhance water flow in CNSs.

**Table 7.3: Tuning parameter $\lambda$ and $f$ for different carbon-carbon interactions and the corresponding water flow rates and axial diffusivities within the CNS core.** [96]

| | flow rate ($ns^{-1}$) | axial diffusivity ($10^{-5}$ $cm^2s^{-1}$) |
|---|---|---|
| DC: $\lambda = 0.4$ | 305 | 3.37 |
| AC: $\lambda$~0.4-1, $f = 0.125$ GHz | 386 | 3.42 |
| AC: $\lambda$~0.4-1, $f = 0.25$ GHz | 589 | 3.58 |

We also point out some potential pitfalls of our study. Figure 4.1B shows that the surface energy of a CNS will be significantly altered only by an applied electric field on the order of 0.2 V/nm. This value is quite high compared to the typical membrane potential of 0.016~0.027 V/nm [45]. The electric field used in our simulations is in the range of 0-0.39 V/nm, while the breakdown strength of membrane has been reported to be around 0.14 V/nm [117]. Although Figure 4.1B shows that it is certainly possible to achieve full tuning of CNS within the breakdown strength of membrane by increasing the length of the basal graphene sheet, it will be important from a practical point of view to investigate strategies to enhance the sensitivity of CNS to an applied electric field through functionalizations and/or to tune the surface energy of CNS via other applied fields. Further studies will be directed along this line of research in the future.

# *Chapter 8*

# *CNS-based molecular crystal*

In the preceding Chapters, we have studied the structural and dynamical properties of a single CNS. Here we show that CNS-based molecular crystals also possess extrodornary mechanical properties that may have many promising applications in engineering.

To simplify the model, we consider a closely packed molecular crystal of CNSs aligned with scroll axes all parallel to the out-of-plane direction. The CNSs are closely packed so that each CNS has 6 nearest neighbours. In the MD simulations, this configuration is realized by setting up a triclinic unit cell with periodic boundary conditions.

## 8.1 Giant electrostriction of CNS crystal

Electrostriction is a property of dielectric materials that cause them to change their shape under an applied electric field. In Chapter 7, we have shown that an electric field applied in the axial direction would cause a CNS to expand its core in response to the reduced interlayer interaction energy. This phenomenon is similar to electrostriction. Here the

core expansion is due to a decrease in the surface energy of CNS induced by dipole-dipole repulsive interaction. However, typical electrostrictive materials reduce their thickness in the direction of an applied electric field due to dipole-dipole attractive interactions, while increase the thickness in orthogonal directions due to Poisson's contraction. Therefore, rigorously speaking, CNS is a special electrostrictive material. In this Chapter, MD simulations and quantitative calculations are employed to explore that the giant electrostriction property of a CNS crystal..

In the MD simulations, we consider a triclinic simulation box containing of CNSs formed from a basal graphene sheet with length $B$=50 nm under periodic boundary conditions. After equilibrium in the NPT ensemble, the molecular volume of the CNS crystal is calculated. The effect of an applied electric field is again represented by an effective surface energy of CNS $\gamma_{eff}$ as described in Eq. (7.1). In actual simulations, this is accomplished by multiplying the parameter $\varepsilon_{CC}$ by a tuning factor $\lambda$ so that the effective nonbonded carbon-carbon interaction is given by Eq. (7.2).

Figure 8.1 shows equilibrium configurations of the CNS crystal under an increasing electric field which reduces the effective surface energy through $\lambda$. The strain as a function of the applied electric field strength is shown in Figure 8.2A. It is seen that the CNS crystal tends to expand as the electric field strength increases.

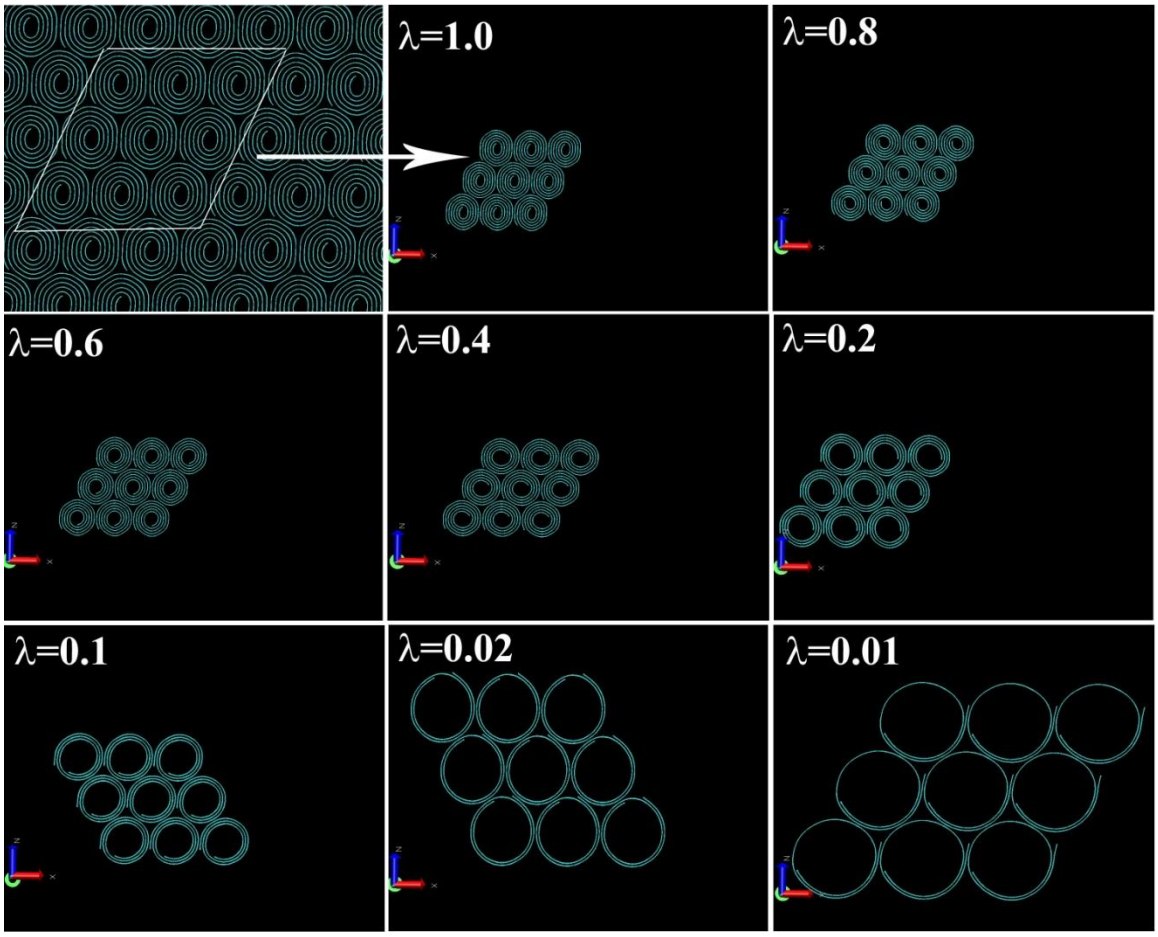


Figure 8.1: Equilibrium configurations of a CNS crystal under different electric fields represented by parameter $\lambda$.

The electrostriction coefficient is an important parameter describing electrostrictive materials. Materials possessing large electrostriction coefficient are sensitive to the electric field and have large electrostriction capability. According to the definition, the electrostriction coefficient ($Q_{ijkl}$) is a fourth rank tensor relating strain and dipole moments as

$$\varepsilon_{ij} = Q_{ijkl} p_k p_l . \tag{8.1}$$

In the present problem, the strain of interest is in the radial direction of CNSs while the dipole moments are in the axial direction, in which case the relevant electrostriction coefficient is

$$Q = Q_{1133} = Q_{2233} = \frac{1}{(4\pi\varepsilon_0\alpha)^2}\frac{d\varepsilon}{d(E^2)}. \tag{8.2}$$

Figure 8.2B shows the variation of the electrostriction coefficient as the applied electric field increases. Typical electrostrictive materials have electrostriction coefficients in the range of 1-10$^{-3}$ m$^4$C$^{-2}$, and some polymers show giant electrostriction coefficients of about 10 m$^4$C$^{-2}$. Apparently, the CNS crystals have features of giant electrostriction.

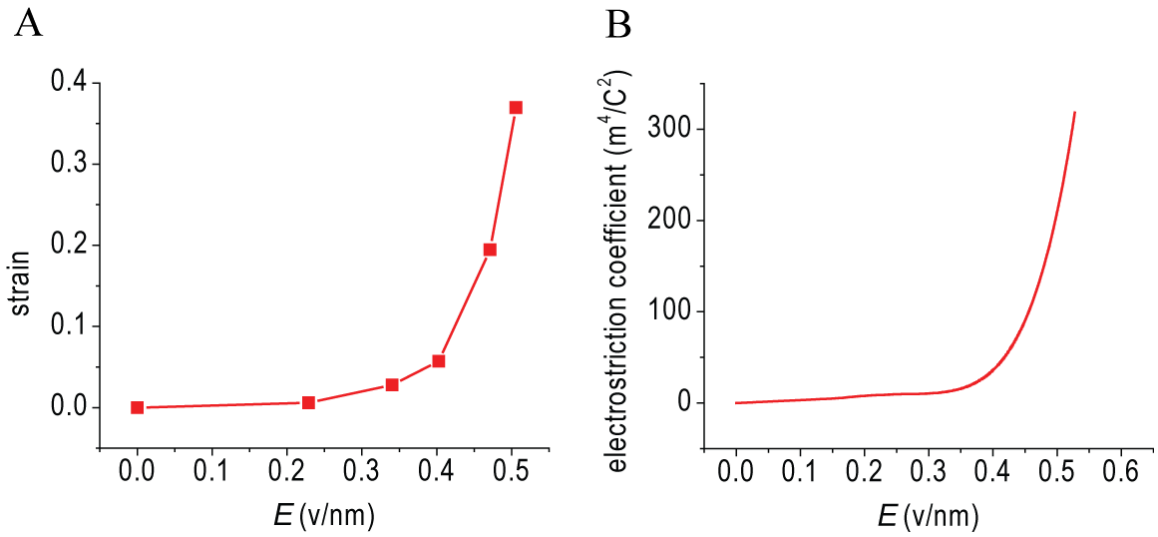


Figure 8.2: The (**A**) strain and (**B**) electrostriction coefficient of the CNS crystal under consideration as a function of the electric field strength.

## 8.2 Hyperelastic behavior in biaxial compression

In addition to giant electrostriction, a CNS crystal also has interesting hyperelastic properties. In the axial direction, CNSs are expected to have ultrahigh Young's modulus

and strength, similar to CNTs. In the radial direction, however, the flexible configuration enables a CNS to undergo large deformation under relatively small loading.

To demonstrate this, we conduct MD simulations in which the CNS crystal is subjected to compression in the radial direction. Consider a triclinic simulation box of CNSs formed from a basal graphene sheet with length $B$=100 nm under periodic boundary conditions in all three dimensions. After equilibrium in the NPT ensemble, the CNS crystal shows a triangular lattice configuration (Fig. 8.3). It is then compressed at a constant strain rate of $10^{-3}$ $ps^{-1}$. The LAMMPS [82] code and the AIREBO potential [83] are used in the simulations. Based on the second generation of Brenner potential [84], the AIREBO potential has two more additional terms: One is the Lennard-Jones term that describes the long range interaction, another is the torsion term that accounts for the dihedral angle contribution. In the MD simulations, a tuning factor $\lambda$ is used in the LJ term to represent the effect of an applied electric field, similar to those described in the preceding chapters.

The results show that the compression forces the CNSs to contract inner cores until they are tightly packed (Fig. 8.3). However, once the applied load is removed, the crystal recovers to the initial state. The stress-strain curves show that the profile is relatively flat at small strains, indicating a relatively small bulk modulus which can be attributed to the easy deformation mode via core contraction. As the strain increases and the crystal becomes packed, the slope of the stress-strain profile becomes sharp, indicating steeply rising bulk modulus in the highly packed state. The stress-strain curves for loading and unloading fit well with each other, indicating with negligible energy dissipation.

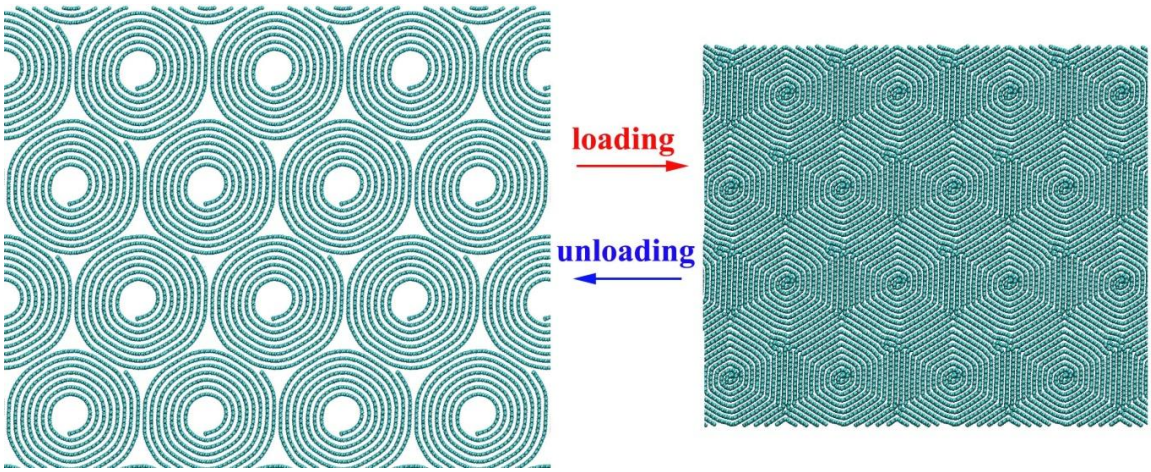


Figure 8.3: Snapshots of MD simulation results showing the initial and final states of a CNS crystal under biaxial compression/decompression.

The influence of an electric field on biaxial compression/decompression of a CNS crystal is further investigated by tuning the LJ potential through a multiplication factor $\lambda$ . The core expansion of CNSs under electric field results in a large strain during compression (Fig. 8.4A). The slopes of the stress-strain curves at initial loading are different under different electric field strengths, indicating that the bulk modulus of the crystal varies with the applied electric field (Fig. 8.4A). Figure 8.4B shows that the bulk modulus of the CNS crystal decreases as the electric field increases ( $\lambda$ decreases), corresponding to electro-softening.

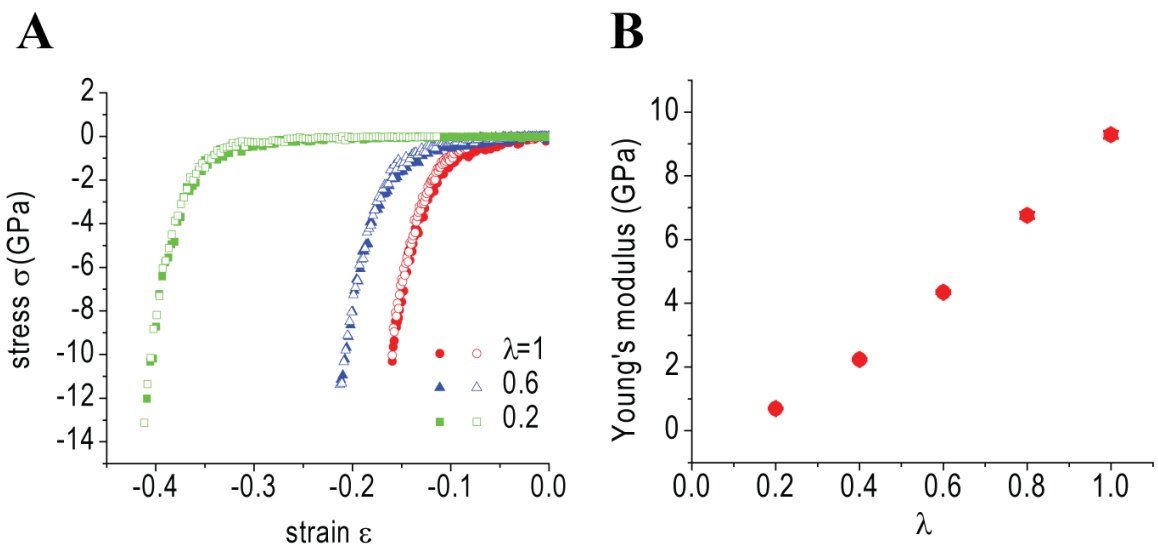


Figure 8.4: (A) Stress-strain profiles of CNSs under biaxial compressing (open)/decompressing (close) under different electric field strengths. (B) Young's modulus at initial loading as a function of the electric field.

### 8.3 Deformation of CNS crystal under axial stretching

It has been widely recognized that carbon nanotubes have ultrahigh strength in the axial direction. With the strength comparable to that of steel, the CNTs are considered as promising candidates for high strength and light weight composite materials. Since CNSs have similar structural features as CNTs in the axial direction while being highly flexible in the radial direction, we may wonder about their properties under axial stretching. In this Section, we conduct MD simulations to investigate the variation of the core of CNSs under axial stretching.

We use the same code and potential as those in Section 8.2. To quantitatively capture the bending stiffness and the surface energy, single CNSs, rather than a CNS crystal, is considered during the simulations. Two ends of a CNS are stretched in the axial direction with a constant strain rate of $10^{-4}$ $ps^{-1}$ (Fig. 8.5). Two types of CNSs, zigzag and armchair, are selected in the simulations.

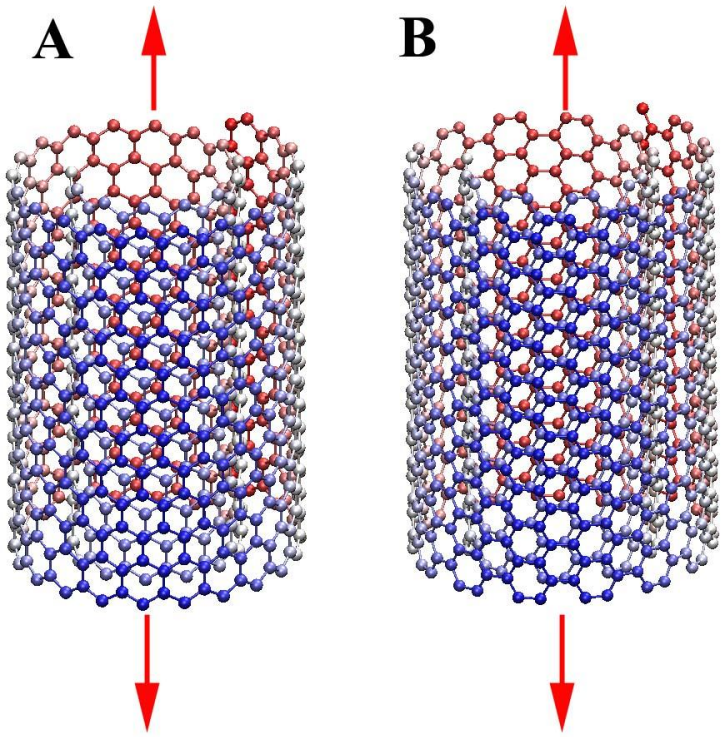


Figure 8.5: Schematic illustrations of (A) zigzag and (B) armchair CNSs subjected to axial loading.

Figure 8.6 shows selected snapshots from the simulation results. It is seen that for the zigzag CNS, the core initially expands as the CNS is stretched (Fig. 8.6A), signifying a negative Poisson's ratio. Apparently, the zigzag CNSs exhibit a negative Poisson's ratio under axial stretching. However, this negative Poisson ratio holds only below a critical strain. When the strain reaches 0.25, the core starts to contract, indicating a transition from negative to positive Poisson's ratio.

For the armchair CNS, however, the core is seen to continuously contract under axial stretching. Why would the core of CNSs change during axial stretching? Why is there a transition from a negative to a positive Poisson's ratio for the zigzag CNS? Why

does the armchair CNS behave differently from the zigzag CNS? These questions are further investigated in the following.

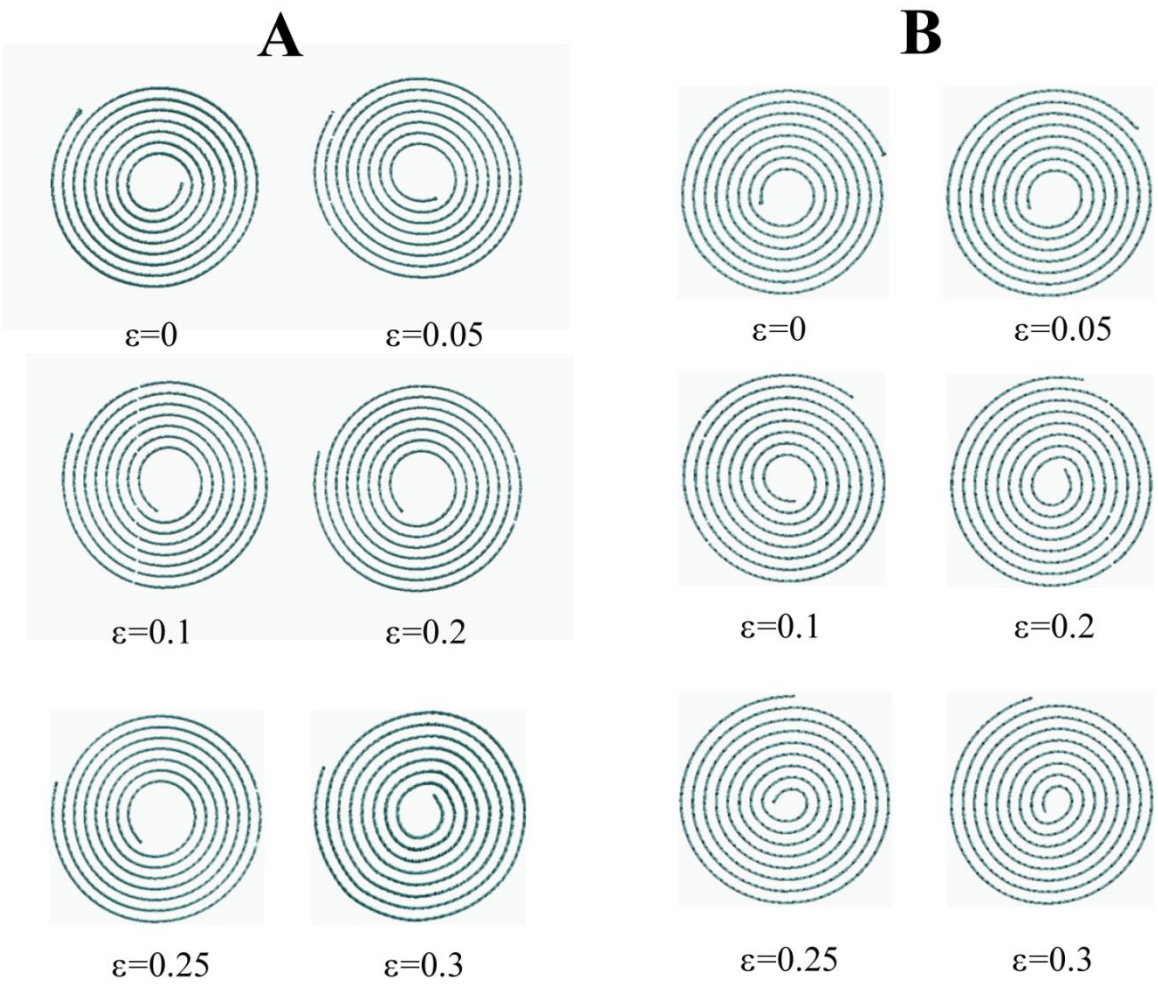


Figure 8.6: Configurations of (A) zigzag and (B) armchair CNSs under axial stretching to different strain levels.

As we have discussed in Chapter 3, the core size of CNSs is determined by the surface energy of CNSs, the bending modulus of graphene, the difference between the pressure inside the core of the CNS and that on its outer surface, as well as the interlayer spacing. Changing each of these parameters would alter its core size. During the axial

stretching, there is no pressure difference and no change of interlayer spacing, and possible remaining mechanisms include changes in bending stiffness of graphene and/or the surface energy of CNSs.

To investigate the bending stiffness of graphene during axial stretching, we adopt a method described in [118] where the bending stiffness of graphene is obtained by rolling a series of graphene strips with different lengths into CNTs with different radii. The bending stiffness of graphene is then extracted from the curvature-dependent strain energies of the CNTs, as described in Eq. (3.26). In the present case, we stretch the graphene along the rolling axis to some fixed strain before forming the CNTs. The stretching of graphene is conducted with LAMMPS code and the AIREBO potential in the NPT ensemble.

Figure 8.7 shows the bending stiffness of graphene for zigzag and armchair CNSs under different axial strains. It is seen that in both cases the stiffness decreases as the strain increases. We also find the surface energy at different strains according to the method described in Chapter 3. It is shown that the surface energy also decreases as the strain increases, presumably due to the decrease in carbon atom density of the graphene. From Figure 8.7 we may see that the decreasing trends of the bending stiffness and surface energy are different for zigzag and armchair CNSs. For zigzag CNSs, the surface energy decreases faster than the bending stiffness in the initial stage, resulting in the core expansion and a negative Poisson ratio. However, after reaching a critical strain, the decrease of bending stiffness prevails, leading to eventual contraction of CNSs. For armchair CNSs, however, the decrease of bending stiffness is always faster than that of

surface energy, in agreement with the observation that an armchair CNS continuously contracts during axial stretching.

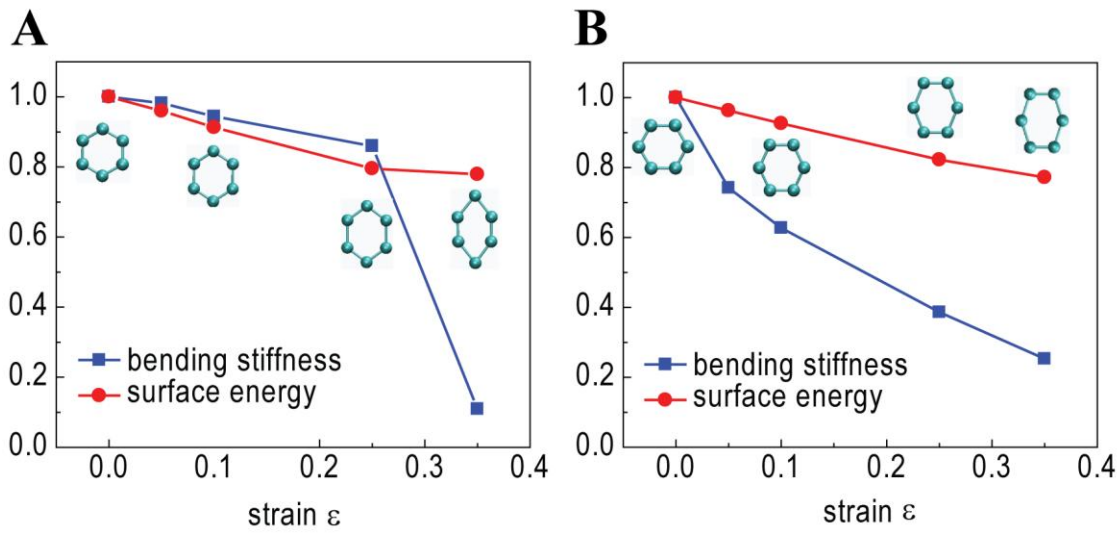


Figure 8.7: Normalized bending stiffness of graphene and surface energy as a function of strain for (A) zigzag and (B) armchair CNSs.

# *Chapter 9*

# *Concluding remarks*

This thesis has examined two topical issues with the mechanics of carbon-based nanomaterials. To investigate how carbon nanotubes (CNTs) enter the cell, we have developed theoretical models as well as coarse grained molecular dynamics (CGMD) simulations. Attention has been focused on the effects of size, aspect ratio and stiffness of CNTs in their uptake by the cell. The main conclusions of the present work are summarized as follows.

(1) Through CGMD simulations and theoretical models, we have shown that, depending on the radius, a carbon nanotube can enter a cell either by wrapping into the cell membrane or by directly piercing through the membrane. The two modes of entry are characterized by a critical radius: sufficiently small tubes favor piercing due to small diffusion distance and large curvature energy, while large tubes favor wrapping due to larger diffusion distance and lower curvature energy. The limitation of this work is that we have artificially set the interaction parameters between CNT's and the lipid head group. Since chemically pure CNT's are hydrophobic and should have weak interactions

with the hydrophilic head groups of lipids, our selection of interaction parameters may have overestimated the interactions between CNT's and the bilayer. The justifications for this set-up are that CNTs for cellular uptake are commonly functionalized and we are primarily interested in the effects of their geometry on tube-bilayer interaction. In other words, we have considered interaction parameters that are only appropriate for decorated CNT's in our CGMD simulations.

(2) Through CGMD simulations and theoretical modeling, we have investigated how multi-walled carbon nanotubes (MWCNTS) enter the cell via receptor-mediated endocytosis. It is found that MWCNTs tend to enter the cell via a tip entry mechanism with the final entry angle determined by two energetic forces. One is the curved membrane induced torque that tends to rotate the nanotube to a large entry angle. The other is the difference of the attractive nanotube-membrane interaction on two sides of the tube: If the interaction on the right side of the nanotube is larger than that on the left side, the nanotube would orient toward the right side, and vice versa. Based on a theoretical framework of receptor mediated endocytosis, the wrapping speeds on both sides of nanotube are found to be identical. In this case the membrane induced torque will dominate and the nanotube is expected to enter a cell via tip entry, which may lead to frustrated endocytosis and even cell death. This work is of fundamental importance to the understanding of physical mechanisms for the cytotoxicity of MWCNTs.

(3) We have also conducted MD simulations to understand the stiffness effect in adhesive wrapping of an elastic vesicle by a membrane. A phase diagram of particle wrapping is determined. The phase transition between partial and full wrapping states is found to be be sensitively dependent on the bending stiffness of the particle. Generally,

stiffer particles require lower adhesion strength to achieve full wrapping and it is more difficult for a cell to engulf softer vesicles: Very soft vesicles may not be able to enter a cell via wrapping. The present work suggests that particle stiffness may play an essential role in endocytosis.

Carbon nanoscrolls (CNS) are a relatively new class of carbon-based nanomaterials, obtained by rolling up a graphene sheet into a scroll with open topology. A major part of the present thesis has been aimed at investigating the structural, dynamical, mechanical and electromechanical properties of CNSs. The main conclusions are summarized as follows.

(4) We have theoretically investigated the basic structure of a carbon nanoscroll and derived an analytical relation between the surface energy, the bending stiffness, the interlayer spacing, the length of the basal graphene sheet, the pressure difference between the inner and outer core of CNS and the core radius of the resulting CNS. Molecular dynamics simulations have been used to verify the theoretical results. The stability and the biaxial constitutive behaviors of pressurized CNS have also been investigated. Under an externally applied pressure, the CNS undergoes biaxial expansion ( $p_i - p_e > 0$ ) or contraction ( $p_i - p_e < 0$ ). We find that there exists a critical size of the CNS core for unstable expansion under a constant pressure. Also, the biaxial modulus of a CNS is found to be sensitively dependent on the applied pressure, increasing with pressure in biaxial compression and decreasing with pressure in biaxial expansion. The biaxial modulus depends on the size and the surface energy of CNSs. These studies suggest possible pressure sensitive applications of CNS in nanotechnology, such as nanopumps

and nanofilters. We propose that the core size of a CNS may be controlled by pressure or mechanical force as well as by surface functionalization. Such tunable nanostructures may have potential also for applications such as nanopore sequencing of DNA, controllable water and ion channels, and gene or drug delivery systems.

(5) We have developed a theoretical model to describe the "breathing" oscillatory motion of a CNS, and have validated the theory with molecular dynamics simulations. It is found that the gigahertz oscillation of CNS can be controlled by tuning the effective surface energy of the system via an applied DC/AC electric field. The energy dissipation rates in the system can be tuned by temperature, basal graphene length and surface energy. These results suggest possible applications of CNS as nanooscillators and nanoactuators. The resonant oscillation of a CNS near its fundamental frequency might be useful for molecular loading/release in gene and drug delivery systems.

(6) A controllable translational nanoactuator based on the rolling and unrolling motion of CNS on a substrate has been proposed and investigated by both theoretical modeling and molecular dynamics simulations. It is found that the theoretical model based on the classical Lagrangian dynamics is fully capable of predicting molecular dynamics simulation results. It is suggested that CNS based linear nanoactuator can be controlled by tuning the effective surface energy of the system via an applied DC/AC electric field as well as adjusting the width of CNS. These results suggest promising applications of CNS as linear actuators and motors in nanomechanical systems.

(7) We have conducted MD simulations of a novel class of tunable water channels based on CNSs. We have shown that it is possible to use dipole-dipole interaction induced by an externally applied electric field to reduce the effective surface energy of a

CNS, so as to controllably increase its core size and the associated water flow rate. We further show that an applied AC field can greatly enhance the flow rates in comparison with a DC field. Compared with CNT-based water channels, the CNS-based channels exhibit much greater water permeability and sensitivity to an applied DC/AC electric field. Besides possible applications as water channels, our tunable CNS channel model can also serve as ion channels across cellular membrane or controllable nanofilters. The tunable core size can effectively prevent the passing of heavy metal ions or nanoparticles.

(8) We have investigated the electrostrictive behaviors of CNS molecular crystals through both MD simulations and theoretical modeling. We found that a CNS crystal undergoes large expansion under an applied electric field, resulting in giant electrostriction. We have also investigated the mechanical behaviors of CNS crystals through biaxial compressing/decompressing. It is found that CNS crystals exhibit hyperelastic behaviors under radial compression. In biaxial compression, an applied electric field causes the CNS crystal to soften with a reduced bulk modulus. Axial stretching could also alter the core size of a CNS: Under axial stretching, zigzag CNSs are observed to undergo core expansion (i.e., a negative Poisson ratio) at small strain and then revert to contraction beyond a critical strain (i.e., positive Poisson ration at large strains); In contrast, under similar axial stretching, armchair CNSs would continuously contract with increasing axial strain. The underneath mechanisms of these deformation modes have been investigated in terms of changes in both bending stiffness and the surface energy by axial stretch.

# *Bibliography*

[1] Moghimi SM and Szebeni J. Stealth liposomes and long circulating nanoparticles: Critical issues in pharmacokinetics, opsonization and protein-binding properties. Progress in Lipid Research 2003;42:463.

[2] Muller RH, Jacobs C and Kayser O. Nanosuspensions as particulate drug formulations in therapy rationale for development and what we can expect for the future. Advanced Drug Delivery Reviews 2001;47:3.

[3] Takeuchi H, Yamamoto H and Kawashima Y. Mucoadhesive nanoparticulate systems for peptide drug delivery. Advanced Drug Delivery Reviews 2001;47:39.

[4] Kumar M, Hellermann G, Lockey RF and Mohapatra SS. Nanoparticle-mediated gene delivery: State of the art. Expert Opinion on Biological Therapy 2004;4:1213.

[5] Drummond TG, Hill MG and Barton JK. Electrochemical DNA sensors. Nature Biotechnology 2003;21:1192.

[6] Penn SG, He L and Natan MJ. Nanoparticles for bioanalysis. Current Opinion in Chemical Biology 2003;7:609.

[7] Alivisatos P. The use of nanocrystals in biological detection. Nature Biotechnology 2004;22:47.

[8] Cui DX, Tian FR, Ozkan CS, Wang M and Gao HJ. Effect of single wall carbon nanotubes on human hek293 cells. Toxicology Letters 2005;155:73.

[9] Bianco A, Hoebeke J, Godefroy S, Chaloin O, Pantarotto D, Briand JP, Muller S, Prato M and Partidos CD. Cationic carbon nanotubes bind to cpg oligodeoxynucleotides and enhance their immunostimulatory properties. Journal of the American Chemical Society 2005;127:58.

[10] Monteiro-Riviere NA, Nemanich RJ, Inman AO, Wang YYY and Riviere JE. Multi-walled carbon nanotube interactions with human epidermal keratinocytes. Toxicology Letters 2005;155:377.

[11] Kam NWS, Jessop TC, Wender PA and Dai HJ. Nanotube molecular transporters: Internalization of carbon nanotube-protein conjugates into mammalian cells. Journal of the American Chemical Society 2004;126:6850.

[12] Kam NWS and Dai HJ. Carbon nanotubes as intracellular protein transporters: Generality and biological functionality. Journal of the American Chemical Society 2005;127:6021.

[13] Kam NWS, O'Connell M, Wisdom JA and Dai HJ. Carbon nanotubes as multifunctional biological transporters and near-infrared agents for selective cancer cell destruction. Proceedings of the National Academy of Sciences of the United States of America 2005;102:11600.

[14] Cherukuri P, Bachilo SM, Litovsky SH and Weisman RB. Near-infrared fluorescence microscopy of single-walled carbon nanotubes in phagocytic cells. Journal of the American Chemical Society 2004;126:15638.

[15] Pantarotto D, Briand JP, Prato M and Bianco A. Translocation of bioactive peptides across cell membranes by carbon nanotubes. Chemical Communications 2004;16.

[16] Lu Q, Moore JM, Huang G, Mount AS, Rao AM, Larcom LL and Ke PC. Rna polymer translocation with single-walled carbon nanotubes. Nano Letters 2004;4:2473.

[17] Private communications with Prof. Robert Hurt of the school of engineering and Prof. Agnes Kane of the school of medicine of Brown University.

[18] Aoyama Y, Kanamori T, Nakai T, Sasaki T, Horiuchi S, Sando S and Niidome T. Artificial viruses and their application to gene delivery. Size-controlled gene coating with glycocluster nanoparticles. Journal of the American Chemical Society 2003;125:3455.

[19] Desai MP, Labhasetwar V, Walter E, Levy RJ and Amidon GL. The mechanism of uptake of biodegradable microparticles in caco-2 cells is size dependent. Pharmaceutical Research 1997;14:1568.

[20] Chithrani BD, Ghazani AA and Chan WCW. Determining the size and shape dependence of gold nanoparticle uptake into mammalian cells. Nano Letters 2006;6:662.

[21] Geng Y, Dalhaimer P, Cai SS, Tsai R, Tewari M, Minko T and Discher DE. Shape effects of filaments versus spherical particles in flow and drug delivery. Nature Nanotechnology 2007;2:249.

[22] Gao HJ, Shi WD and Freund LB. Mechanics of receptor-mediated endocytosis. Proceedings of the National Academy of Sciences of the United States of America 2005;102:9469.

[23] Kol N, Shi Y, Tsvitov M, Barlam D, Shneck RZ, Kay MS and Rousso I. A stiffness switch in human immunodeficiency virus. Biophysical Journal 2007;92:1777.

[24] Viculis LM, Mack JJ and Kaner RB. A chemical route to carbon nanoscrolls. Science 2003;299:1361.

[25] Xie X, Ju L, Feng XF, Sun YH, Zhou RF, Liu K, Fan SS, Li QL and Jiang KL. Controlled fabrication of high-quality carbon nanoscrolls from monolayer graphene. Nano Letters 2009;9:2565.

[26] Savoskin MV, Mochalin VN, Yaroshenko AP, Lazareva NI, Konstantinova TE, Barsukov IV and Prokofiev LG. Carbon nanoscrolls produced from acceptor-type graphite intercalation compounds. Carbon 2007;45:2797.

[27] Roy D, Angeles-Tactay E, Brown RJC, Spencer SJ, Fry T, Dunton TA, Young T and Milton MJT. Synthesis and raman spectroscopic characterisation of carbon nanoscrolls. Chemical Physics Letters 2008;465:254.

[28] Chuvilin AL, Kuznetsov VL and Obraztsov AN. Chiral carbon nanoscrolls with a polygonal cross-section. Carbon 2009;47:3099.

[29] Shioyama H and Akita T. A new route to carbon nanotubes. Carbon 2003;41:179.

[30] Chen Y, Lu J and Gao ZX. Structural and electronic study of nanoscrolls rolled up by a single graphene sheet. Journal of Physical Chemistry C 2007;111:1625.

[31] Braga SF, Coluci VR, Legoas SB, Giro R, Galvao DS and Baughman RH. Structure and dynamics of carbon nanoscrolls. Nano Letters 2004;4:881.

[32] Braga SF, Coluci VR, Baughman RH and Galvao DS. Hydrogen storage in carbon nanoscrolls: An atomistic molecular dynamics study. Chemical Physics Letters 2007;441:78.

[33] Coluci VR, Braga SF, Baughman RH and Galvao DS. Prediction of the hydrogen storage capacity of carbon nanoscrolls. Physical Review B 2007;75.

[34] Mpourmpakis G, Tylianakis E and Froudakis GE. Carbon nanoscrolls: A promising material for hydrogen storage. Nano Letters 2007;7:1893.

[35] Pan H, Feng Y and Lin J. Ab initio study of electronic and optical properties of multiwall carbon nanotube structures made up of a single rolled-up graphite sheet. Physical Review B 2005;72.

[36] Rurali R, Coluci VR and Galvao DS. Prediction of giant electroactuation for papyruslike carbon nanoscroll structures: First-principles calculations. Physical Review B 2006;74.

[37] Avouris P. Molecular electronics with carbon nanotubes. Accounts of Chemical Research 2002;35:1026.

[38] Lacerda L, Bianco A, Prato M and Kostarelos K. Carbon nanotubes as nanomedicines: From toxicology to pharmacology. Advanced Drug Delivery Reviews 2006;58:1460.

[39] Gartstein YN, Zakhidov AA and Baughman RH. Charge-induced anisotropic distortions of semiconducting and metallic carbon nanotubes. Physical Review Letters 2002;89.

[40] Lefevre R, Goffman MF, Derycke V, Miko C, Forro L, Bourgoin JP and Hesto P. Scaling law in carbon nanotube electromechanical devices. Physical Review Letters 2005;95.

[41] Hummer G, Rasaiah JC and Noworyta JP. Water conduction through the hydrophobic channel of a carbon nanotube. Nature 2001;414:188.

[42] Zhu FQ and Schulten K. Water and proton conduction through carbon nanotubes as models for biological channels. Biophysical Journal 2003;85:236.

[43] Wan RZ, Li JY, Lu HJ and Fang HP. Controllable water channel gating of nanometer dimensions. Journal of the American Chemical Society 2005;127:7166.

[44] Joseph S and Aluru NR. Pumping of confined water in carbon nanotubes by rotation-translation coupling. Physical Review Letters 2008;101.

[45] Garate JA, English NJ and MacElroy JMD. Carbon nanotube assisted water self-diffusion across lipid membranes in the absence and presence of electric fields. Molecular Simulation 2009;35:3.

[46] Liu B, Li XY, Li BL, Xu BQ and Zhao YL. Carbon nanotube based artificial water channel protein: Membrane perturbation and water transportation. Nano Letters 2009;9:1386.

[47] Mashl RJ, Joseph S, Aluru NR and Jakobsson E. Anomalously immobilized water: A new water phase induced by confinement in nanotubes. Nano Letters 2003;3:589.

[48] Gong XJ, Li JY, Lu HJ, Wan RZ, Li JC, Hu J and Fang HP. A charge-driven molecular water pump. Nature Nanotechnology 2007;2:709.

[49] Li JY, Gong XJ, Lu HJ, Li D, Fang HP and Zhou RH. Electrostatic gating of a nanometer water channel. Proceedings of the National Academy of Sciences of the United States of America 2007;104:3687.

[50] Zou J, Ji BH, Feng XQ and Gao HJ. Self-assembly of single-walled carbon nanotubes into multiwalled carbon nanotubes in water: Molecular dynamics simulations. Nano Letters 2006;6:430.

[51] Gao HJ and Kong Y. Simulation of DNA-nanotube interactions. Annual Review of Materials Research 2004;34:123.

[52] Gao HJ, Kong Y, Cui DX and Ozkan CS. Spontaneous insertion of DNA oligonucleotides into carbon nanotubes. Nano Letters 2003;3:471.

[53] Liu GR, Cheng Y, Mi D and Li ZR. A study on self-insertion of peptides into single-walled carbon nanotubes based on molecular dynamics simulation. International Journal of Modern Physics C 2005;16:1239.

[54] Shi XH, Kong Y and Gao HJ. Coarse grained molecular dynamics and theoretical studies of carbon nanotubes entering cell membrane. Acta Mechanica Sinica 2008;24:161.

[55] Smit B, Esselink K, Hilbers PAJ, Vanos NM, Rupert LAM and Szleifer I. Computer-simulations of surfactant self-assembly. Langmuir 1993;9:9.

[56] Palmer BJ and Liu J. Simulations of micelle self-assembly in surfactant solutions. Langmuir 1996;12:746.

[57] Goetz R and Lipowsky R. Computer simulations of bilayer membranes: Self-assembly and interfacial tension. Journal of Chemical Physics 1998;108:7397.

[58] den Otter WK and Briels WJ. The bending rigidity of an amphiphilic bilayer from equilibrium and nonequilibrium molecular dynamics. Journal of Chemical Physics 2003;118:4712.

[59] vonGottberg FK, Smith KA and Hatton TA. Stochastic dynamics simulation of surfactant self-assembly. Journal of Chemical Physics 1997;106:9850.

[60] Noguchi H and Takasu M. Self-assembly of amphiphiles into vesicles: A brownian dynamics simulation. Physical Review E 2001;64.

[61] Marrink SJ, de Vries AH and Mark AE. Coarse grained model for semiquantitative lipid simulations. Journal of Physical Chemistry B 2004;108:750.

[62] Berendsen HJC, Postma JPM, Vangunsteren WF, Dinola A and Haak JR. Molecular-dynamics with coupling to an external bath. Journal of Chemical Physics 1984;81:3684.

[63] Berendsen HJC, Vanderspoel D and Vandrunen R. Gromacs - a message-passing parallel molecular-dynamics implementation. Computer Physics Communications 1995;91:43.

[64] Jahn R, Lang T and Sudhof TC. Membrane fusion. Cell 2003;112:519.

[65] White JM. Viral and cellular membrane-fusion proteins. Annual Review of Physiology 1990;52:675.

[66] Lopez CF, Nielsen SO, Moore PB and Klein ML. Understanding nature's design for a nanosyringe. Proceedings of the National Academy of Sciences of the United States of America 2004;101:4431.

[67] Evans EA, Skalak R and Hochmuth RM. Mechanics and thermodynamics of biomembranes .1. Crc Critical Reviews in Bioengineering 1979;3:181.

[68] Rawicz W, Olbrich KC, McIntosh T, Needham D and Evans E. Effect of chain length and unsaturation on elasticity of lipid bilayers. Biophysical Journal 2000;79:328.

[69] Turley WD and Offen HW. Lipid microviscosity of dmpc vesicles at high-pressures - dipyrenylpropane excimer fluorescence. Journal of Physical Chemistry 1986;90:1967.

[70] Yang FQ and Li JCM. Impression creep of a thin-film by vacancy diffusion .2. Cylindrical punch. Journal of Applied Physics 1993;74:4390.

[71] Kane AB and Hurt RH. Nanotoxicology: The asbestos analogy revisited. Nature Nanotechnology 2008;3:378.

[72] Poland CA, Duffin R, Kinloch I, Maynard A, Wallace WAH, Seaton A, Stone V, Brown S, MacNee W and Donaldson K. Carbon nanotubes introduced into the abdominal cavity of mice show asbestos-like pathogenicity in a pilot study. Nature Nanotechnology 2008;3:423.

[73] Ghio AJ, Stonehuerner J, Richards J and Devlin RB. Iron homeostasis in the lung following asbestos exposure. Antioxidants & Redox Signaling 2008;10:371.

[74] Cooke IR, Kremer K and Deserno M. Tunable generic model for fluid bilayer membranes. Physical Review E 2005;72.

[75] Reynwar BJ, Illya G, Harmandaris VA, Muller MM, Kremer K and Deserno M. Aggregation and vesiculation of membrane proteins by curvature-mediated interactions. Nature 2007;447:461.

[76] Yi X, Shi X and Gao H. In progress. 2010.

[77] Nelson P. *Biological physics: Energy, information, life* (Freeman, New York) 2003.

[78] Shi WD, Wang JZ, Fan XJ and Gao HJ. Size and shape effects on diffusion and absorption of colloidal particles near a partially absorbing sphere: Implications for uptake of nanoparticles in animal cells. Physical Review E 2008;78.

[79] Muller MM, Deserno M and Guven J. Balancing torques in membrane-mediated interactions: Exact results and numerical illustrations. Physical Review E 2007;76.

[80] Tirado MM, Martinez CL and Delatorre JG. Comparison of theories for the translational and rotational diffusion-coefficients of rod-like macromolecules - application to short DNA fragments. Journal of Chemical Physics 1984;81:2047.

[81] Beningo KA and Wang YL. Fc-receptor-mediated phagocytosis is regulated by mechanical properties of the target. Journal of Cell Science 2002;115:849.

[82] Plimpton S. Fast parallel algorithms for short-range molecular-dynamics. Journal of Computational Physics 1995;117:1.

[83] Stuart SJ, Tutein AB and Harrison JA. A reactive potential for hydrocarbons with intermolecular interactions. Journal of Chemical Physics 2000;112:6472.

[84] Brenner DW, Shenderova OA, Harrison JA, Stuart SJ, Ni B and Sinnott SB. A second-generation reactive empirical bond order (rebo) potential energy expression for hydrocarbons. Journal of Physics-Condensed Matter 2002;14:783.

[85] Helfrich W. Elastic properties of lipid bilayers - theory and possible experiments. Zeitschrift Fur Naturforschung C-a Journal of Biosciences 1973;C 28:693.

[86] Deserno M. Elastic deformation of a fluid membrane upon colloid binding. Physical Review E 2004;69.

[87] Seifert U and Lipowsky R. Adhesion of vesicles. Physical Review A 1990;42:4768.

[88] Yi X, Shi X and Gao H. On cellular uptake of elastic nanoparticles. submitted 2010.

[89] Shi XH, Pugno NM and Gao HJ. Tunable core size of carbon nanoscrolls. Journal of Computational and Theoretical Nanoscience 2010;7:517.

[90] Shi X, Pugno N and Gao H. Constitutive behavior of pressurized carbon nanoscrolls. International Journal of Fracture 2010;submitted.

[91] Hess B, Kutzner C, van der Spoel D and Lindahl E. Gromacs 4: Algorithms for highly efficient, load-balanced, and scalable molecular simulation. Journal of Chemical Theory and Computation 2008;4:435.

[92] Walther JH, Jaffe R, Halicioglu T and Koumoutsakos P. Carbon nanotubes in water: Structural characteristics and energetics. Journal of Physical Chemistry B 2001;105:9980.

[93] Jorgensen WL, Chandrasekhar J, Madura JD, Impey RW and Klein ML. Comparison of simple potential functions for simulating liquid water. Journal of Chemical Physics 1983;79:926.

[94] Darden T, York D and Pedersen L. Particle mesh ewald - an n.Log(n) method for ewald sums in large systems. Journal of Chemical Physics 1993;98:10089.

[95] Essmann U, Perera L, Berkowitz ML, Darden T, Lee H and Pedersen LG. A smooth particle mesh ewald method. Journal of Chemical Physics 1995;103:8577.

[96] Shi XH, Cheng Y, Pugno NM and Gao HJ. Tunable water channels with carbon nanoscrolls. Small 2010;6:739.

[97] Israelachvili J. *Intermolecular & surface forces* (Academic Press, London) 1991.

[98] Langlet R, Devel M and Lambin P. Computation of the static polarizabilities of multi-wall carbon nanotubes and fullerites using a gaussian regularized point dipole interaction model. Carbon 2006;44:2883.

[99] Maheshwari R, Parthasarathi R and Dhathathreyan A. Molecular dipoles at substrate/film interfaces influencing surface energy of langmuir-blodgett films. Journal of Colloid and Interface Science 2004;271:419.

[100] Shi XH, Pugno NM, Cheng Y and Gao HJ. Gigahertz breathing oscillators based on carbon nanoscrolls. Applied Physics Letters 2009;95.

[101] Guo WL, Guo YF, Gao HJ, Zheng QS and Zhong WY. Energy dissipation in gigahertz oscillators from multiwalled carbon nanotubes. Physical Review Letters 2003;91.

[102] Rivera JL, McCabe C and Cummings PT. The oscillatory damped behaviour of incommensurate double-walled carbon nanotubes. Nanotechnology 2005;16:186.

[103] Liu P, Gao HJ and Zhang YW. Effect of defects on oscillation characteristics and instability of carbon nanotube-based oscillators. Applied Physics Letters 2008;93.

[104] Xu ZP. Energy dissipation in the double-walled carbon nanotube based mechanical oscillators. Journal of Computational and Theoretical Nanoscience 2008;5:655.

[105] Kim SY and Park HS. Multilayer friction and attachment effects on energy dissipation in graphene nanoresonators. Applied Physics Letters 2009;94.

[106] Lin WH and Zhao YP. Nonlinear behavior for nanoscale electrostatic actuators with casimir force. Chaos Solitons & Fractals 2005;23:1777.

[107] Zhao MH, Wang ZL and Mao SX. Piezoelectric characterization of individual zinc oxide nanobelt probed by piezoresponse force microscope. Nano Letters 2004;4:587.

[108] Shi XH, Cheng Y, Pugno NM and Gao HJ. A translational nanoactuator based on carbon nanoscrolls on substrates. Applied Physics Letters 2010;96.

[109] Verkman AS, VanHoek AN, Ma TH, Frigeri A, Skach WR, Mitra A, Tamarappoo BK and Farinas J. Water transport across mammalian cell membranes. American Journal of Physiology-Cell Physiology 1996;270:C12.

[110] Knepper MA. Molecular physiology of urinary concentrating mechanism: Regulation of aquaporin water channels by vasopressin. American Journal of Physiology-Renal Physiology 1997;272:F3.

[111] Steudle E and Henzler T. Water channels in plants - do basic concepts of water transport change. Journal of Experimental Botany 1995;46:1067.

[112] Tieleman DP and Berendsen HJC. Molecular dynamics simulations of a fully hydrated dipalmitoyl phosphatidylcholine bilayer with different macroscopic boundary conditions and parameters. Journal of Chemical Physics 1996;105:4871.

[113] Bussi G, Donadio D and Parrinello M. Canonical sampling through velocity rescaling. Journal of Chemical Physics 2007;126.

[114] Parrinello M and Rahman A. Polymorphic transitions in single-crystals - a new molecular-dynamics method. Journal of Applied Physics 1981;52:7182.

[115] Zou J, Ji BH, Feng XQ and Gao HJ. Molecular-dynamic studies of carbon-water-carbon composite nanotubes. Small 2006;2:1348.

[116] Liu YC, Shen JW, Gubbins KE, Moore JD, Wu T and Wang Q. Diffusion dynamics of water controlled by topology of potential energy surface inside carbon nanotubes. Physical Review B 2008;77.

[117] Tieleman DP, Leontiadou H, Mark AE and Marrink SJ. Simulation of pore formation in lipid bilayers by mechanical stress and electric fields. Journal of the American Chemical Society 2003;125:6382.

[118] Lu Q, Arroyo M and Huang R. Elastic bending modulus of monolayer graphene. Journal of Physics D-Applied Physics 2009;42.